KINEMATICS AND COLLISION KINETICS IN HIGH SHEAR GRANULATION

Amol M. Nilpawar

In partial fulfillment of the requirements of the degree of
Doctor of Philosophy in Engineering

Department of Chemical and Process Engineering

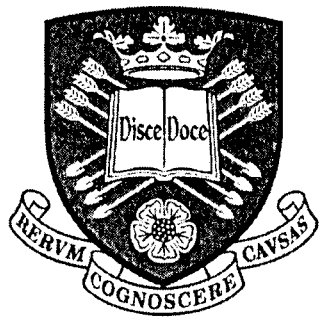

The University of Sheffield

October 2006

ABSTRACT

High shear granulation (HSG) is an important unit operation in the Pharmaceutical, Detergent and Food industries. The desired output of HSG is generally a specified granule size distribution (GSD) and bulk density of the granular product. Depending on the final application, homogeneity, strength and internal structure of granules also need to be of desired quality. In industry this operation suffers from problems such as poor reproducibility and high rejection rate. Knowledge in this area is mainly empirical for both operation and scaling up. A generalised universal approach needs to be developed. This is possible if the rate processes in granulation are understood.

In this dissertation a new approach to granulation is suggested as follows. The operating conditions and properties of the agglomerating substances dictate the bulk flow and thus the particle relative motion responsible for particle-particle collisions. The particle-particle collisions result in aggregation, breakage or rebound of particles. So only a fraction of colliding particles will result in aggregating successfully. If the relationship between these individual processes is understood, given the initial conditions, it would be possible to predict the output.

A novel cost-effective technique to measure surface velocities in HSG has been developed by combining High Speed Imaging and Particle Image Velocimetry. This technique resulted in efficient characterization of the mean and the particulate flow in a vertical axis high shear mixer with high temporally and spatially resolved velocity data. The equipment used for HSG is referred to as high shear mixer (HSM) in the chemical industry. The experimental mixer (Roto Junior, Zanchetta, Italy) was a 10 litre, vertical axis HSM with a provision to change the mixing blade. The test feed material was Calcium carbonate (Durcal 40) and binders used were Polyethylene Glycols (PEG, avg. molar masses 400, 1500 and 4000 g/mol) and Glycerol. Effect of operating conditions and material properties on the flow has been established in the high shear mixer equipped with a 3-blade impeller. The average bed velocities were found to increase with increase in impeller speed, although approaching a stable value at higher impeller speeds. A higher viscosity binder considerably slowed the bed. Also it was noticed during a wet granulation (granulation wherein a liquid binder is used) experiment that

the bed velocities were a function of availability of surface binder and the average granule size. The results were found to be highly reproducible for dry granules.

A disc impeller was used for further experiments with dry granules mainly to simplify the mean flow in order to extract velocity fluctuations to calculate collision frequencies. The Kinetic Theory of Granular Flow (KTGF) was found to predict particle collision frequencies three orders of magnitude higher than those predicted by the Shear theory. This observation with disc impeller experiments provided a basis to perform further experiments with the 3-blade impeller.

In a wet granulation experiment with the 3-blade impeller, simultaneous observation of particle dynamics and GSD was made. By extracting temporal velocities from a single interrogation area, granular temperature and subsequently collision frequencies based on the KTGF were calculated. A discretised population balance equation was fitted to the GSD data by minimising overall sum of square errors to calculate the aggregation rate constant. From the knowledge of the collision rate and the aggregation rate, aggregation efficiency was estimated to be of the order of 4 in 100 million in the initial stages of granulation with gradual decrease in this value as granulation proceeded. This method of extracting particle collision rate, aggregation rate and estimated aggregation efficiency provides a basis for predictive high shear granulation model using population balance modelling and knowledge of particle dynamics.

ACKNOWLEDGEMENTS

My sincere gratitude to my supervisors, Prof. M. J. Hounslow and Dr. A. D. Salman, for putting their faith in me and providing the opportunity to carry out research studies and be part of the prestigious Particle Products Group (PPG). I am very grateful to the University of Sheffield and the PPG at the Department of Chemical and Process Engineering for providing the fee bursary and the scholarship. My progress through PhD research was particularly smooth due to the support and guidance from Dr. Gavin K. Reynolds. I thank him with utmost humility for being such a great colleague and mentor. Also I would like to thank Mr. Chris Wright and Mr. Adrian Lumby for their technical support regarding high shear mixer and in fabricating a disc impeller. The EPSRC - Engineering Instrument pool (EPSRC-EIP, 2006) has been very generous to lend the high speed camera systems on more than one occasion. Special thanks to them as this research would have not taken its current shape without it.

Life in Sheffield was very pleasant and interesting due to great friend circle that helped me to evolve into a better person. They will always be my inspiration towards every endeavour in life and I look forward to their unending friendship beyond Sheffield. Also I thank all colleagues from PPG and the Department for being great companions from whom I learned a lot.

I am also very grateful to my brother Sanjay who encouraged me towards taking up PhD research studies. I would like to thank my parents, brother and sister for being always there to help and support me. Last but not least I would like to thank each and every person who came across my life and influenced it in a positive way.

CONTENTS

1

INTRODUCTION

1.1 NEW APPROACH TO GRANULATION

Granulation is a unit operation commonly used in the chemical industry. There are many physical parameters that dictate the granulation process. Research in this subject area in the past couple of decades has been focused on understanding the specific equipments and their working methodology. It is only in the past decade or so that the basic research to understand granulation and to provide a common working understanding of this unit operation has gathered momentum. The need is to understand the physical processes and transformations at the microscopic level. This understanding can then be scaled up to the process scale level.

Researchers have identified the need to develop a predictive model for granulation. A predictive model would enable to make a priori prediction of the output of granulation. This kind of prediction is possible if the underlying rate processes in granulation are understood well. As granulation is a very complex unit operation, understanding the rate processes is rather difficult considering the interdependencies of the various rate processes that influence it. Attempts to understand these processes towards building a predictive model, in particular for high shear granulation (HSG), can be found in the work of Knight et al. (1998), Iveson et al. (2001a), Pearson et al. (2001), Hounslow et al. (1998, 2001), Ramaker et al.(1998, 2001), Biggs et al. (2003), Sanders et al. (2003), Hapgood (2000) and Scott et al. (2000a, 2000b). Many researchers have used similar approach in fluidised bed granulation and drum granulation as well. Although, the models developed to describe HSG are still not well developed due to the complexities

of the various inter-dependent parameters that influence it. This is the main motivation behind this research to develop a universal approach to HSG.

A new approach to granulation has been suggested as shown in Figure 1.1. The operating conditions and properties of the agglomerating substances dictate the bulk flow and thus the particle relative motion. This particle relative motion causes particle-particle collisions. Particles in this context can be depicted as the primary powder particles or the granules containing primary particles as well as binder. The particle-particle collisions result in aggregation, breakage or rebound of particles. So only a fraction of collisions will successfully result in aggregation. The end product of a granulation process is a stipulated granule size distribution (GSD) and bulk density. If the relationship between these individual processes is understood, given the initial conditions, it would be possible to predict the output such as GSD. This forms the basis of this research thesis.

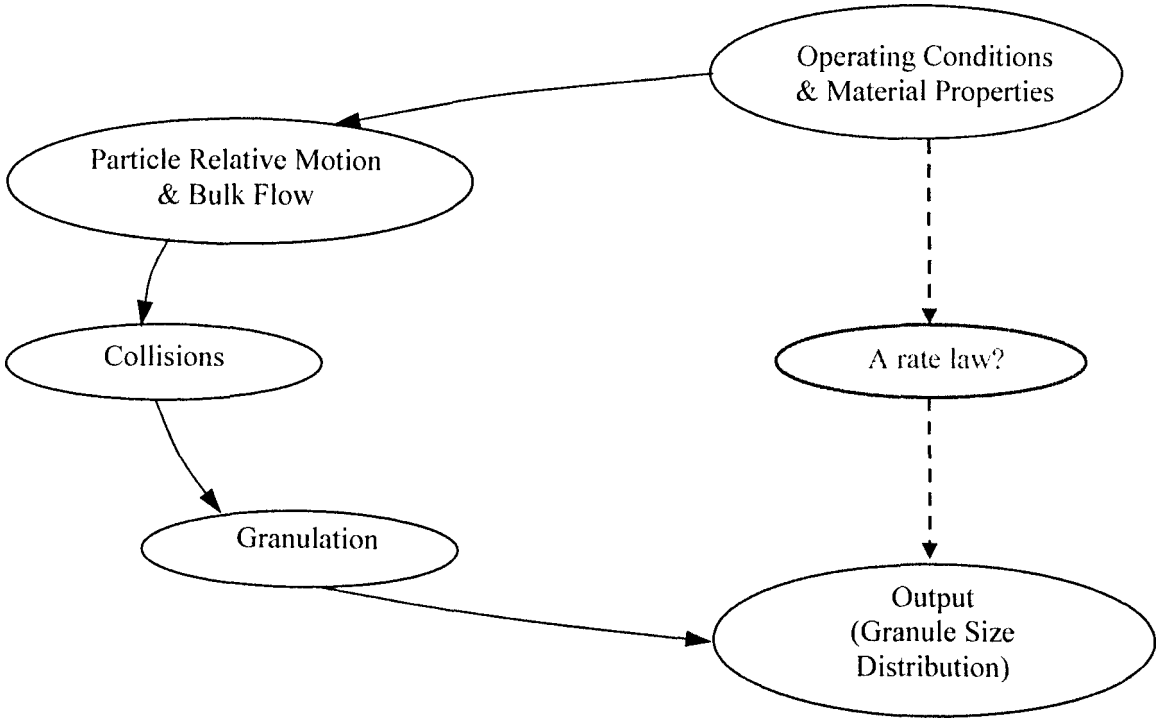

Figure 1.1: A new approach to granulation.

A novel cost-effective technique to measure surface velocities in HSG has been developed by combining High Speed Imaging and Particle Image Velocimetry to investigate the surface flow in a vertical axis high shear mixer. The development of this technique is described in Chapter 3. The results in this thesis are limited to surface flow

observation and corresponding inferences are made based on these observation only and not on the observations inside the bulk material in the high shear mixer. The effect of operating conditions and material properties on the flow has been investigated in the high shear mixer equipped with a 3-blade impeller, the results of which are discussed in Chapter 4. In Chapter 5, experiments with a disc impeller for dry granules are analysed. These experiments were mainly performed to simplify the mean flow in order to extract velocity fluctuations to calculate collision frequencies. This observation with disc impeller experiments provided a basis to perform further experiments with the 3-blade impeller. Based on the methodology developed in Chapter 5, further experiment with a 3-blade impeller with simultaneous observation of particle dynamics and granule size distribution (GSD) are analysed in Chapter 6 that lead to extracting temporal velocities from a single interrogation area, granular temperature and subsequently collision frequencies based on the Kinetic Theory of Granular Flow were calculated. A discretised population balance equation was fitted to the GSD data by minimising overall sum of square errors to calculate the aggregation rate constant. From the knowledge of the collision rate and the aggregation rate, aggregation efficiency was estimated to be of the order of 4 in 100 million in the initial stages of granulation with gradual decrease in this value as granulation proceeded. This is a first ever estimation of aggregation efficiency in the granulation literature and the collision frequency estimation is a first ever for high shear granulation. These observations are open for further rigorous and critical investigation to the granulation research community. The conclusions from this research are discussed in Chapter 7.

In Chapter 1, section 1.2 develops a thorough understanding of the granulation process. The types of granulation equipments are listed in section 1.3 and the chapter then converges to the specific research topic that is high shear granulation in section 1.4 and factors affecting high shear granulation are discussed in section 1.5. Chapter 2 introduces the reader to the techniques used for investigating granular flow inside high shear mixers and findings from previous researchers. The theoretical background utilised in this research is also discussed in Chapter 2.

1.2 GRANULATION

Granulation is one of the many types of size enlargement processes. Other examples of size enlargement processes are compaction, extrusion, sintering, spray drying, and prilling. Granulation can be defined as the process of agglomerating particles together into aggregates, commonly known as granules (Ennis et al., 1997) with the aid of mechanical agitation methods (Rhodes, 1999). The granules are semi-permanent and conserve the original shape and/or properties of its components. In granulation, a particulate feed and a liquid binder is agitated in a process vessel to form a granulated product. It is also commonly referred to as 'Wet granulation' in the literature due to the addition of binder that is in liquid form either throughout the process or only during the agglomeration of particles. Granulation has gained wide acceptance in industry as it has the capability to produce multi-component granules specifically targeted to the consumer needs (Edwards et al., 2001). The unit operation employs processing equipment such as drums, pans, fluid beds and high shear mixers. It is widely used in industries such as pharmaceutical, consumer products, mineral processing, fertilizer, food, ceramics and fine chemicals. It is mainly employed to:

- Reduce dustiness to avoid health hazards
- Increase bulk density for easy storage and transportation
- Improve flowability
- Reduce caking and lump formation
- Aid in uniform distribution of individual components in the finished product

1.2.1 Mechanisms of granulation

All mechanisms of granulation described traditionally are nowadays considered as cases of coalescence and/or breakage as illustrated in Figure 1.2 (Iveson et al., 2001b). The variables are the size of coalescing granules/particles and the availability of surface liquid. This modern approach to granulation, a combination of three sets of rate processes, has been widely accepted in the granulation research community (Ennis et al., 1997; Iveson et al., 2001b). Iveson et al. (2001b) discuss these processes in detail in their review paper. These are wetting and nucleation, consolidation and growth, and attrition and breakage. These three processes can be thought of as the rate processes at granule level and in turn control the size distribution and density of the product granules.

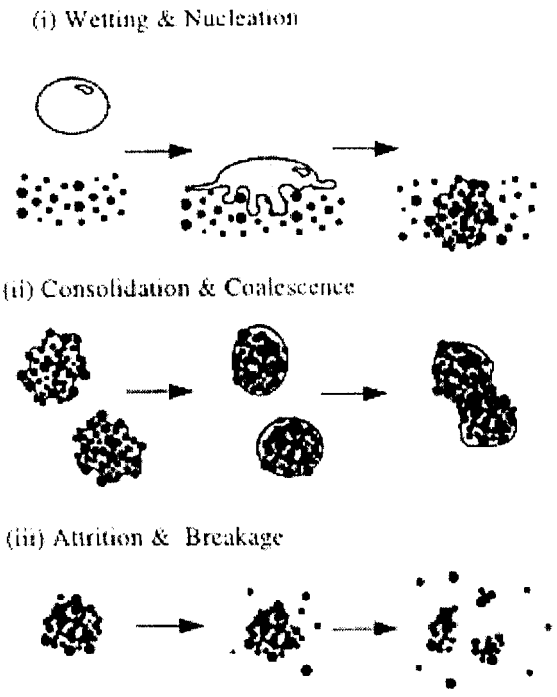

Figure 1.2: Modern approach to granulation processes, Ennis et al. (1997).

1.2.1.1 Wetting and nucleation

In wetting and nucleation, the initial contact between liquid binder with a dry powder bed gives a distribution of nuclei granules. In the nucleation regime all the granule collisions are successful provided free binder is available and so it is mainly controlled by binder feed rate and distribution (Ennis, 1991). This was confirmed by Hoornaert et al. (1998) in their experiments in a 50l horizontal axis Lodige mixer granulator. The binder can be added to the powder in three different ways, namely spraying, melt-in, and pour-on (discussed in section 1.2.3), which leads to different behaviour in this initial stage of wetting and nucleation. Litster et al. (2001) noticed that binder spraying can lead to nuclei formation on a moving powder in experiment outside a granulator. Whereas, Hapgood (2000) found that nucleation is controlled by mechanical dispersion of binder for pour-on type of addition. As the binder is not dispersed instantaneously, it leads to formation of in-homogeneous distribution resulting in local over-wetting and dry region formation as noticed by Knight et al. (1998). They also noticed that this in-homogeneous distribution of binder results in bimodal distribution of the resulting granules. Scott et al. (2000b) also found bimodal distribution in the initial stages of granulation for both pour-on as well as melt-in type of binder addition.

1.2.1.2 Consolidation and growth

In this stage after initial nucleation, the collisions between two granules, granules and feed powder, or a granule and the equipment lead to granule compaction and growth. Kristensen (1985) noticed that at the initial stages nucleation proceeds by liquid bridge bonding whereas the agglomerates have to achieve certain strength for coalescence. Ennis (1991) also noticed that the consolidation is mainly influenced by operating parameters such as impeller speed and material properties such as binder viscosity. He also proposed that the consolidation and in turn breakage are influenced by collisional kinetic energy and binder viscosity.

1.2.1.3 Attrition and breakage

Granules break due to impact, wear or compaction in the granulator. Granule breakage is an important phenomenon in granulation as it improves granule homogeneity. In granulation literature, granule 'strength' is used as a property of granule to quantify how easy or difficult it is to break a granule. At a granule level, mainly two theories have been widely accepted in the literature (Reynolds et al., 2005), Rumpf's (1962) classical model for predicting the static tensile strength (σ_v) and Kendall's (1988) expression of fracture strength (σ_f) of granules. According to Rumpf (1962) fracture of a granule is mainly caused by the tensile stress generated within the assembly and all the interparticle bonds across fracture simultaneously. Whereas Kendall (1988) postulated that the granule breaks due to crack nucleation at flaws with subsequent propagation. Such an understanding at a single granules level and the effect of process parameters on an ensemble of granules has been widely studies in the literature. As pointed out by Reynolds et al. (2005), the granule breakage inside a granulator (macro-scale level) depends on various parameters such as agitation intensity (impeller speed), various binder properties (viscosity, surface tension, contact angle with primary particle, content), binder addition method, primary particle size and shape, and granulation time.

1.2.2 Granule growth regime map

According to Iveson et al. (2001b, 2001c), granule growth behaviour is a function of the maximum pore liquid saturation and the amount of granule deformation during impact (Figure 1.3). The pore liquid saturation is the percentage volume inside a granule occupied by binder excluding the volume occupied by the solid powder particles.

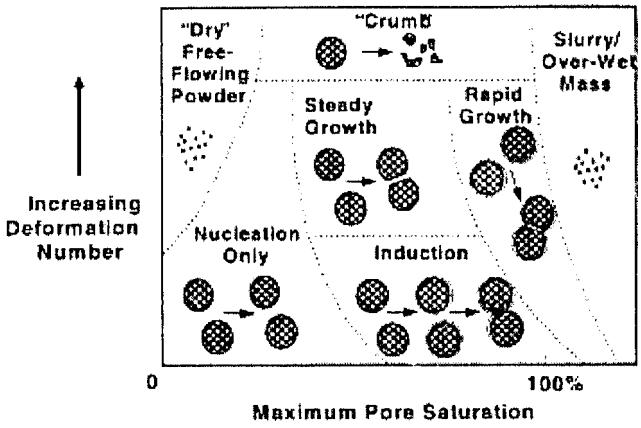

Figure 1.3: Granule growth regime map (Iveson et al., 1998a).

The amount of deformation is characterised by a Stokes deformation number (St_{def}), which is the ratio of the kinetic energy of the impact and the dynamic granule strength. The equation for Stokes deformation number can be written as:

$$St_{def} = \frac{\rho \upsilon_c^2}{2\sigma_y} \tag{1.1}$$

where, υ_c is the representative collision velocity; ρ is the granular density; σ_y is the tensile strength of granule. Iveson et al. (1998a) explained the type of granule growth behaviour as a function of maximum pore saturation and Stoke's deformation number. The different regimes show that:

- Weak and deformable granules undergo *steady growth* either by the crushing and layering mechanism or else they deform producing large contact area to get coalesced. Weaker granules have higher Stokes deformation number and are susceptible to deformation compared to stronger granules with lower Stokes deformation number.
- *Induction growth* occurs in relatively stronger systems. When granules are stronger they can not coalesce unless surface liquid is available. Granules under compaction forces squeeze out liquid onto the surface. The granules then tend to grow until the torque exerted on dumbbell pairs becomes too large.
- *Nucleation only growth* occurs when granule nuclei form, but the binder is insufficient to promote further growth.
- When the formulation is too weak to form permanent granules it forms a loose *crumb* material.
- When excess binder is added to the system it tends to form *slurry / over-wet mass.*

However while validating the growth regime map in further research Iveson et al. (2001c) found that regime map convincingly represents the drum granulation but not the high shear granulation data. They suggested it could be due to the over-estimated values of collision velocities (in Eq. 1.1) that were approximated to the chopper tip speed. So they emphasised the need of investigation of particle dynamics in high shear mixers. In further research, Iveson et al. (2003) emphasised the importance of flow pattern measurement in granulators to better estimate strain-rate that would in turn be adapted to improve coalescence/aggregation models. These observations support the importance of investigating kinematics in high shear granulation, which is one of the aims of this research.

1.2.3 Methods of binder addition

The method of binder addition changes according to the process and product requirements. There are mainly three different types of binder addition commonly used in granulation namely spraying, melt-in, and pour-on. Mixer granulators can handle all these types of binder addition. Such versatility is rare in tumbling and fluidized bed granulation. The energy input through the impeller and chopper in mixer granulator helps in distribution of binder for melt-in and pour-on types of binder addition.

Spraying

In spraying type of binder addition the binder in liquid form is atomized through a spray nozzle and directed on the powder bed. This aids uniform distribution of binder right from the beginning of the granulation process. The downside of spraying is that it requires a closed system for avoiding the powder and the binder from escaping the process vessel or the spray atomization has to be at low pressure. So an exit for the atomizing air is required as well. This method is common for all types of granulation equipment.

Melt-in

When binder in solid flake or chunk form is directly mixed with dry powder and allowed to melt while mixing, it is called a melt-in type of binder addition. These types of binders are solid at room temperature and require in-process heating to provide higher temperature for melting. So mixing, melting and binder disbursal all happen

simultaneously. This is generally used in mixer granulators as the binder disbursal requires high energy input through shear and impact forces.

Pour-on

Pour-on type of binder addition means direct addition of liquid binder onto the powder bed. If the binder has higher melting temperature than the room temperature, then the binder is first melted and then added while keeping the granulator operating temperature near to the melting point of the binder.

1.3 TYPES OF GRANULATION EQUIPMENT

Granulation equipment can be classified according to the type of motion and force imparted to the feed material. The type of motion and forces in action decide the properties of the end material.

1.3.1 Tumbling granulators

Drums, pans and disc granulators are different kinds of tumbling granulators. This is commonly used in the fertilizer industry. The shear forces applied on the granules are relatively low in this type of granulator. The end product normally has low to medium density but the granules are very spherical. These are usually continuous granulators and can handle high throughputs.

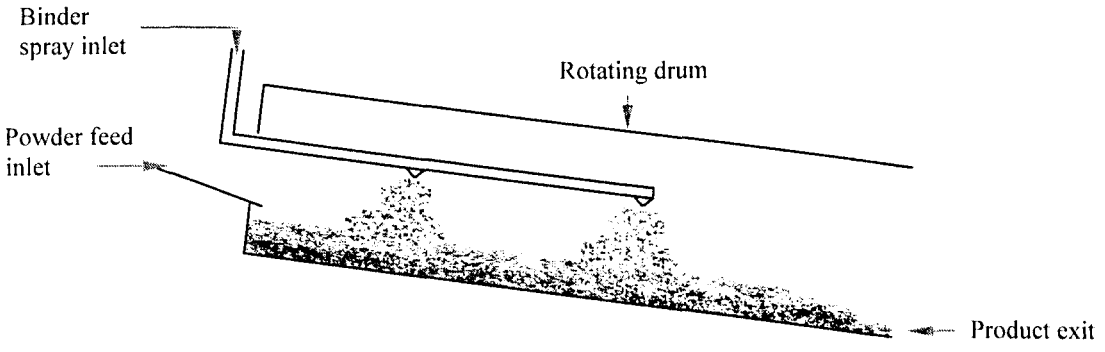

Figure 1.4: Schematic of drum granulation.

In drum granulators (Figure 1.4), the feed is introduced from one end and the product comes out from the other end as a consequence of the inclination and the rotational

motion of the drum. The binder is normally sprayed on the feed inside the drum. Pan granulators are rotating disc with rim, inclined at angles of 45° to 55°. Powder is continuously fed at the edge of the rotating granular bed. Binder is sprayed across the radial face of the disc. Pan or dish granulators are employed in industries such as agricultural chemicals and mineral processing.

1.3.2 Fluidised bed granulators

In fluidised bed granulators, the powder feed is supported by a mesh and fluidised by air from underneath as shown in Figure 1.5. Atomized liquid binder is sprayed directly on the fluidised powder feed. The binder solidifies quickly creating solid bridges between particles. Low shear and impact forces inside a fluidised bed mean that the binder redistribution will not occur after the initial nucleation stage, which necessitates use of a solidifying binder. This mechanism produces granules of high porosity. It finds application in industries such as consumer goods, fertilizers, pharmaceuticals and agro-chemicals. They can be operated continuously (e.g. detergents, fertilizers) as well as in batch mode (e.g. pharmaceutical, agro-chemicals) (Ennis et al., 1997).

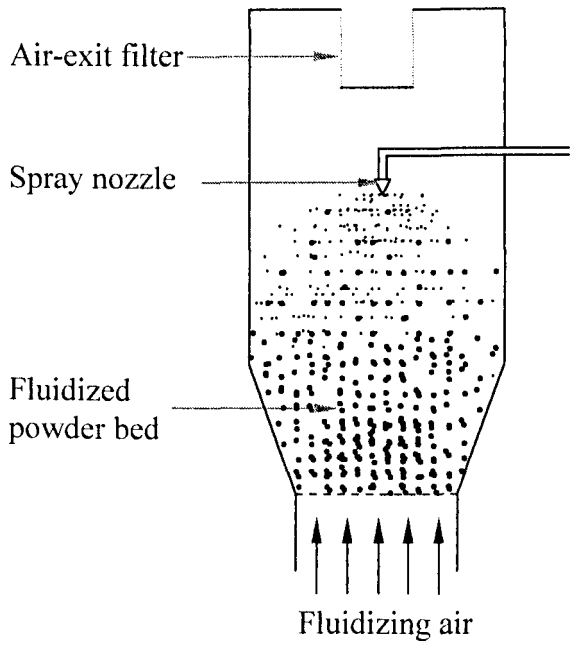

Figure 1.5: Schematic of fluidised bed granulation.

1.3.3 Mixer granulators

Mixer granulators, also known as high shear mixers, employ an agitator blade that is responsible for the powder mixing. Mixer granulators are very versatile and are used in various industries such as detergent, pharmaceutical, fertilizers, agricultural chemicals and food industries. They are capable of handling viscous material. The mixer granulator can either be a vertical axis or a horizontal axis type shown in Figure 1.6 (a) and (b) respectively. These mixer granulators employ an impeller for mechanical mixing and a chopper to improve component distribution and control granule size distribution. The end product is high density granules with relatively narrow size distribution. It is mainly used in pharmaceutical granulation and detergent powder production. Mixer granulators can be approximately divided into high shear mixers and low shear mixers (Litster et al., 2004). Pug mills and paddle mills are examples of low shear mixers that could operate at impeller speeds of lower than 100 rpm. These are being either replaced by other types of granulators or have little application in industry nowadays. It is the high shear mixers that have become popular in the industry over the years. HSG is discussed in detail in section 1.4.

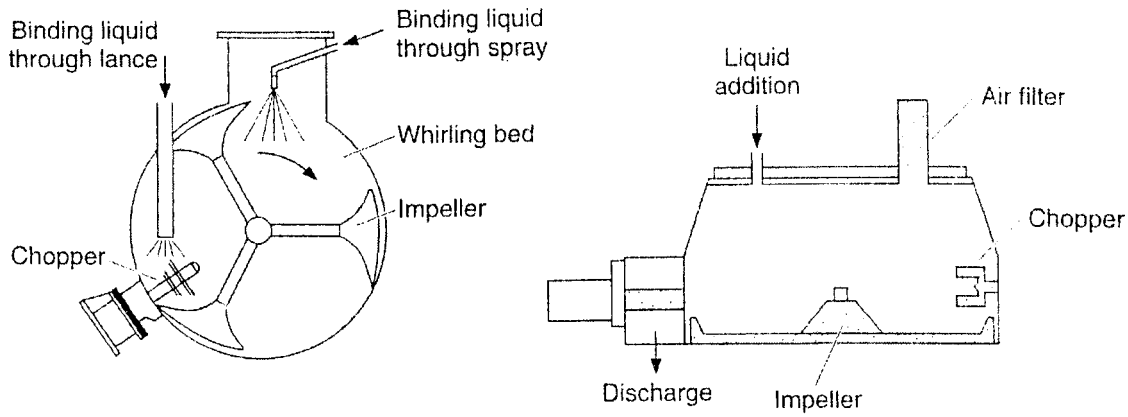

Figure 1.6: Mixer granulators (a) Horizontal axis and (b) Vertical axis type (Ennis et al., 1997).

1.4 HIGH SHEAR GRANULATION

1.4.1 Introduction

High shear granulation (HSG) is mainly used in the detergents, food and the pharmaceutical industries. High shear mixers such as the Diosna, Lodige, Fielder, Zanchetta and Moritz used in detergent and pharmaceutical industry are widely studied in the literature on HSG. Some characteristic features (advantages) of wet granulation in a high shear mixer are (Schaefer et al., 1986; Kristensen et al., 1996; Knight et al., 1998; Hoornaert et al., 1998; Russell et al., 2001; Litster et al., 2004):

- Can handle solids having a wide range of particle sizes;
- Can handle very cohesive powders,
- Provide efficient distribution of highly viscous liquids into the solid particulate material and can tolerate over-wetting,
- Short processing times,
- Space requirements for installation are low,
- Produces very dense granules (e.g. compact detergent),
- Good containment of dust and aerosols.

It also has certain disadvantages (Litster et al., 2004):

- It has high capital, maintenance and operating cost,
- Difficult to scale-up from laboratory to industry in order to maintain the product properties.

In pharmaceutical industry, HSG is employed before the tabletting operation. This step provides a uniform distribution of the active drug components in the finished product (usually tablets). The granular form of material also facilitates its flow to a tabletting press. In FMCG industry, it aids in increasing the bulk density to facilitate transport, provides uniform distribution of components in granular products and reduces dustiness while handling of products such as washing detergent.

1.4.2 Types of high shear mixers

High shear mixers can be subdivided according to the impeller shaft position or the position of mixing chamber as depicted in Figure 1.6 (Ennis et al., 1997; Knight et al., 1998; Litster et al., 2004) as:

1) High shear mixer with a horizontal impeller shaft; e.g. Lodige and plough-share mixers.
2) High shear mixer with a vertical impeller shaft; e.g. Zanchetta, Fielder and Diosna mixers.

Vertical high shear mixers produce steady-state flow as opposed to horizontal high shear mixer where the flow is periodic (Stewart et al., 2001a). Due to this the dynamics of these two systems are considerably different and so the observations in these two types of mixers can not always be correlated. On the contrary, researchers have found differences in the working of these two mixers. Schaefer et al. (1986) found that horizontal high shear mixers produce slightly denser granules than vertical counterparts. They also compared the effects of process conditions in a small horizontal Lodige high shear mixer with a vertical Fielder pilot scale high shear mixer for dicalcium phosphate. One of the key findings was that they noticed granule growth at lower moisture content in the vertical Fielder high shear mixer compared to horizontal Lodige high shear mixer.

1.4.3 Factors affecting high shear granulation

The factors that influence high shear granulation can be broadly divided as operating conditions and feed material properties. The operating conditions mainly include the agitation, process-run time, method of binder addition and the amount of binder added. On the other hand the feed material properties could be the viscosity and the surface tension of the binder and the primary particle size of the feed powder (primary particle size is the mean size of the particle size distribution of the powder).

1.4.3.1 Effect of operating conditions

From Figure 1.3 it is clear that the granule growth is a function of granule pore saturation. This also implies that the granulation can only happen for certain liquid solid ratios. This phenomenon is confirmed in the literature, such as by Knight et al. (1998). They also concluded that the different binder addition methods have major effects on the granule growth kinetics with the melt-in type of binder addition exhibiting the lowest growth rate. The agitation in a high shear mixing system is brought about by an impeller and a chopper. Knight et al. (1993) found that the mean granule size increased with the granulation time irrespective of whether the chopper was on or off. They also

found that the chopper narrowed the size distribution as the mean size increased. In further study, Knight et al. (2000) concluded that granule growth at higher impeller speed was limited by the granule breakage although they did not achieve equilibrium between the growth rate and the breakage rate resulting in a wider size distribution at high impeller speeds.

1.4.3.2 Effect of feed material properties

Keningley (1997) studied the effect of binder viscosity on granulation behaviour and found that the liquid solid ratio for a recipe to agglomerate increases with finer powder particle size. For fine grade powder, Schaefer (1996 and 2004) found the resulting granules to be of high strength and low deformability. Schaefer (2004) also concluded that in order to reduce inter-granular heterogeneity a low viscosity binder needed to be agglomerated with finer powder and a high viscosity binder for coarser powder grades. Johansen (2001) found this to be especially true when spherical agglomerates or pellets are desired and also found it to be difficult to agglomerate powder with a relatively high mean particle size of 214 μm even with a very high viscosity binder (~100 Pa.s at 80°C).

Some of the observations above are universal to all granulation processes and others are more specific to high shear granulation. It is however not always possible to correlate the parameters discussed above and the granules obtained as the studies in the literature are more specific to a particular type of equipment. The geometry and scale of the mixing equipment and the mixer fill ratio, which is the percentage volume of mixer filled with the agglomerating material, also influences the characteristics of the product granules. The results obtained are not always reproducible due to the complexity of the granulation environment and the growth mechanisms as noticed by Fu et al. (2004a). Bardin et al. (2004) attributed the batch to batch variation in properties to the variation in liquid-solid absorptivity and un-uniform distribution of liquid binder in the granules. The parameters mentioned above are the major parameters that influence granulation but are in no way exhaustive. Other parameters such as, process-run time (Hoornaert et al., 1998; Knight et al., 1998; Knight et al., 2000), mixer fill ratio (Schaefer et al., 1993), binder surface tension (Iveson et al., 1998b), vessel material (Bouwman et al., 2004) etc. also influence HSG.

2

LITERATURE REVIEW AND THEORITICAL BACKGROUND

2.1 INTRODUCTION

This chapter deals with the introduction of methods, techniques and background science utilised throughout the thesis. The sections in this chapter are divided according to their usefulness to the research objectives mentioned in section 1.1. In section 2.2, the need to measure velocities in a high shear mixer is highlighted and the relevant techniques used in literature are discussed. Section 2.3 introduces the rate based approach to modelling granulation using population balances. Sections 2.4 and 2.5 introduce two different theories (aspects) of particle motion responsible for particle-particle interaction. These theories form the basis to estimate particle-particle collision rates.

2.2 DIRECT MEASUREMENT OF VELOCITIES IN A HIGH SHEAR MIXER

2.2.1 Motivation behind measuring velocities in a high shear mixer

- The flow inside a high shear mixer determines the nature of forces acting on powder particles and granules. These forces such as shear forces and impact forces dictate the nature of interaction. This interaction between particles is responsible for coalescence and/or breakage.
- The flow behaviour in a high shear mixer directly influences the effectiveness of the mixing process. An effective mixing can optimise the granulation process by

reducing the power input, recycle ratios and reducing material waste in quality control.

- Measuring the velocities can help in understanding particle motion and fluctuations in this motion. This in turn will be useful to understand the particle-particle collision dynamics.

The two common techniques that are used by researchers are High Speed (optical) Imaging (HSI) and Positron Emission Particle Tracking (PEPT). These are discussed in sections 2.2.2 and 2.2.3 respectively.

2.2.2 High speed imaging

In HSI, images of an object are recorded at a high framing rate with an optical imaging camera. The framing rate is measured as number of images or frames recorded per second (Hz). Generally, framing rates above 50 Hz are regarded as high speed. High speed imaging is discussed in detail in section 3.2. It is also necessary to note here that the observations made with a high speed camera are limited to surface observation of the powder/granular bed only and inferences are made based on this.

Ramaker et al. (1998) investigated flow of pellets in a 0.25 L coffee grinder and a 8 L Gral high shear mixer. They used a stroboscope to obtain two or more images of a pellet in one photo. The frequency and errors in their method of finding pellet velocities is not apparent from the research paper. Although the frequency of imaging is not mentioned to be categorized as high speed, the method was first of a kind that made use of imaging technique to investigate velocities in a high shear mixer. They found a toroidal flow in both the high shear mixers. In case of coffee grinder, the velocities tended to increase from the wall towards the centre in the range of 0.15 m/s to 0.4 m/s. This range didn't show much difference at different impeller speeds of 82 and 187 revolutions per second. These velocities can be considered as to be more specific to the size of equipment investigated.

Hapgood (2000) measured powder surface velocities in a Hobart mixer. The powder was 1.7kg of Wyndale 1000 mesh lactose and filled to approx $\frac{1}{4}^{th}$ of the mixer volume. The powder surface motion was recorded with a Sony BW CCD camera at 25 fps for 4

seconds. The lumps and cracks in powder bed were tracked with MetaMorph® image processing software (Universal Imaging Corporation, PA, USA). Several impeller speeds from 150 to 750 rpm were investigated that showed a general increasing trend in powder surface velocities with an increase in impeller speed.

Muguruma et al. (2000) used 'Particle velocimetry tracking' technique to validate the results obtained from a DEM (Discrete Element Modelling) simulation of particle flows in a centrifugal tumbling high shear mixer. Although they termed it as a tumbling high shear mixer (376 mm diameter), it was indeed a vertical axis high shear mixer equipped with a disc impeller. The mixer was operated at 300 rpm impeller speed. A high-speed VTR system (Figure 2.1) was used at a speed of 250 images per second to record particle flow.

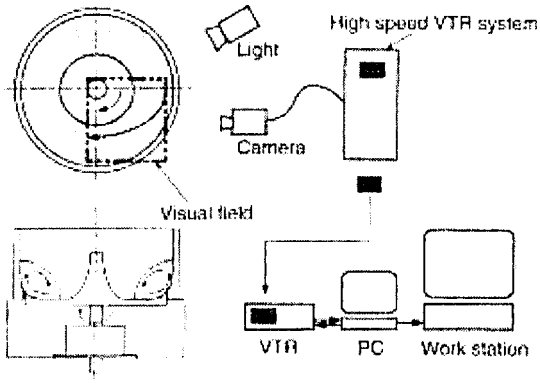

Figure 2.1: Schematic diagram of apparatus for particle velocity measurement used by Muguruma et al. (2000).

White Alumina beads (1.90 mm, 3.98×10^3 kg/m^3) were used as tracer particles with the brown grass beads (1.92 mm, 2.52×10^3 kg/m^3) as test particles. A polarized filtering technique was employed to distinguish the tracer particles from test particles (Figure 2.2). This figure also shows an accumulation of bulk material near the mixer wall in the side view of the mixer cross-section. The bulk material also exhibited a toroidal flow with the powder moving towards the wall at the bottom of the impeller and falling towards the mixer centre on the surface of the bed.

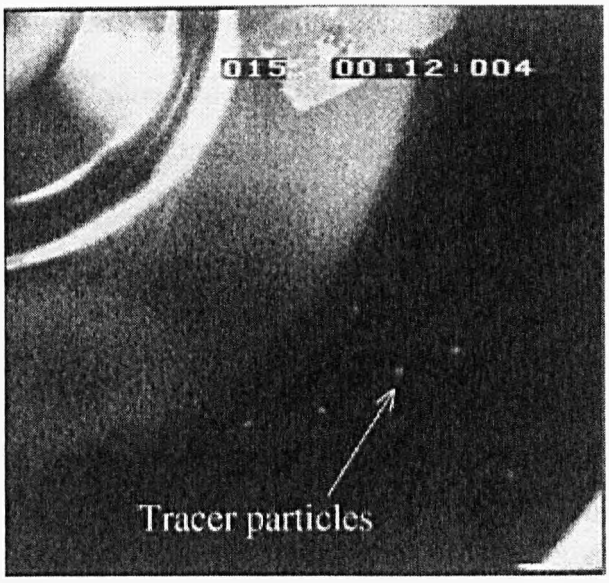

Figure 2.2: Example of an image of visual field with number of tracer particles (Muguruma et al., 2000).

The particle velocities were obtained by comparing particle positions from consecutive images. Out of the three components of the particle velocity, only two components, the circumferential component (v_θ) and the radial component (v_r), were measured. The particle velocities were plotted against the non-dimensional distance *r/R* (Figure 2.3), where *r* is the particle position from the centre of the rotor and *R* is the stator radius. From Figure 2.3, it can be interpreted that the magnitude of circumferential velocity was approximately ten times the radial velocity. These findings lacked the time resolved velocity variation of particles as it was primarily meant to validate the results of DEM simulation.

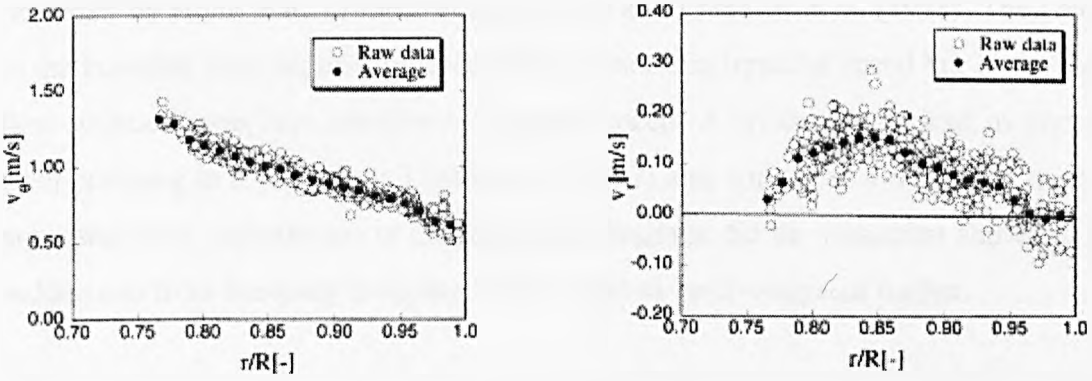

(a) Circumferential components of particle velocity. (b) Radial components of particle velocity.

Figure 2.3: Experimental data of particle velocity profile (Muguruma et al., 2000).

Litster et al. (2002) measured powder velocity in a 25 L PMA Fielder mixer. The aim of their powder velocity measurement was to estimate A, the area flux of powder traversing the spray zone that was used in dimensionless spray flux Ψ_a formula (Litster et al., 2001) given as:

$$\Psi_a = \frac{3\dot{V}}{2Ad_d} \tag{2.1}$$

where, $\dot{V}$ is volumetric spray rate and d_d is droplet diameter. The dimensionless spray flux (Ψ_a) was used to characterize the different nucleation regimes. The powder flow was filmed with a high-speed video camera at 500 frames per second. The camera was kept tilted at 45° centered on the spray zone. The flow pattern was measured for a batch of 6-kg dry lactose powder and wet lactose (approx. 6% moisture) at impeller speeds between 100 and 500 rpm. The images were analyzed with MetaMorph® image processing software (Universal Imaging, PA, U.S.A.). They noticed that the powder bed did not fluidize and its movement could be followed by using the natural bed structure (lumps and cracks in the packed bed). The position of a lump of powder was followed over a number of frames and scalar velocity was calculated by the software. An average of all velocity results was used. They observed two distinct flow regimes (Figure 2.4). First, the '*Bumping flow*' in which the powder surface remains horizontal and the bed bumps up and down as the impeller passed underneath. In the second flow regime, which they attributed as '*Roping flow*', the powder from the bottom is forced up the vessel wall and then tumbles down towards the center, similar to flow mentioned as 'toroidal' by Holm et al. (1996), Wellm (1997) and Ramaker et al. (1998). The velocity in the bumping flow regime increased with increase in impeller speed but in the roping flow regime it was less sensitive to impeller speed. A break was noticed in transition from bumping to roping flow. Litster et al. (2002) also suggested a transition stage and proposed more experiments to confirm these findings. So the transition shown to be a sudden one from bumping to roping flow needed to be investigated further.

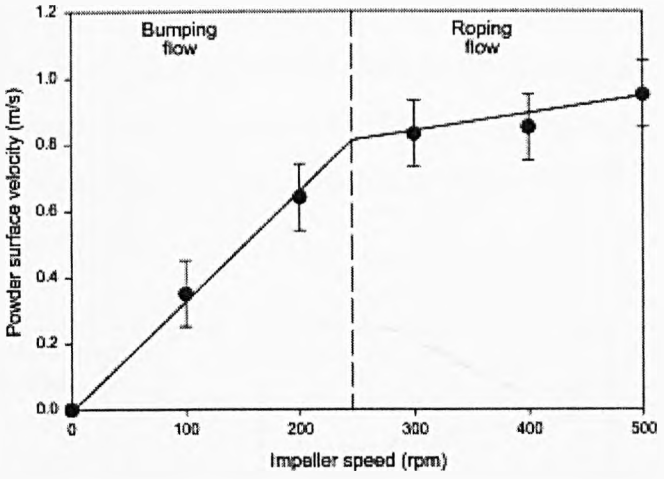

Figure 2.4: Powder surface velocities as a function of impeller speed (dry lactose), (Litster et al., 2002).

Plank et al. (2003) carried out similar work to that of Litster et al. (2002) to emphasise the importance of dimensionless spray flux in scaling up of wet granulation processes. They modified dimensionless spray flux (Eq. 2.1) as:

$$\Psi_a = \frac{3V}{2vWd_d} \tag{2.2}$$

where v is the velocity of powder moving through a spray zone of width W. A high-speed video camera that had framing rate of up to 500 Hz was used to measure the surface velocity of powder beds. The velocity was measured in three Aeromatic-Fielder high shear mixers of 25 L, 65 L, and 300 L volume fitted with plexiglass lids at various granulating conditions. The video clips were recorded for 5 s each. Only tangential component of surface velocity was calculated by tracking tangential movement of the powder frame-by-frame. The frame of reference was established with an image of ruler positioned inside the mixer. The powder used contained mixture of lactose monohydrate (55.9% w/w), microcrystalline cellulose (26.6% w/w), sucrose (12.2% w/w), and pre-gelatinized starch (5.7% w/w). USP (United States Pharmacopoeia) water was used as a binder. Average surface velocity was measured as a function of impeller speed (Figure 2.5), granulating liquid (water) level (Figure 2.6), and fill level. Surface velocity increased with increasing impeller speed. This effect was profound for 300 L mixer but for 25 L and 65 L mixers it showed a flat increase beyond standard low speed. A sudden increase in velocities was noticed with a transition from powder to sticky/cohesive and agglomerated phase as in Figure 2.6. The fill level had a negative effect on average

surface velocity and slowed the bed by approximately 60-70% for a fill level (*h/D*) change from 0.26 to 0.33. They also observed that the powder bed surface remained motionless for a fraction of the interval required for consecutive impeller blades to pass beneath the surface of the bed. This phenomenon was detectable for higher fill levels in the 65 L and 300 L mixers.

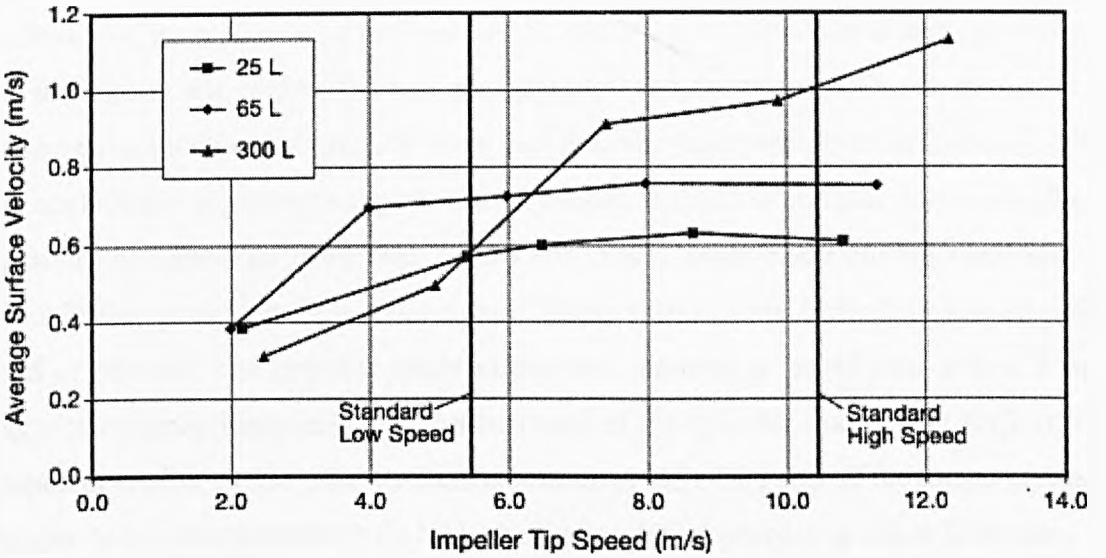

Figure 2.5: Surface velocities compared across the 25-l, 65-l, and 300-l mixers at 7%w/w granulating liquid (Plank et al., 2003).

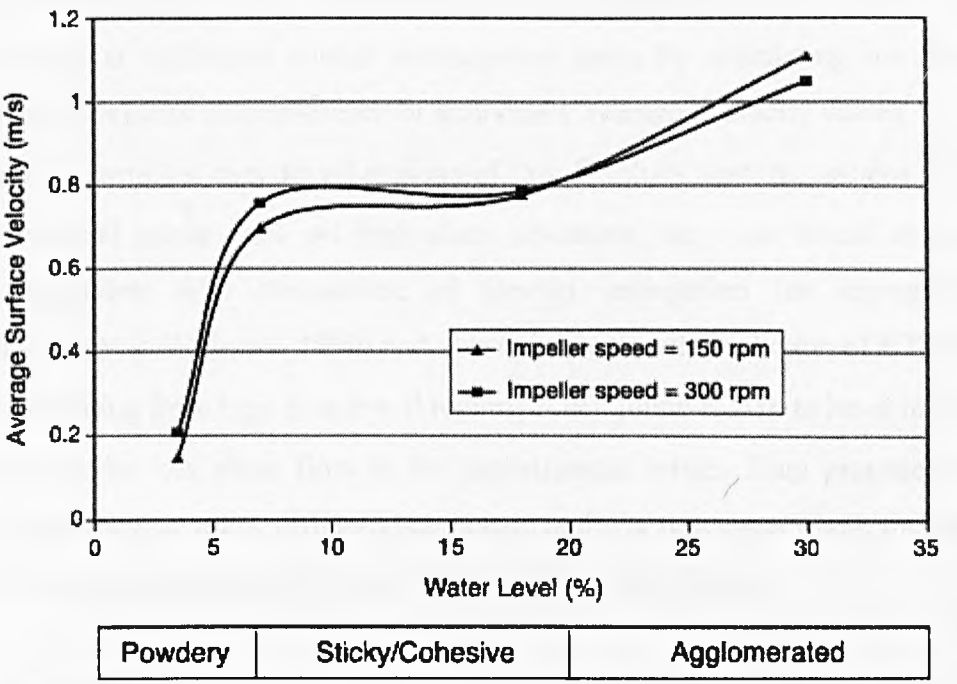

Figure 2.6: Surface velocity as a function of granulating liquid level in a 65-l mixer (Plank et al., 2003).

Coinciding with this research, Conway et al. in 2005 published their study wherein they used 2D particle image velocimetry (PIV) to look at a granular flow in a vertical cylinder equipped with a four bladed impeller. They used near-monodisperse dry art sand (size range 355 to 425 μm) for flow characterization and mixture of varying diameter glass particles to understand granular segregation (segregation is referred to the phenomenon of physical separation of granules of different sizes under dynamic conditions). The blades were inclined at 45° and could be moved in either direction so that the blades can move through the granular bed in either acute or obtuse way changing the direction of granular flow and thus the equipment type imitated. Motion with acute blade angle was suggested to be similar to the flow in filter dryers, results of which are not discussed here. The results for obtuse angle blade motion were said to resemble the motion in high shear mixer. These results were limited to low impeller speed of 50 rpm. The impeller blade radius was reported to be 45 mm with a 5 mm clearance between blade edge and vertical wall of the cylinder making the scale of the equipment similar to that used by Ramaker et al. (1998). The size of the mixer makes it arguable to be representative of a high shear granulation process in either laboratory or industrial scale. The importance of mentioning this research here is the resemblance in terms of use of PIV for granular flow in a mixer-like configuration and the key methodologies and observations. They stressed on applicability of Kinetic Theory of Granular Flow (KTGF). They calculated granular temperature (θ, refer to section 2.4.1 for definition) at individual spatial interrogation areas by calculating instantaneous fluctuations in velocity with reference of temporally averaged velocity values. For near-monodisperse particles, they found regions of low θ values near the agitator shaft and near the vertical mixer wall. At high shear operation, they also found segregation patterns consistent with mechanism of sieving segregation (or segregation by percolation; refer to Williams, 1990) and also consistent with prediction of KTGF about particles migrating from high θ to low θ regions. They found KTGF to be of limited use for describing the low shear flow in the experimental mixer. They proposed further work on different size units, different geometries and real processes where the presence of a second phase such as liquid solvent/binder affects the process.

Limitations of PIV:

1. PIV technique lacks the 3D spatial investigation capability in opaque systems. And this is the strength of the PEPT technique. Even the modern 3D variants of PIV

(Stereographic PIV) systems can not probe opaque systems and they can only investigate limited depth in transparent systems.

2. A higher spatial resolution comes at the expense of lower temporal resolution and vice versa. This shortcoming is being addressed with new developments in digital imaging. This shortcoming is also evident in the current research as the earlier experiments in Chapter 3, 4 and 5 are at a relatively lower spatial resolution as compared to experiments in Chapter 6 due to limited availability of newer cameras in the EPSRC-EIP (2006) at the time.

The velocities on the bed surface are expected to be lower in magnitude than that near the impeller. Stewart et al. (2001a) found granular velocities approaching the impeller speed near to the impeller in their studies involving Positron Emission Particle Tracking (PEPT). So it is plausible to assume that the granular velocities will not exceed the maximum impeller tip speed and also that there will a distribution of velocities from the impeller to the surface of the granular bed.

2.2.3 Positron emission particle tracking (PEPT)

The Positron Emission Particle Tracking (PEPT) technique has been developed and used since the early 90s (Broadbent et al., 1993; Parker et al., 1993; Laurent et al., 2000; Parker et al., 2002). PEPT is a variant of Positron Emission Tomography (PET) widely used in medicine and has been modified to investigate the flow structure inside various particle flow systems. It is a non-invasive method for tracking motion of a particle inside an opaque system. The PEPT uses a single tracer particle that can be followed in time and space. The tracer particle can be an artificial proton-rich isotope such as ^{18}F, ^{22}Na, ^{68}Ga and ^{64}Cu. Such isotopes decay to produce a neutron (n), a positron (e^+) and a neutrino (ν). The emitted positron carries the energy of about 1 MeV and gets annihilated in 1 ps by inelastic collision with an electron in the surrounding medium. The collision produces two opposing collinear 511 keV gamma rays. Two detector plates placed at specified separation detect the rays. The direction of gamma ray emission changes and triangulation of two or more successive events enables the system to locate the tracer. Such location monitoring when associated with time enables tracing the particle path and calculating velocity, acceleration, and residence time distribution. Gamma ray with 511 keV energy is capable of penetrating through casings of industrial

equipment (Broadbent et al., 1993). Stewart et al. (2001a) reported a practical limiting speed for tracer tracking to be 2 m/s. The accuracy improved to tracking within 1 mm at speeds up to 5 m/s as reported by Forrest et al. (2003).

Wellm (1997) used PEPT for high shear mixer (Diameter 0.285 m) to establish a general view of the flow pattern of the particulate material. The powder was found to be moving in the direction of the running blade with no exception. The powder was moving much slower than the blades, even near to the blades where the tip-speed was about 14.1 m/s. The velocities were calculated in a horizontal and a vertical plane. The particulate mass was performing a toroidal vortex motion. The vortex motion was outward in the lower regions of the mixer and inward in the upper regions, rising at the wall and falling near the axis of the mixer. This data was analysed with Fast Fourier Transform (FFT) that showed a peak at a frequency 0.9 s^{-1} corresponding to a maximum tangential velocity of 0. 85 m/s near the outer perimeter. With the FFT analysis it was found that the speed of the solids depends on blade speed and design, properties of the solids and level of fill. The tip speed and the speed of the powder had ratios as large as 100:1 that became smaller with the smaller blade speed. For experiments done with a disc impeller at different speeds, the peaks for the horizontal motion were in the identical place. It was inferred that the speed of the disc has no significant effect on the movement of the powder and so coefficient of friction is independent of the velocity difference between blade and powder. Wellm (1997) suggested that insensitivity of granular velocity to the disc impeller speed could be due to slippage between the granules and the disc.

Stewart et al. (2001a) investigated particle flow in a vertical stirred high shear mixer equipped with a two-bladed impeller using PEPT technique. The mixer had a diameter of 249 mm making the scale similar to that used in this thesis (D = 285 mm). They used spherical glass beads with size range 2 to 2.4 mm. The tracers were made of same material within a size range 2.17 to 2.23 mm. They performed experiments at varying bed mass (1.4 to 7 kg) and at varying impeller speeds (10 to 160 rpm). The major finding of their study was the 3D recirculation of particle that decreased with increasing fill level and impeller speed. Increase in blade speed also expanded the volume of bed material and increased mechanical agitation. Similarly, Knight et al. (2001a) verified

results for mixer torque modelling with experiments carried out with PEPT measurements in a vertical high shear mixer for bladed as well as disc impellers.

PEPT has some limitations (Wellm, 1997, Bridgewater et al., 2003):

1. It is not suitable for unsteady-state systems.
2. Since only one particle can be tracked, each location in the equipment needs to be visited several times for better statistics of occupancy and velocity distributions.
3. The tracer particle needs to be of certain size and material to contain radioisotope that will give enough emitting nuclei. This causes problems such as differences in size and density of the tracer and the surrounding material. This leads to segregation and therefore misrepresentation of speeds within the vessel.
4. The thickness and density of the material of construction of the equipment and the material under investigation may cause scattering and signal attenuation of the γ-rays. Scattering leads to wrong locations and attenuation to a loss of the signal.
5. The spatial resolution degenerates with the increasing speed of the tracer particle.

Other limitation such as extended experimental time has been addressed by increasing the positron camera sensitivity and improving data delivery rate in recent developments of PEPT technique. Tracer particle with sizes as small as 100 μm have been reported in the literature (Bridgewater et al., 2003). It might take some time for PEPT to catch up with PIV in terms of spatial and temporal resolution and accuracy. A combination of both techniques would be ideal to investigate particulate flow. But until then either technique will get preference based on the aim of the experiment and the parameters to be investigated in a system.

2.3 MODELLING GRANULATION

2.3.1 Introduction

Four mechanisms: Nucleation, Growth, Aggregation and Breakage have been identified as the main mechanisms that would influence particle size distribution (PSD) during granulation process (Hounslow, 1998). These processes are previously described in section 1.2.1, except aggregation, which is synonymous with the coalescence process and generally assumes a two-body interaction. Population Balance Modelling (PBM) is

a technique that has been popularly used to help understand particulate processes. It has widely been used as a rate based approach to describe the granulation process and extract the rate constants from the granule size distribution changes. By this approach it is possible to characterise the granulation process by a single parameter such as a rate constant (discussed below). Due to the difficulty in solving all four mechanisms (that influences PSD) at a time, normally only binary aggregation is modelled (Hounslow, 1998). However new algorithms developed by Hounslow (2002) can simultaneously solve aggregation and breakage.

The population balance model for granulation is based on certain assumptions:

- Granules are spherical.
- Binder is distributed equally over all granules in one size range.
- Each granule has a uniform composition in terms of its components.

PBM for granulation also does not take into consideration the amount of binder available on the surface for effective aggregation of colliding particles such as that included in model proposed by Ennis et al. (1991) based on collisional dissipation of relative particle kinetic energy. It would also seem that the collision rates (and so the aggregation rate) inside a mixer would vary as a function of position due to varying granule size distribution throughout the mixer. However due to intense mixing characteristics of high shear granulator, the granules of different sizes can be assumed to be evenly distributed throughout. This assumption also results in conclusion that granular temperature will not vary much throughout the bed except near to the impeller where the particle velocities are considerably higher (Stewart et al., 2001a). So the problem reduces only to measuring the granular temperature throughout the mixer. Due to the limitations of the current investigating technique only surface observation will be made and some inferences will be made on situation inside the granular bed later on in the thesis.

The rate of aggregation can be defined as:

$$r_{agg_{i,j}} = \beta_{i,j} N_i N_j \tag{2.3}$$

where N_i and N_j are the number concentration in the size classes i and j respectively and β is the aggregation rate constant or kernel.

The aggregation rate constant can be split into efficiency and a collision rate constant as (Ramakrishna, 2000; Biggs et al., 2003; Tan et al., 2004):

$$\beta_{i,j} = \psi_{i,j} \times (collision\ rate\ const.) \tag{2.4}$$

The $\psi_{i,j}$ is the aggregation efficiency and can be defined as the fraction of the total number of collisions between particles of sizes i and j that produce successful aggregation. This equation also signifies that the aggregation is a process of collision. The collisions between particles depend on the kinematics of the motion and so the need to study it.

The aggregation rate, $\beta(u,v,t)$, can be separated into the time dependent rate constant and the size dependent kernel as (Sastry, 1975):

$$\beta(u,v,t) = \beta_0(t)\beta^*(u,v) \tag{2.5}$$

where β_0 is the aggregation rate constant and $\beta^*(u,v)$ is the aggregation or coalescence kernel. The β_0 is a lumped parameter that can be considered to be a complex function of the wide range of equipment, material and operating parameters existing in a granulator. This is often determined semi-empirically through fitting of experimental data. The $\beta^*(u,v)$ describes the expected aggregation rate as a function of granule size. This presents the problem of selecting a suitable physically based kernel. A wide range of aggregation kernels have been proposed in the literature with some based on physical models and others empirical.

There are mainly two kernels described in the literature for calculating particle-particle collision rates in granular flow. These are namely, Equi-partition of Kinetic energy Kernel (EKK) described in section 2.4.2 and Smoluchowski Shear Kernel (SSK) described in section 2.5.2. By comparing these two models it would be possible to infer the closeness of the models to the physical situation in high shear granulation. Tan et al. (2004) found that the EKK provides a good description of the granule size distribution in fluidised bed granulation. They showed that the velocity distribution in a fluidised bed was consistent with KTGF and hence the EKK should be expected to provide a good description of the aggregation rate. The SSK seems a natural choice for the size dependent kernel when modelling HSG, due to the anticipated shear field in the high shear mixer, although it has been shown to provide a poor description of the granule

size distribution in HSG by Hounslow et al. (2001). This size dependent SSK favours large-large granule interactions.

2.3.2 Population Balance Equation

A granule is generally made of liquid, solid and air making it a three dimensional (3-D, phase space) population balance problem (Biggs et al., 2003). Scott et al (2000b) has shown that the trapped air volume tends be very small after initial compaction of granules making the problem 2-D with solid and liquid as modelling parameters. If the distribution of liquid in granule is assumed to be uniform irrespective of the granule size then the problem reduces to a simplified 1-D problem. (The different dimensions in this context refer to the phases, liquid, solid and air).

A 1-D size population balance for aggregation alone expressed for the number per unit volume, n, of granules of size v at time t can be written as follows (Biggs et al., 2003):

$$\frac{\partial n(v,t)}{\partial t} = \frac{1}{2}\int_0^v \beta(u, v-u, t)\, n(u,t) n(v-u,t) du - n(v,t)\int_0^\infty \beta(u,v,t) n(u,t) du \qquad (2.6)$$

where $n(v,t)$ is the number density of particles of volume v, at time t. The first part of Eq. (2.6) is the *Birth rate* and the second part is the *Death rate*. β is a measure of collisions between particle of volume u and v that successfully aggregate to form particle of size $u+v$.

2.3.3 Solving population balance equation

Several methods of solving a population balance equation have been described in Ramakrishna D. (2000). Among the methods described in this reference, the method of discretizing population balance (DPB) equations and solving the discrete equations numerically provides rapid solution of selected properties of a population (Ramakrishna D., 2000).

The population balance equations in this thesis were solved using a discretised population balance model for binary aggregation described by Hounslow et al. (1988), where the rate of change in the number of particles in the size interval i is given by Eq.

(2.7). This model has been widely used in the PBM of high shear granulation (Biggs et al., 2003; Sanders et. al., 2003; Darelius et al., 2005) and fluidised bed granulation (Tan et al., 2004).

$$\frac{dN_i}{dt} = N_{i-1}\sum_{j=1}^{i-2}\left(2^{j-i+1}\beta_{i-1,j}N_j\right)+\frac{1}{2}\beta_{i-1,i-1}N_{i-1}^2 - N_i\sum_{j=1}^{i-1}\left(2^{j-i}\beta_{i,j}N_j\right)-N_i\sum_{j=i}^{i_{max}}\beta_{i,j}N_j \quad (2.7)$$

Above Eq. 2.7 was solved in a DPB package in *Mathematica* written by M.J. Hounslow (2002). The input to this package is a GSD at different time intervals during granulation in a spreadsheet format. For simulating results the package takes the initial condition as the GSD in number format on a $\sqrt[3]{2}$ progression at the starting time. The rate law is also defined before starting the package, which is the active mechanism that influences the granulation and the dependence on size and time defined by the aggregation kernel.

2.4 KINETIC THEORY OF GRANULAR FLOW (KTGF)

2.4.1 Introduction

Granulation involves various complex processes and transformations. The interdependence of these complex processes adds to the complexity of the process. There is no single model that can predict the distribution of granule product properties such as size, shape, particle density and composition. Most granule growth models use average values of process parameters. The Kinetic Theory of Granular Flow is one such tool that has been used by many researchers to model the dynamics of granular systems. Examples can be found for high shear granulation in the work of Hounslow et al. (1998 and 2001) and Conway et al (2005). Similarly it has also been used for fluidized bed granulation by Goldschmidt (2001), Goldschmidt et al. (2002) and Tan et al. (2004).

In a granular flow, the mean mechanical energy of flow is first transformed into random particle motion and then dissipated into internal energy (Ogawa et al., 1980), as depicted in Figure 2.7. KTGF describes the mean and the fluctuating motion of particles within a continuous granular medium (Goldschmidt et al., 2001). This theory is a continuum model, basically an extension of classical kinetic theory of dense gases (Chapman and Cowling, 1970), which takes non-ideal particle-particle collisions and

gas-particle drag into account. KTGF assumes 'molecular' chaos, as in the classical kinetic theory of gases. This implies that:

(i) All particles are homogeneously distributed within an ensemble,

(ii) The particle velocity distribution for all particles is isotropic, and

(iii) The velocities of two particles involved in a collision are independent of each other.

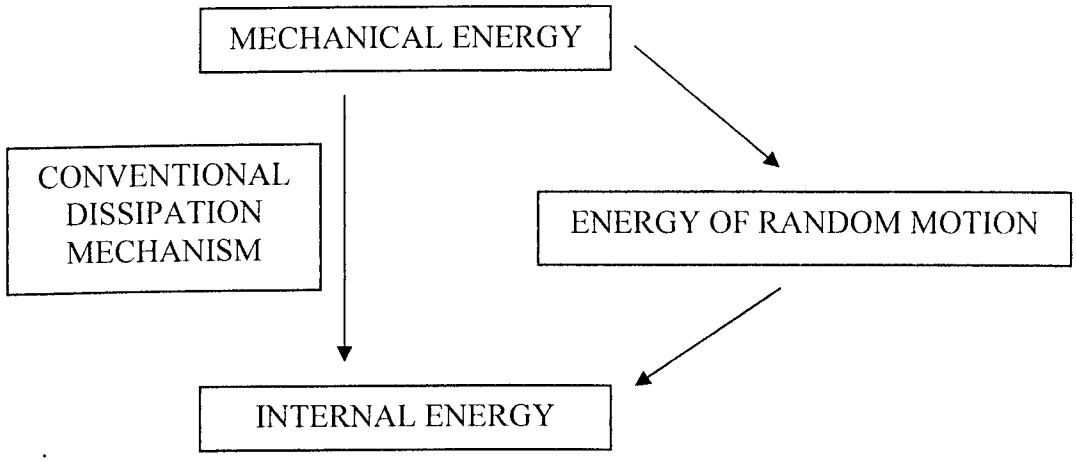

Figure 2.7: Energy flow in granular and particulate multiphase flows (Ogawa et al. 1980).

Random fluctuating component of velocity

In KTGF the actual particle velocity c (m.s^{-1}) is decomposed in a local mean velocity v (m.s^{-1}) and a random fluctuating velocity C (m.s^{-1}) (Gidaspow, 1994).

$$\bar{c} = \bar{v} + \bar{C} \tag{2.7}$$

Granular temperature

Associated with the random motion of the particles, a pseudo temperature called granular temperature, θ, analogous to the temperature of gases in the classical kinetic theory of dense gases, is defined as one-third of the mean square velocity.

$$\theta \equiv \frac{1}{3}\left\langle \bar{C}.\bar{C} \right\rangle \tag{2.8}$$

Particle velocity fluctuation

In the ideal case for KTGF, the distribution of speeds should be Maxwellian and the velocity fluctuations in each direction should be Gaussian (Eq. 2.9).

$$f(C_{X,Y,Z}) = \frac{1}{\sqrt{2\pi\theta_{X,Y,Z}}} \exp\left[-\frac{C'^2_{X,Y,Z}}{2\theta_{X,Y,Z}}\right] \tag{2.9}$$

In this case, the granular temperature is the square of the standard deviation (or variance) of the Gaussian distribution. As KTGF assumes random behaviour of fluctuating particle component, it will be mandatory to decompose the velocities in mean motion component and fluctuating component. The logical steps for this decomposition will be discussed in relevant following sections.

2.4.2 Equi-partition of Kinetic energy Kernel (EKK)

Hounslow (1998) described an aggregation kernel assuming equi-partition of kinetic energy which assumes that particles collide as a consequence of their random component of velocity and that the random component results in equal distribution of the particles' kinetic energy.

$$\beta(l_i, l_j) = (l_i + l_j)^2 \cdot \sqrt{\left(\frac{1}{l_i^3} + \frac{1}{l_j^3}\right)} \tag{2.10}$$

Goldschmidt et al. (2001) derived an expression for the collision rate between two particles from KTGF from which Tan *et al.* (2004) derived an aggregation kernel:

$$\beta_{i,j} = \psi g_{i,j} \sqrt{\frac{3\theta_S}{\rho}} (l_i + l_j)^2 \sqrt{\frac{1}{l_i^3} + \frac{1}{l_j^3}} \tag{2.11}$$

where, ψ is the aggregation efficiency (i.e. the fraction of collision events that result in aggregation), $g_{i,j}$ is the radial distribution function, and θ_S is termed the mixture granular temperature. This is synonymous with the description of temperature in the kinetic theory of gases:

$$\theta_S = \frac{1}{3} m_n \left\langle \overline{C} \cdot \overline{C} \right\rangle = m_n \theta \tag{2.12}$$

where m_n is the mass of the particle (or granule).

Comparison of Eq. 2.10 with Eq. 2.11 shows that the size dependent part of this expression is clearly the EKK, with the time dependent term given by:

$$\beta_0 = \psi g_{i,j} \sqrt{\frac{3\theta_S}{\rho}} \tag{2.13}$$

The aggregation efficiency (ψ) in above equation depends on particle wetness, particle collision velocity, particle composition and position in the bed (Goldschmidt, 2001). The exact dependence of aggregation efficiency on process parameters or a model is not available in the literature.

2.5 SHEAR FLOW

2.5.1 Theory of shear flow

Smoluchowski (1917) calculated collision rate for small particles based on two different kinds of motion, the orthokinetic motion and the perikinetic motion. In orthokinetic motion, collision between particles is induced by shearing motion of the total assembly of particles. Shear flow is exhibited in a granular flow when the adjacent layers under the influence of a force move with a velocity gradient. As in Figure 2.8, the shear rate $\dot{\gamma}$ can be defined as the velocity gradient. In the perikinetic motion, the motion of particles arises from the collisions between the particles and the molecules of the liquid. This type of motion can be found in liquids with suspended particles. It is the orthokinetic motion that can supposedly depict the motion of particles in a high shear mixer.

In orthokinetic motion it is assumed that:

- The particles follow the fluid streamlines;
- The fluid streamlines are undisturbed by the presence of particles.

The second assumption is absurd as the particles need to collide in order to aggregate for which they need to disturb the streamlines. Hounslow (2005) counters this argument by citing the work of Mason and co-workers that "*neglecting the effect of attractive forces between particles quite neatly cancels out the tendency for particles to move around each other due to lubrication effects*".

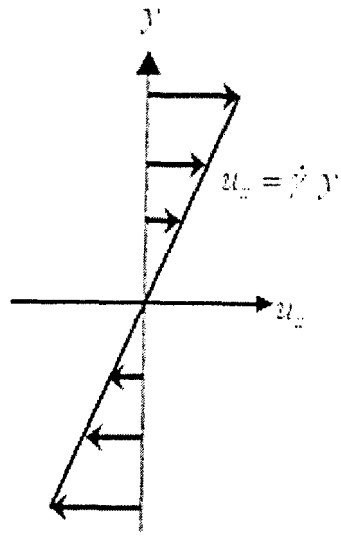

Figure 2.8: Velocity profile in a shear flow.

2.5.2 Collision frequency based on shear

The particulate motion in shear flow can be understood by an example between a big particle (at rest) surrounded by moving smaller particles (Figure 2.9). The small particles will collide with the big one only when their path passes through the collision cross section of the bigger particle. Collision cross section is the diameter equal to addition of diameters of both colliding particles. Smoluchowski (1917) presented a kernel (Eq. 2.14) describing the size dependent collision frequency of particles of sizes l_i and l_j in a laminar shear field:

$$\beta_{SSK} = \frac{\dot{\gamma}}{6}\left(l_i + l_j\right)^3 \tag{2.14}$$

The $\dot{\gamma}/6$ part of Eq. 2.14 is the size independent collision rate constant. This kernel will be referred to as Smoluchowski Shear Kernel (SSK) during further discussions.

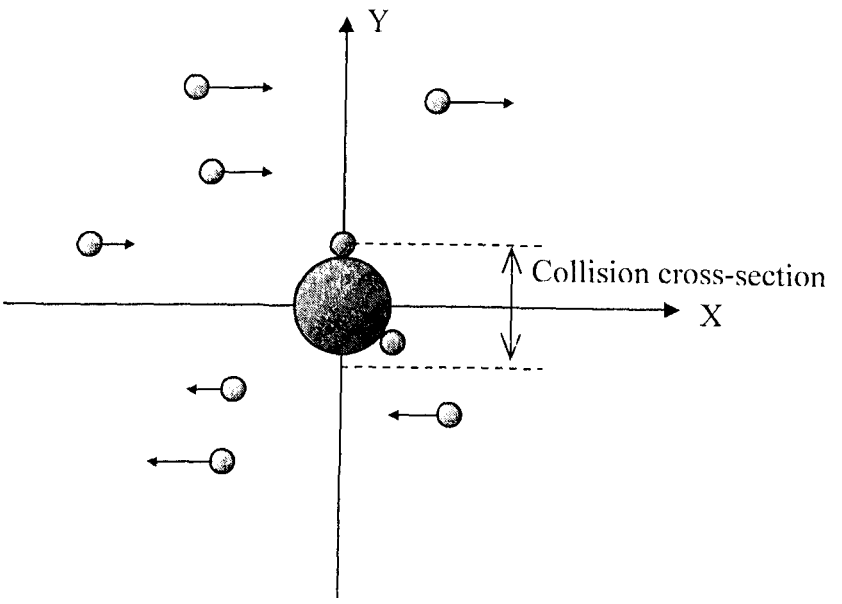

Figure 2.9: Depiction of particle-particle collisions in a shear flow.

2.6 RESEARCH OBJETIVE RE-VISITED

A generalised theory for granulation is possible only when the processes happening at granule and even smaller (micro) level are studied and the effect at batch (meso) level and further up to the equipment level (macro level) are correlated. This takes us back to the motivation behind this research thesis. This need indeed has been identified by many researchers (Ennis, 1996; Tardos et al., 1997; Hounslow et al., 2001; Knight, 2001b; Biggs et al., 2003; Sanders et al., 2003; Knight, 2004; Reynolds et al., 2004; Björna et al., 2005).

The objectives of this research can be listed as:

1. To develop a cost-effective method to investigate kinematics in HSG considering the drawbacks of previous techniques used in the literature.
2. To understand the effect of operating conditions and material properties on the mean flow and the particle motion behaviour.
3. To understand the mechanisms of collisions between particles and to estimate the collision rate based on the knowledge of surface velocity observations.
4. To estimate the aggregation efficiency based on the knowledge of third objective (as above) to form the basis of a predictive high shear granulation model.

Once the effect of the operating parameters on the kinematics inside the high shear mixer is understood and the dominant particle collision mechanism is known, the operating parameters can be correlated to the collision rates and later on to the aggregation efficiencies provided suitable aggregation models are available or developed.

Chapter 3 develops the understanding of the analysis method developed in this research. Chapter 4 serves the aims listed in objective 2 where the effect on kinematics of factors such as binder viscosity, granule size etc. is investigated in-depth. Two mechanisms of particle-particle collisions are studied and collision rates are estimated in chapter 5 for a system of high shear mixer equipped with a disc impeller. Chapter 6 is aimed at estimating aggregation efficiencies in a wet granulation experiment with the 3-blade impeller in the high shear mixer. Whereas, in chapter 7 the conclusions drawn from this research are discussed and future recommendations are listed.

3

TECHNIQUE AND ANALYSIS DEVELOPMENT OF VELOCITY MEASUREMENT

The aim of the experiments was to investigate the mean and the granular velocities (velocities depicting the velocity of single granule) and the flow pattern inside the high shear mixer (HSM). The velocities obtained would also be used to calculate the fluctuations in particle velocity, which will help in understanding the particle-particle collision rates. The idea is to record the images of the moving granular bed in the HSM with a high speed camera (HSC) and analyse the consecutive images to determine the granular velocities with Particle Image Velocimetry software. There were two PIV software routines used namely VidPIV3® software (Optical Flow Systems, Penicuik, Scotland) and PIV toolbox ('mpiv') available in MATLAB (Mori et al., 2003). VidPIV3® uses a cross-correlation algorithm whereas MQD algorithm was used in analysis with 'mpiv'. The raw velocity data from this analysis was processed with a code written in 'C++'. Further analysis was done in the 'Mathematica' software package. This method of technique and analysis development is discussed in this chapter.

3.1 EXPERIMENTAL SET-UP

3.1.1 Apparatus

A Zanchetta high shear mixer (Figure 3.1) with a nominal volume of 10 L was used as the experimental mixer. It was equipped with a detachable impeller on the central shaft that can revolve up to a speed of 900 rpm. The 3-blade impeller was used as the primary experimental impeller. Another impeller was custom made in the shape of a disc type impeller for separate experiments (in chapter 5). A chopper blade is attached to the lid of the mixer and has a maximum rotational speed of 1400 rpm. The mixer was 285 mm in diameter and 175 mm in height and was attached with a discharge chute for the removal of product at the bottom corner. There was an opening in the mixer lid to add binder on the moving powder bed. The heating jacket in the mixer wall could heat it up to a temperature of 80°C.

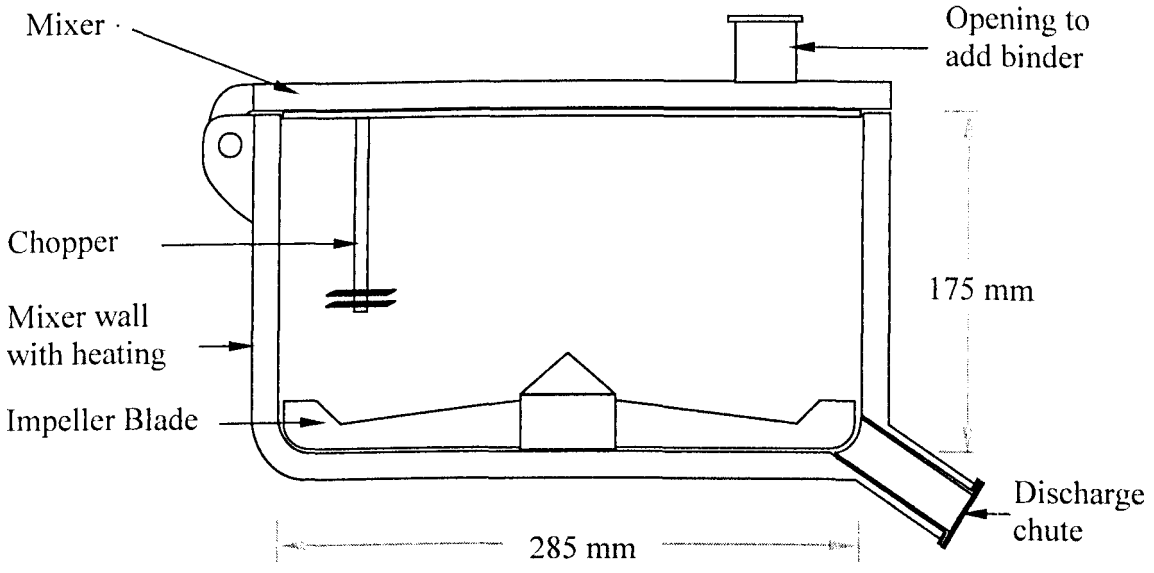

Figure 3.1: Schematic diagram of 10l - Zanchetta high shear mixer.

3.1.2 Set-up

Due to the centrifugal force exerted by the impeller on the powder (granules), most of the time the powder gets accumulated in the peripheral region as shown in the Figure 3.2 by shaded region. So the region under observation (Figure 3.2, 'Area under observation') is the powder surface adjacent to the mixer wall. Generally the HSM can

not be operated with the lid open. For getting a sharp image of the granular bed the camera has to be taken near to it and into the mixer. So for most of the experiments, the mixer system has to be overridden to be operated with the lid open and the chopper off. The HSC was kept tilted at an angle of about 20° to the horizontal focused onto the granular bed as shown in Figure 3.2. The HSC was either held up with a steel-frame attached to the HSM or set up on an aluminium stand. The steel-frame was purpose built and served to fix the camera position at a particular position so as to neglect the error in image orientation when separate experimental results are to be compared. The camera inclination was checked with a spirit level.

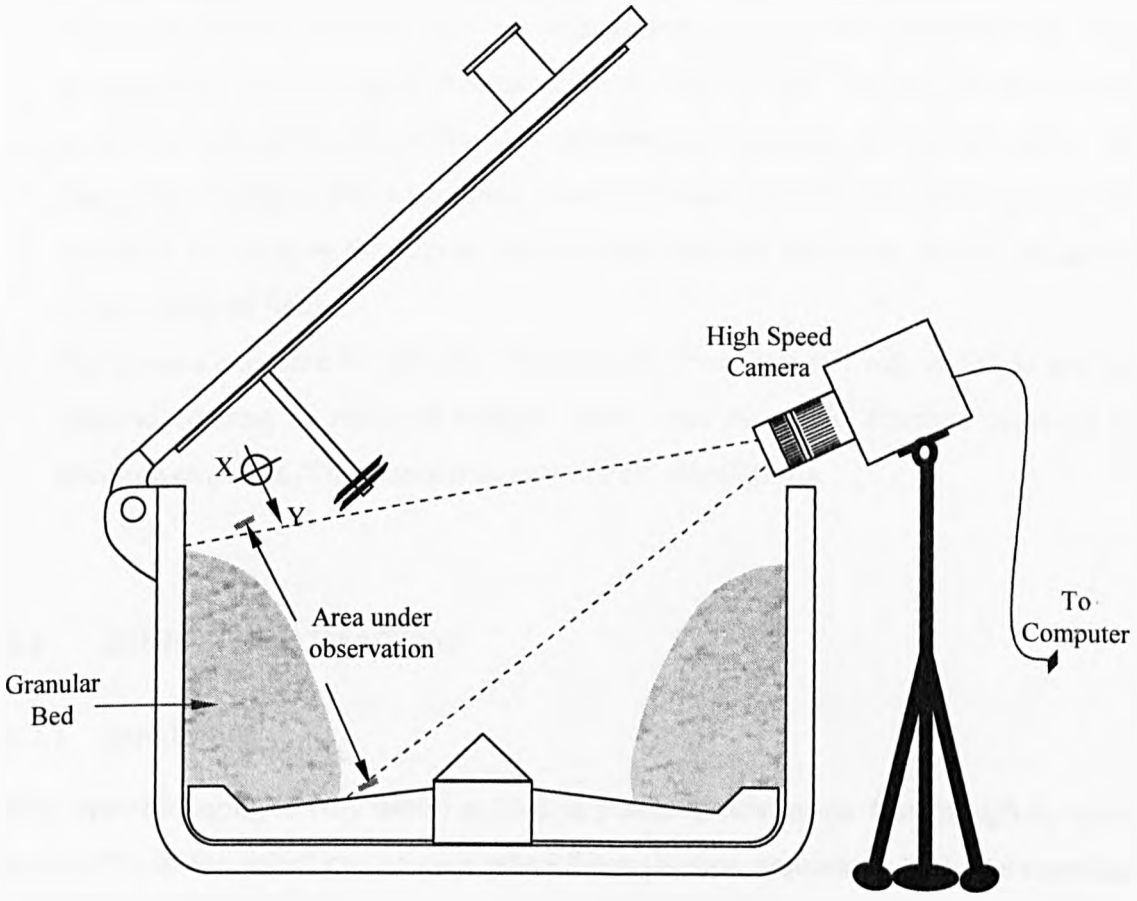

Figure 3.2: High speed camera setup with the high shear mixer. The positive x-direction is perpendicular to the plane of the image and points outwards. The positive y-direction is downwards at the area of observation or surface. Y-component of velocity approaches vertical component only at high impeller speeds.

3.1.3 Operating conditions

The operating conditions were selected on a case to case basis. The conditions mentioned below were common to all experiments unless expressed otherwise:

- The mixer load was kept constant at 2800 g. This fill ratio was found to be suitable for operating the mixer with the mixer lid open. The granules rarely came out of the mixer for impeller speeds up to 500 rpm.
- The camera angle to focus on the granular bed was changed in the range of 15 to 30° to get a good focus of the powder surface and to adjust to the changing profile of the granular bed with respect to the changing conditions. The angle was kept constant when the results of more than one experiment were to be compared. An exact perpendicular positioning of the camera to the bed surface was not always possible as the bed curvature was difficult to comprehend with the 2D camera and it was constantly changing due to running impeller blades underneath. Although the bed remained in focus as the digital camera used had the ability to resolve images to certain depth of field.
- The camera exposure to light (by changing the lens aperture) was varied to get best possible contrast in recorded images. There was no single absolute criterion for selecting exposure. The contrast improves PIV calculations.

3.2 HIGH SPEED IMAGING

3.2.1 Introduction

High speed imaging is very useful to look at processes that occur fast enough to be not perceptible to the naked eye or even when the resolution required is high. As described earlier in section 2.2.2, high speed camera (HSC) is characterized by their ability of recording images at speed generally above 50 Hz. Even higher speeds come at a cost of reduction in image size or resolution maintaining a balance between the speed and resolution is necessary to achieve the required purpose. The high speed cameras used during this research were borrowed from EPSRC - Engineering Instrument Pool (EPSRC-EIP, 2006). As the make and type of cameras borrowed from EPSRC depended on the availability of the high speed cameras, their functioning and operating procedure varied to a certain degree.

3.2.2 Image resolution

Image resolution is decided by the number of pixels in an image. A pixel is a picture element of an image that has single brightness value. A group of such different brightness pixels produces pattern in an image. Normally a pixel is a square element and an image can be expressed as the number of pixels in two dimensions of a plane. For example an image of resolution 1200×1000 pixels will have 1200 horizontal pixels and 1000 vertical pixels resulting in an image resolution of 1.2 mega pixels. The higher the resolution of an image the more detailed reproduction it will give of the original object. As the aim of the experiments was to understand the mean as well as the random motion, the images were recorded so as to optimize the balance between highest resolution available on a camera with the optimum image framing rate and capturing the entire height of the powder/granular bed.

3.2.3 Image framing rate

Image framing rate is the number of images that a video camera can record per second. It can be measured in frames per second (fps) or Hertz (Hz). The most suitable framing rate for the experiments was found to be 1000 Hz or the nearest value possible according to the settings available on a particular camera. It was also noticed that the image resolution was uncompromised at this framing rate.

3.2.4 Exposure time

Exposure time is the amount of time the camera image sensor is exposed to the light. In a HSC, this is achieved by switching the sensor on and off for the required time. So if the exposure time is 0.001 sec, the sensor will receive light for a period of 0.001 sec to create an impression of a single image. The exposure time setting has to be decided based on the amount of incident light available. The amount of incident light on the sensor can also be varied with the aperture setting within certain limits. For the experiments, the exposure time was set to be half the time between two consecutive frames. So for a framing rate of 1000 Hz, the time between to frames would be 0.001 sec and the exposure time would be set as 0.0005 sec. This setting was found optimum for capturing reasonably bright images with the type of illumination available during the experiments.

3.3 PARTICLE IMAGE VELOCIMETRY

3.3.1 Introduction

Particle image velocimetry (PIV) has been extensively applied to understand fluid flows (Adrian, 2005). The fluid is seeded with tracer particles that are assumed to follow the flow without disturbing it. The movement of these tracers is followed in space and time. The research in industry and universities has been mostly done with 2-D orientation with the 3-D version gaining popularity with emerging improvements (Adrian, 2005). In fluid flow, tracer particles are illuminated with a thin sheet of LASER. A sequence of images of these illuminated tracer particles are captured with a CCD camera to be then processed through PIV software to tabulate flow fields. In dense granular flows however, a LASER sheet may not be used as the large number of granules would block the light penetrating and coming out of the bulk. So the problem reduces to calculation of surface velocities restricted to 2-D flow if PIV is to be used for dense granular flows. Also in case of dense granular flows, the images recorded are more of a speckle nature rather than images with individual particles far from each other. In PIV a sequence of images is directly recorded with a digital camera. Two successive images are analysed computationally through a PIV algorithm based on either Cross-correlation (section 3.3.2.1) or MQD (section 3.3.3.1) to find the velocity field. The images are divided into small square areas known as 'interrogation window/area' over which correlation or MQD algorithm is applied. The corresponding interrogation areas from the two images are interrogated to calculate the average spatial shift of each interrogation window.

3.3.2 VidPIV® software

VidPIV® software correlates the consecutive images to give velocity vectors across the field of the image. The software splits up the vector calculation process into nodes, each meant to serve a different purpose. The nodes of particular interest in this study are:

- Timing: This node is to control and edit the timing information associated with the images.
- Annotations: Includes image mappings to convert image co-ordinates and displacement to real world units such as meters and inches. It also includes exclusions, lines, points and graphical annotations that allow masking off and identifying regions such as flow boundaries.

- Image: To import images into the project. This can be in pairs as well as single images.
- Derivations: Consists of data processing operations such as cross-correlation, vector filters such as global and local, etc.

The image mappings such as linear and photographic (non-linear) mappings are used to calibrate the distances on the image. The linear scale can be specified by plotting at least 3 reference points in the image field whereas the photographic mapping calculates distances from an image of dots (at least 20), equally spaced according to some reference unit (1cm for this case). Image node imports single image in 'Importation Single' sub-node or a pair of images for cross-correlating in an 'Importation Dual' sub-node. For cross-correlation, a grid description is necessary on which the correlation processing is applied. The description of the grid includes interrogation grid spacing, interrogation area dimensions and the units for definition of the grid spacing. The interrogation window size for correlation could be varied in the range of 16 by 16 to 128 by 128 pixels and a point to point separation can be specified in the range 8 to 128 pixels. The point to point separation was generally set equal to the interrogation size, so that the interrogation areas overlap each other half way. This is an optimum setting for better correlation results. The largest measurable displacement is 0.25 of the interrogation diameter. At an impeller speed of 300 rpm, a framing rate of 750 to 1500 fps gives reasonable movement of the granule bed. The images are annotated to exclude the effect of the blank corners and the regions of no-granules that would have caused zero velocity vectors.

3.3.2.1 Cross-correlation

The interrogation areas from consecutive images are cross-correlated, pixel by pixel in the PIV software. The correlation produces a signal peak, to calculate the common particle displacement. This is repeated for each interrogation area over the consecutive image frames to produce an array of displacement vectors. The distances computed from a reference image are used to calculate velocity vectors in the software. The cross-correlation algorithm for PIV is the method used to estimate velocity vectors in VidPIV®. The formula for two-dimensional cross-correlation of images f_1 and f_2 can be written as in Eq 3.1(Mori et al., 2003).

$$Cor(\Delta X,\Delta Y)=\frac{\sum_{i=1}^{N}\sum_{j=1}^{N}\left[f_1(X_i,Y_j)-\overline{f_1}\right]\left[f_2(X_i+\Delta X,Y_j+\Delta Y)-\overline{f_2}\right]}{\sqrt{\sum_{i=1}^{N}\sum_{j=1}^{N}\left[f_1(X_i,Y_j)-\overline{f_1}\right]^2}\sqrt{\sum_{i=1}^{N}\sum_{j=1}^{N}\left[f_2(X_i+\Delta X,Y_j+\Delta Y)-\overline{f_2}\right]^2}} \tag{3.1}$$

where f_1 and f_2 are the small (interrogation) windows from each image in the image pair, N is the window size and the over-bar denotes mean quantity. The location of the maximum value (peak) in *Cor* is used as the mean particle displacement of this small area. For detailed procedure of velocity field calculation the reader can refer to Willert et al. (1991).

3.3.3 PIV through MATLAB®

To have more flexibility on the PIV process, 'mpiv' toolbox available in MATLAB® was chosen for further analysis. By using this it was possible to set up the correlation parameters in the MATLAB® code rather than using some of the default setting in custom built PIV software as in VidPIV®. The 'mpiv' can use cross-correlation as well as MQD algorithm. The one used for the analysis here is MQD algorithm discussed below. According to Mori et al. (2003), the MQD algorithm work well for images containing no particles such as speckle images in which situation the correlation algorithm may not work.

3.3.3.1 Minimum quadric differences (MQD) algorithm

The MQD algorithm calculates the pixel value differences between the search windows f_1 and f_2. It is also referred to as 'Gray level difference accumulation'. MQD algorithm can be written as (Mori et al., 2003):

$$Cor(\Delta X,\Delta Y)=\sum_{i=1}^{N}\sum_{j=1}^{N}\left|f_1(X_i,Y_j)-f_2(X_i+\Delta X,Y_j+\Delta Y)\right| \tag{3.2}$$

The location of the minimum value in *Cor* is used as the particle displacement. In the 'mpiv' program the calculated displacement is retained as 'valid' only if the ratio of the values of the highest peak to the second highest peak exceeds a preset threshold value, and the ratio of the values of the highest peak to the R.M.S. (Root Mean Square) noise also exceeds a preset threshold value.

'Mpiv' makes use of 'Recursive super-resolution PIV' to increase accuracy and resolution of the results. It first begins with larger interrogation window iterating to smaller window and at the same time shifts the f_2 in second image according to the displacement from the previous calculation. It also achieves sub-pixel accuracy by a three-point curve fitting technique to calculate the real peak of the correlated results. The Gaussian function is used for the fitting in MQD algorithms and is as follows (Mori et al., 2003):

$$P_{sub} = i - \frac{1}{2}\frac{\ln Cor_{i+1} - \ln Cor_{i-1}}{\ln Cor_{i+1} - 2\ln Cor_i + \ln Cor_{i-1}} \tag{3.3}$$

3.3.3.2 Accuracy of 'mpiv'

Mori et al. (2003) used the PIV standard images taken from VSJ-PIV (case 1 in PIV Standard Project) distributed by the Visualization Society of Japan (http://www.vsj.or.jp/) to test the accuracy of mpiv. They summarised the dependence of the R.M.S. error on different algorithms chosen in mpiv, and different window sizes used in the process as in Figure 3.3.

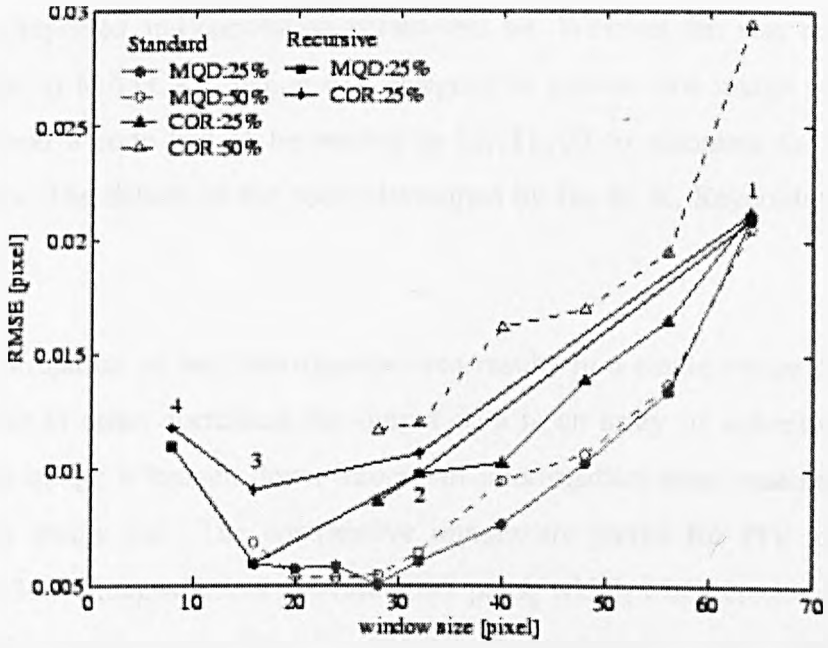

Figure 3.3: Dependence of R.M.S. error on different algorithms and window sizes (Mori et al., 2003). MQD: minimum quadric differences; COR: cross-correlation. The percentage values show the extent of overlapping of adjacent interrogation windows.

In the experiments in chapters 5 and 6, the recursive MQD algorithm at 50% overlap between adjacent interrogation areas was used. The RMS error for these settings is not mentioned in Figure 3.3. However it can be inferred from the figure that this value can be in the range 0.005 to 0.01 (in pixel). For interrogation window size of 16×16 it can be lower part of this range and that for 8×8 interrogation window size it can be in the upper range. This value of error will be compared with the values of granular temperature in corresponding sections in chapter 5 and 6.

3.4 VELOCITY ANALYSIS

The two aims of the velocity analysis were to understand the mean flow characteristics and the particle motion characteristics. Once the velocity data was gathered through PIV analysis, it was then processed independently for further analysis of mean motion and motion at a single interrogation area.

In most of the experiments, image recording was performed for 3 sec at a framing rate of 1000 to 1125 frames per second. So over a period of 3 sec around 3000 images are recorded. Processing of these many images was automated in VidPIV® once the image range to be imported and correlation parameters set. Whereas this was not the case in mpiv toolbox in MATLAB, which was designed to process one image pair at a time. For this reason a code had to be written in MATLAB to automate the PIV process through mpiv. The details of the code (developed by Dr. G. K. Reynolds) are given in Appendix A.

The cross-correlation of one interrogation area results in a single vector output. When an image pair is cross correlated the output data is an array of velocities across the image as the image is broken down into small interrogation areas creating one output file for each image pair. The consecutive images are paired for PIV analysis. This implies that 3000 images would provide 2999 pairs, which when cross-correlated will result in 2999 velocity array files. To simplify processing this much data codes were developed by Dr. G. K. Reynolds in 'C++' programming language, which are reproduced in Appendix B (1 and 2).

3.4.1 Bed velocity characterization

Bed velocity is characterized as an average of velocities across the entire height of the granular bed surface. Due to impact of each impeller blade the powder bed height fluctuates. This causes temporary blank spaces in the upper part of the images. This was taken into consideration and the upper boundary of the powder bed was masked off to offset the error due to blank areas. The extent of masking off was decided depending on individual experiments as the materials involved change the bumping behaviour of the powder bed. These adjustments were kept similar when two or more experiments needed to be compared with each other.

For understanding bed motion, a scalar average of array of velocities over an image was calculated and is termed as bed velocity. The variation in bed velocity was calculated by using 'C++' code as in Appendix B-1 (developed by Dr. G. K. Reynolds). The horizontal and vertical vector components of bed velocity are also analysed to understand the bumping and roping (Litster et al., 2002) behaviour.

The bed-velocity variation data obtained is a function of time for all sets of experiments. A typical plot of bed velocity (V) with time at 312 rpm impeller speed for granulation of PEG-4000 with Durcal-40 with the 3-blade impeller is shown in Figure 3.4. As the framing rate was 1000 frames per second, the time difference between two consecutive images is 1 ms and so the time difference between two consecutive bed-velocities is 1 ms. The highest temporal resolution achieved with the current procedure is the analysis at 1125 frame per second in chapter 4. At higher framing rates, compared to that used in this analysis, the granules do not make reasonable displacement to be able to calculate the velocities.

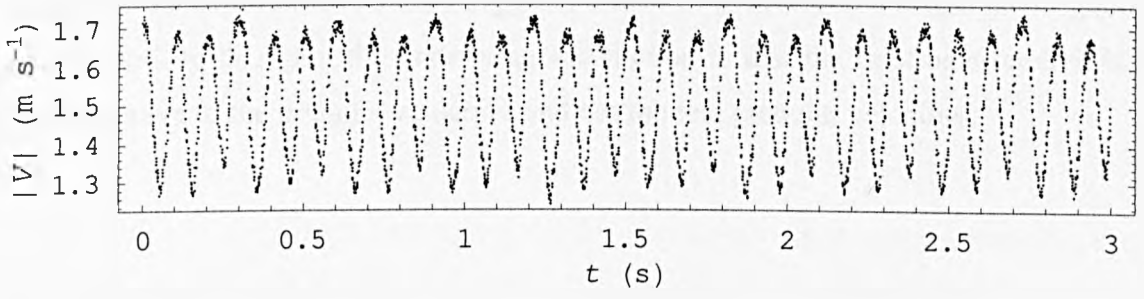

Figure 3.4: Bed velocity (V) variation with time at 206 rpm impeller speed for wet granulation of Durcal 40 with PEG-4000.

3.4.1.1 X-component of bed velocity (V_x)

The x-component is the horizontal motion in the direction perpendicular to the plane of the image in Figure 3.2. In the actual experimental mixer, this component exhibits the bed motion parallel to the impeller rotation and is representative of tangential component in cylindrical-polar coordinates.

3.4.1.2 Y-component of bed velocity (V_y)

The y-component of bed velocity is the vertical movement of the granular bed in the image reference. As the granular bed accumulates adjacent to the mixer wall under the influence of rotating impeller, the bed surface assumes a steep slope towards the mixer centre. As the camera is kept focused approximately perpendicular to this surface, the y-component of the bed velocity would be a resultant of axial and radial component of bed velocity in cylindrical-polar coordinate terms. As the bed at impeller speeds above 200 rpm assumes a steep slope for the surface, the V_y approaches the axial component.

3.4.2 Characterization of velocity at a single interrogation area

To understand the granular velocities, velocity at spatial resolution that approximates the size of a granule is necessary. Granules are the basis of binary aggregation that is used for population balance modelling in chapter 6. It was observed that, under the experimental conditions and the image resolutions used, the size of individual granule was in the range 2 to 6 pixels in the images recorded. The smallest possible interrogation area was 8 by 8 pixels size. This also means that the number of granules in a single interrogation area could range from 1 to 32 granules. The probability of 32 small granules in the same interrogation is very low due to the distribution of size ranges. A realistic estimate would suggest number of granules in a single interrogation area to be 2 to 8. Again the underlying assumption is that the interrogation area is a representative of the granular velocities and not the real granular velocities.

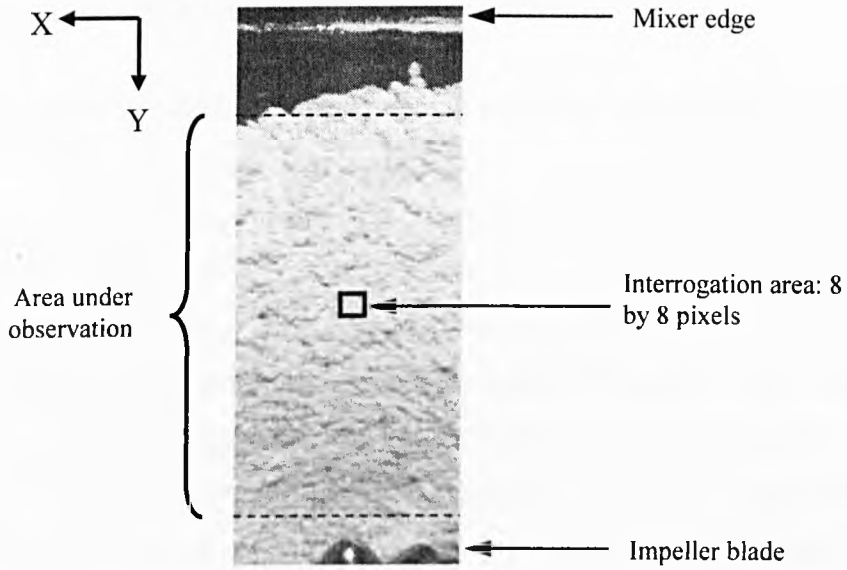

Figure 3.5: Typical image from high speed camera showing the powder/granular bed surface, some mixer features and the spatial location of the sampled velocity data. The orientation of the x and y coordinates is also illustrated.

To characterize the temporal variation of velocity at a single point, a suitable centrally located interrogation area was chosen (as in Figure 3.5). The velocity at this static point was then pulled out from the vector array file. This has to be done for all the array files for which another code in 'C++' was written as in Appendix B-2 (code developed by Dr. G. K. Reynolds). The raw velocity data could then be exported to 'Mathematica' and plotted as a function of time. An example of this plot is shown in Figure 3.6. This sample is taken from the same experiment as shown in Figure 3.4.

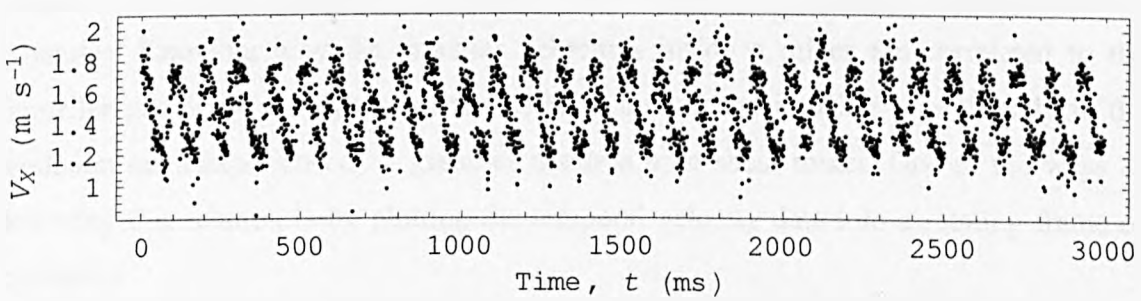

Figure 3.6: Sample x-velocity (V_x) variation at a centrally located interrogation area (size 8×8 pixel) in the field of view of the granular bed at 1 min time interval for wet granulation of Durcal 40 and PEG-4000.

3.5 FREQUENCY ANALYSIS OF VELOCITY

Frequency analysis is helpful in understanding repetition of particular signals, which in this case are bed velocity and its components. The frequency analysis clarifies the dependence of bed velocity on physical parameters such as instrumental design (e.g. impeller shape), material properties (e.g. binder viscosity). Fourier transform is the tool used in frequency analysis. It converts signal from time domain to the one in frequency domain known as Fourier spectrum. Fourier transform works on an infinite length continuous signal. For computing purposes, 'Discrete Fourier Transform' (DFT) is employed as computers can not handle continuous or infinitely long signals (Smith, 2003). The DFT produces a Fourier spectrum of a finite length sampled signal with values at a finite number of discrete frequencies.

The DFT can be directly executed in 'Mathematica' package with command *Fourier[list]*. This is incorporated in the 'Mathematica' code originally written by Prof. M. J. Hounslow as in Appendix C. This code was written for final analysis of raw velocity data obtained at the end of execution of C++ program in Appendix B-1 and B-2. It was later modified by the author for subsequent analysis and customized for individual experimental results.

3.6 VELOCITY PLOTS IN A ROTATING FRAME OF REFERENCE

The impeller in the high shear mixer imparts momentum to the granular bed. The impact forces and variation in velocity field dictate the collision behaviour of the granules. Knowing how the granular velocities inside a mixer are correlated to the impeller geometry and operation will help in linking the impeller type directly to the collision rates experienced by granules inside a high shear mixer. One of the ways of knowing this relation is by plotting the temporal velocity data into a rotating frame of reference.

From the knowledge of the frequency of bed velocity variation, the time resolved velocities can be plotted in a rotating frame of reference. In this the velocities were plotted as a function of position relative to an arbitrary fixed point on the impeller in degree angle (Figure 3.7). The angle of the impeller is measured from the initial

position of impeller starting at 0° to 360° at the end of a complete revolution of the impeller. Velocities during subsequent rotation of impeller will overlap already plotted velocity data. As the frequency of blade is thrice the frequency of impeller, one third of the blade frequency (f) (equivalent to impeller frequency) was used as a reference to plot velocities in the rotating frame of reference. The angular speed of rotation (ω) in radians can be written as:

$$\omega = 2\pi \frac{f}{3} \tag{3.4}$$

and the angle in degrees can be calculated as

$$\phi = \frac{180}{\pi} \omega t \tag{3.5}$$

where t is the time. The plot in rotating frame of reference would then show velocities against angle of impeller (ϕ) that varies from 0° to 360°. (See appendix C).

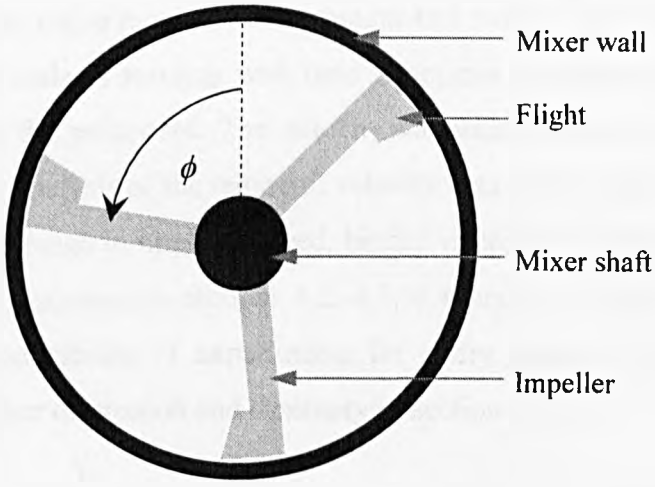

Figure 3.7: Top view of the high shear mixer illustrating the angle of impeller measured from the point of 'area under observation' (as in Figure 3.2) or the initial position of the impeller.

4

MOTION WITH A 3-BLADE IMPELLER

4.1 INTRODUCTION

This chapter deals with the granular-bed surface velocities and the flow pattern inside a 10 L Zanchetta high shear mixer equipped with the 3-blade impeller. The field of view was fixed across the entire height of the granular-bed surface effectively providing the mean motion. The scale of scrutiny with time is optimal considering the limitations of the equipment and the procedure. The velocity variation is correlated to the impeller position by Fourier analysis of the temporal velocity data. The temporal variation in the mean motion with change in impeller speed, binder viscosity, average granule size, and granulation time is discussed in sections 4.2, 4.3, 4.4, and 4.5 respectively. Section 4.6 discusses the reproducibility of experiments for a dry granule system. The chapter concludes with further discussion and summary in section 4.7.

4.2 EFFECT OF IMPELLER SPEED

4.2.1 Materials and procedure

A 2800 g batch of dry granules was prepared by granulating Durcal-40 and PEG-1500 at 60 °C beforehand and sieved into a size range of 0.4 to 2 mm after cooling. The granules are referred to as dry as the binder is in solid form at the room temperature. As the granules were dry, the impact with the impeller caused some granule breakage. Before reusing the batch, it was sieved to remove the undersize fragments produced during the experiment. The breakage from higher granule size range to lower granule

size range however remained unnoticed and can be assumed to be insignificant considering the short duration of these experiments. The dry-granule batch was fed into the mixer and the impeller was started. The chopper was kept off to prevent granule breakage and as only the response of the granular velocities to the impeller motion was sought. Once the impeller reached the specified rotational speed, high speed imaging of the bed surface was started and run for approximately 2.67 sec. The camera used for the experiments in sections 4.2, 4.3 and 4.4 was a Kodak HS 4540 high speed camera (EPSRC-EIP, 2006). This camera had a maximum image storing capacity of 3072 images in the temporary memory (RAM). The images had to be downloaded to a permanent memory (ROM) before the camera could be available for the next experiment. The resolution of the captured images was 256×256 pixels covering a physical area of 95×95 mm resulting in a spatial resolution of 0.37 mm/pixel. Above 1000 frames per second (fps) the framing rate of the camera could have been varied in the multiples of 1125 fps, i.e. 2250 and a maximum of 4500 (at full image resolution). In the trial experiments, it was noticed that the images captured at a resolution of 2250 (or higher) were not suitable for PIV calculations due to the low displacement of the granules in the image. So 1125 fps camera framing rate was used. Approximately 3000 images were captured. Consecutive image pairs making 2999 pairs were cross-correlated with VidPIV® software for velocity calculation. The bed velocity and its component were calculated as explained in section 3.4.1. Frequency analysis and rotational motion analysis was done as explained in sections 3.5 and 3.6 respectively.

4.2.2 Results

4.2.2.1 Comparing average bed velocities

Figure 4.1 shows the time averaged values of the bed velocity (V), the x-component of bed velocity (V_x) and the y-component of bed velocity (V_y) and its standard deviation at different impeller speeds. V and V_x tend to increase with increasing impeller speed except for a slight dip at 420 rpm. Both show similar behaviour with increasing impeller speed and difference in their magnitude is small. Average V_y doesn't vary much with increasing impeller speed but its standard deviation decreases slightly. This is due to the shortening of the period of time between consecutive impeller-blade passes responsible for the bumping nature (Litster et al., 2002) of the bed. The bed gets less time for a free fall under gravity and gets picked mid-way by the passing impeller blade underneath it

and exhibits a more roping than bumping behaviour. This could possibly also explain a slight dip in velocity at an impeller speed of 420 rpm. If an airborne ensemble of granules does not get caught straightaway by the passing impeller, then they retard more and result in reduction in average bed. As average V_y is positive, the resultant powder surface movement is downwards at all impeller speeds. The HSM is a closed system which means the powder has to stay inside it. With support of the findings using PEPT studies by Wellm (1997), it can be interpreted that the powder might be moving towards the mixer wall at the bottom of the mixer and rise upwards near the wall of the mixer to end up on the bed surface exhibiting a toroidal flow. The toroidal flow in HSM was first noticed by Holm et al. (1996) and was then confirmed by Wellm (1997) using PEPT technique. It should be noted that the positive and negative V_y need not be balanced for mass conservation as the motion near the wall is opposed to that seen on the bed surface.

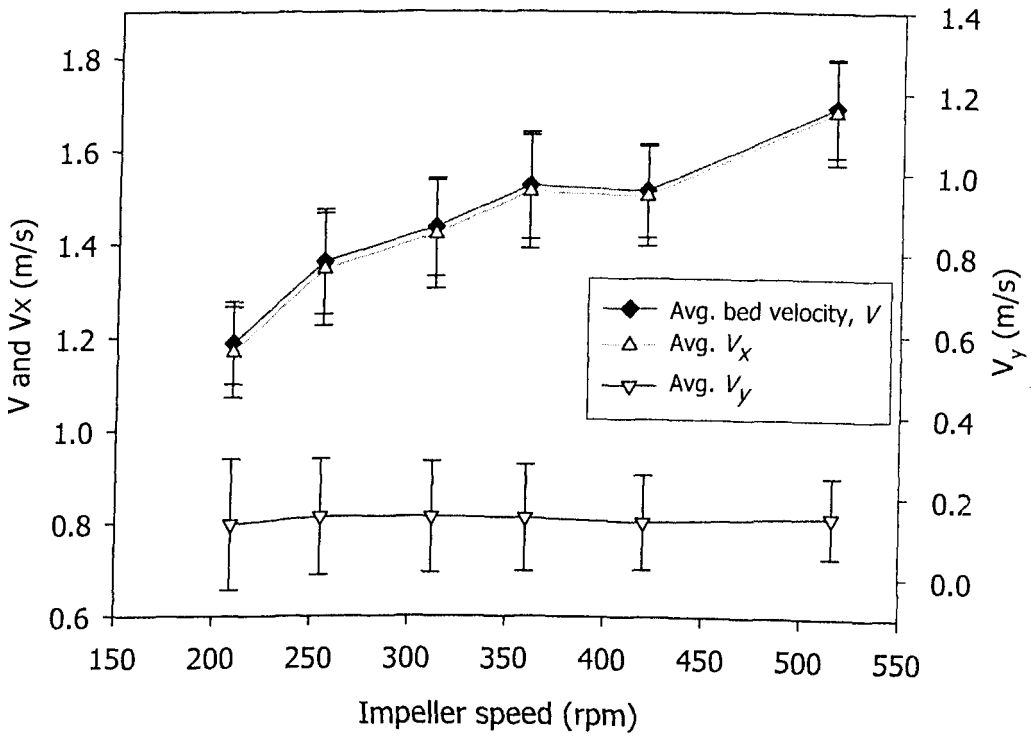

Figure 4.1: Time averaged velocity variation with impeller speed for 2800g dry granules batch made of PEG-1500 and Durcal-40. The standard deviations of the averaged velocities are also indicated.

Due to the loss in momentum transfer from the impeller to the granules and then from granule to granule, granules at the bottom of the mixer might be experiencing higher velocities. Higher particle velocities near the impeller blade approaching the values of

blade speed were reported in various PEPT studies (Stewart et al., 2001a). It should be noted that the impeller tip speed varied from 3.76 ms^{-1} (at 209 rpm) to 9.28 ms^{-1} (at 516 rpm). Whereas the bed speed at the surface was almost $1/3^{rd}$ to $1/5^{th}$ of the bed velocity magnitude, 1.2 to 1.7 ms^{-1}. Litster et al. (2002) found average velocities in the range of 0.2 to 1.0 ms^{-1} for dry lactose powder (d_{50}=64.8μm) for impeller speed range of 200 to 500 rpm in a 25 L HSM. Dry powder should be expected to exhibit low velocities (as can be interpreted from the discussion in section 4.4) and can be contrasted with the velocities here.

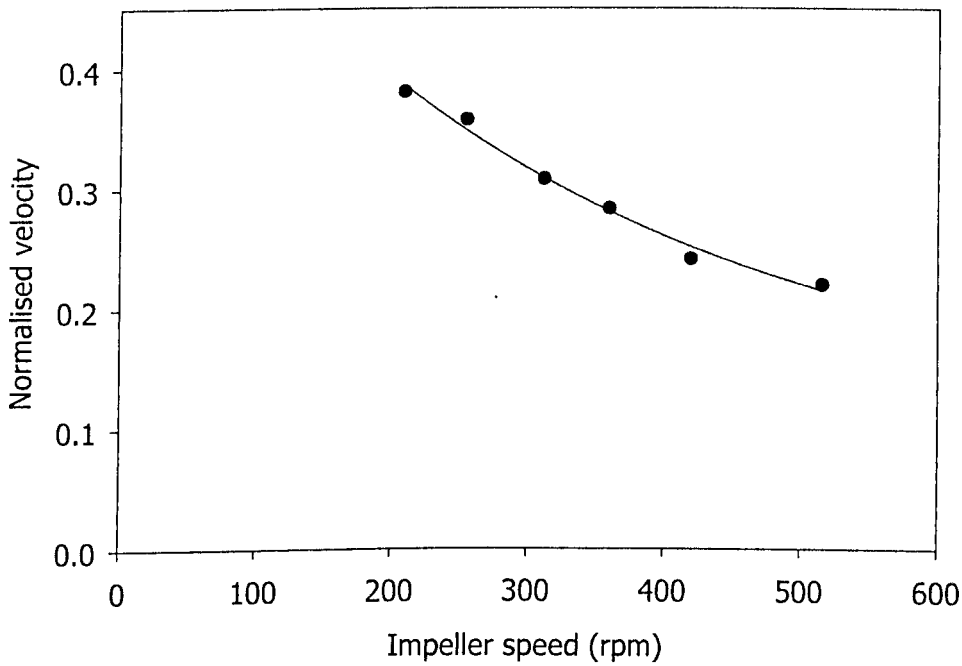

Figure 4.2: Normalised surface velocities (Bed velocity / Impeller tip speed) with different impeller speed for 2800g dry granules batch made of PEG-1500 and Durcal-40.

Although velocities tend to increase with the increase in impeller speed as shown in Figure 4.1, a different perspective of analysing it is shown by plotting normalised bed speed versus impeller speed. The normalised bed speed is the ratio of bed velocity (V) to impeller tip speed. Figure 4.2 shows that the normalised bed speed decreases from 0.38 to 0.22 with increasing impeller speed from 209 to 516 rpm. This means the increase in bed-velocity with impeller speed is not proportionate. In other words, a further increase in impeller speed leads to comparatively little increase in bed-velocity. Plank et al. (2003) found similar behaviour in a 25 l high shear mixer with normalised

velocity deceasing from 0.3 to 0.1 corresponding to a change in impeller tip speed from 2 to 11 ms^{-1} for a fill level of 0.26. This can be compared to the higher normalised velocity in Figure 4.2. At higher impeller speeds, the granular bed remains fluidised for more time with an expanded volume as compared to that at lower impeller speeds. The expanded bed results in higher distances between colliding granules. As the distances between granules increase the granules get freer path during which the loss in momentum will be higher resulting in lower normalised velocities.

4.2.2.2 Frequency analysis

The Fourier analysis of the bed-velocity data gives the primary frequency and harmonics of it. The power spectra (Figure 4.3) of the bed-velocity show the primary frequency to be near the impeller frequency. These graphs also show a peak near the blade frequency which is 3 times the impeller frequency due to the 3 blades and other smaller peaks in multiples of the primary frequency (corresponding to impeller frequency). With increasing impeller speed (Fig 4.3i to 4.3vi) there is a transition of the dominant frequency from the one corresponding to the blade frequency to the impeller frequency. At 209 rpm, the power spectrum exhibits peak at 3.38 Hz and 10.13 Hz corresponding to the impeller frequency 3.48 Hz and blade frequency 10.44 Hz respectively as in Figure 4.3(i) with both peaks having relatively similar magnitude. At 255 rpm, however, a major peak can be seen near to the blade frequency. This behaviour is maintained for 312 rpm but the peak intensity at blade frequency starts decreasing at 420 rpm and shows a very small peak for 516 rpm. The power spectrum for 516 rpm shows higher peak at 8.63 Hz corresponding to impeller frequency 8.6 Hz. The magnitude of this peak corresponding to the impeller frequency can be seen to be increasing from impeller speed 255 rpm through to 516 rpm. This behaviour can be explained only after an analysis of bed speed in a rotating frame of reference. The difference between the observed bed-velocity frequency and the impeller frequency recorded through the mixer instrumentation could be due to the *leakage* from one frequency to another while estimating the power spectrum (Press et al., 1986). If the actual frequency is between two frequency bins on the power spectrum then the *leakage* extends well beyond these two adjacent bins. This problem can be solved by *data windowing* (Press et al., 1986). Such an accuracy is however not required considering the aim of the analysis and so not discussed here.

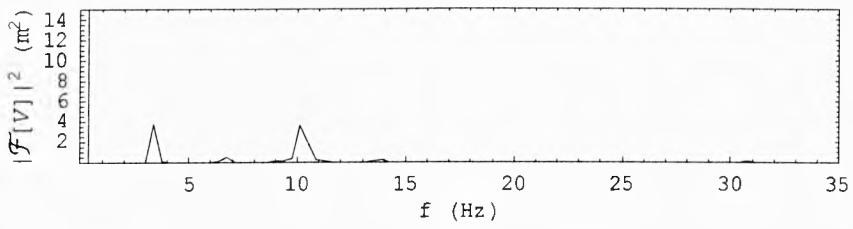

(i) 209 rpm (3.48 Hz)

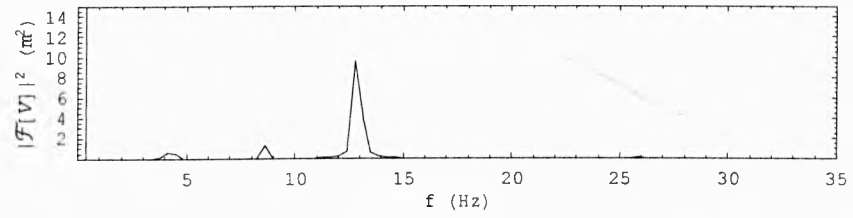

(ii) 255 rpm (4.25 Hz)

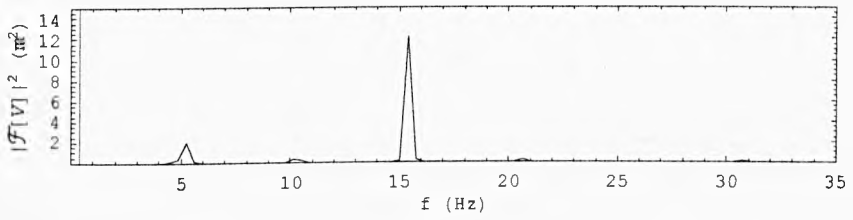

(iii) 312 rpm (5.2 Hz)

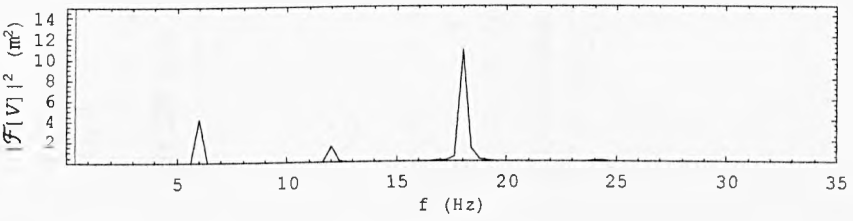

(iv) 360 rpm (6 Hz)

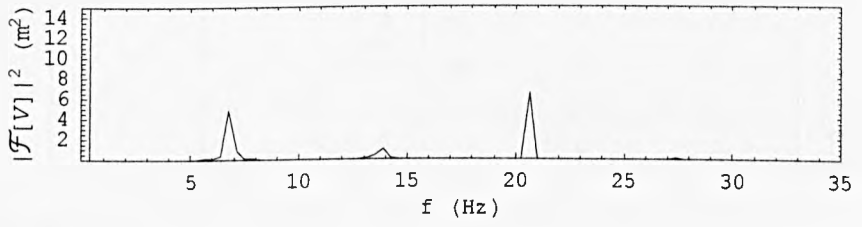

(v) 420 rpm (7 Hz)

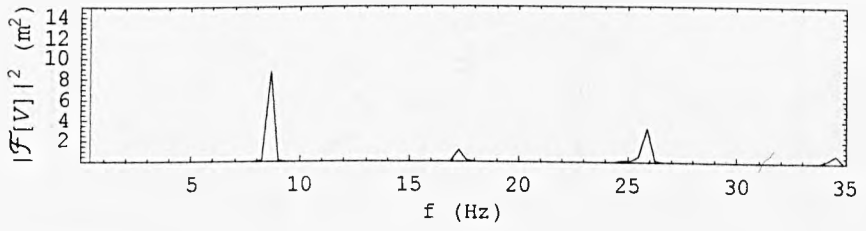

(vi) 516 rpm (8.6 Hz)

Figure 4.3: Power spectrum of bed velocity (V) at different impeller speeds for 2800g dry granules batch made of PEG-1500 and Durcal-40.

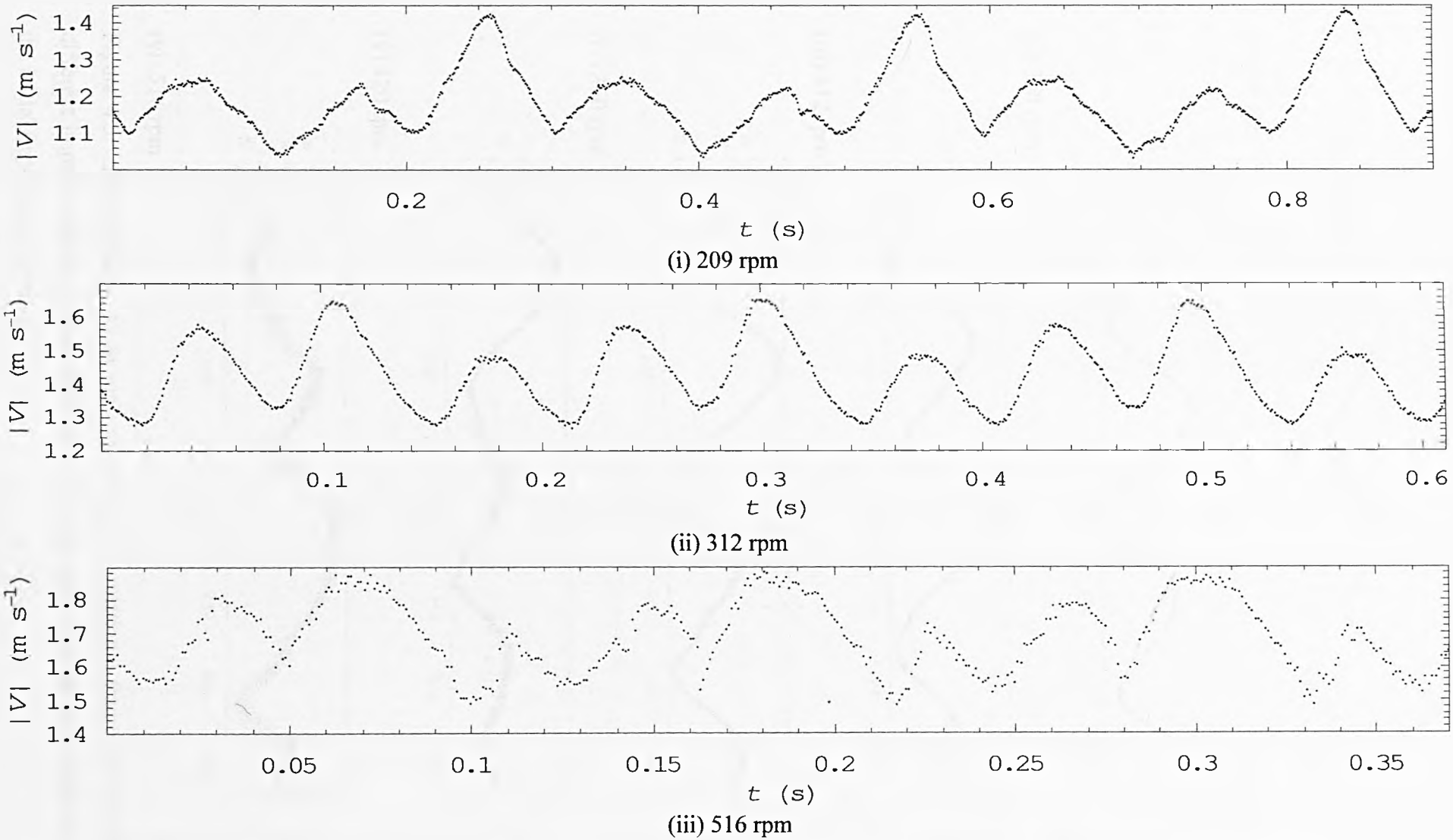

Figure 4.4: Time resolved bed velocity (V) at different impeller speeds for three impeller rotations for dry granules batch.

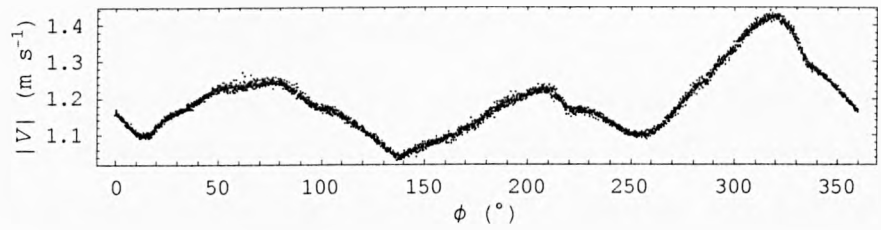

(i) 209 rpm

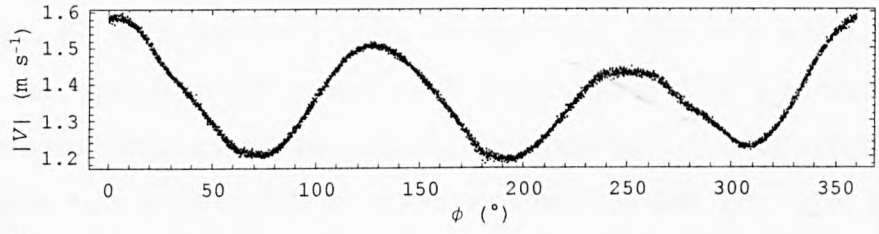

(ii) 255 rpm

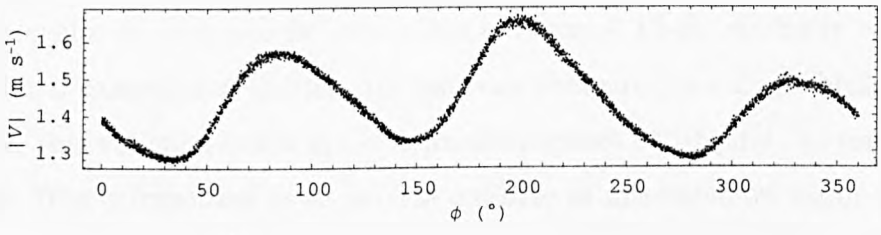

(iii) 312 rpm

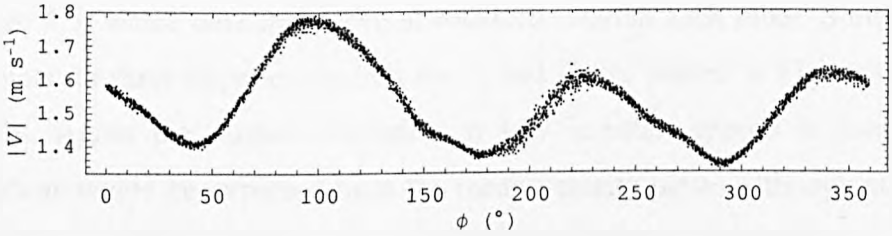

(iv) 360 rpm

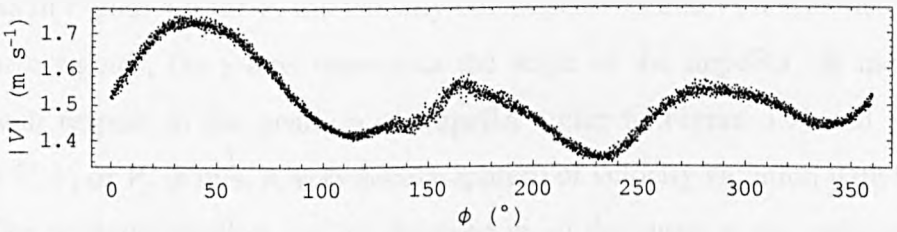

(v) 420 rpm

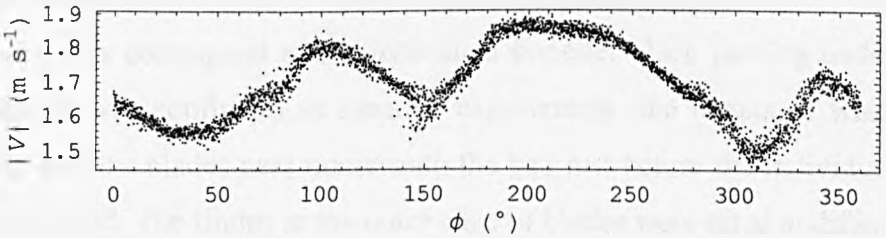

(vi) 516 rpm

Figure 4.5: Bed velocity (V) in ms^{-1} variation in a rotational frame of reference at different impeller speeds. Rotational frame of is the angle of impeller measured from the initial impeller position.

4.2.2.3 Analysis in a rotating frame of reference

The temporally resolved bed velocity is plotted in a rotating frame of reference in Figure 4.5 for different impeller speeds with reference of 1/3rd of the blade frequency from Figure 4.3 (as explained in section 3.6). To elucidate this, bed velocity as a function of time for the first three impeller rotations is shown in Figure 4.4. The velocity data for each impeller rotation overlaps each other in a rotating frame of reference. For example, at 209 rpm, a single rotation takes 0.287 s as seen in Figure 4.4(i), where first three peaks in bed velocity corresponding to the three impeller blades approximately take 0.28 to 0.29 s. It can also be seen that first three peaks take approximately 0.19 s at 312 rpm as in Figure 4.4(ii) and 0.12 s at 516 rpm as in Figure 4.4(iii). It can also be seen that the data points in Figure 4.4(i-iii) randomly vary around a mean value if examined at shorter time intervals compared to a single blade pass or a single peak. This variation is low at lower impeller speeds of 209 and 312 rpm and high at 516 rpm. This is important to be pointed out here as this variation within short time intervals (within blade passes) is not clear from the plots in rotating frame of reference as in Figure 4.5, where data from several rotations overlap each other. Similarly, time resolved plots for three impeller rotation for V_x and V_y are plotted in Figure 4.6 and 4.7 respectively. Again the random variation at low impeller speeds is low for both components as would be expected from the mean velocity plots. Although at 516 rpm, V_x exhibits more random variation as compared to V_y (Figure 4.6iii and 4.7iii). Similar to the plots in Figure 4.5 for V, the velocity components V_x and V_y are plotted in Figure 4.8. In these figures, the x-axis represents the angle of the impeller (ϕ) measured in degrees with respect to the position of impeller (refer to Figure 3.7) and the y-axis represents V, V_x or V_y in m/s. A very regular pattern of velocity variation with respect to the impeller or blade position can be observed in all the cases as the velocity profiles coincide for successive rotations. Three individual peaks can be seen in each of the plots. These peaks correspond to the individual impeller-blade passing underneath the granular bed. It was confirmed in separate experiments (the results of which are not shown here) that the blades pass underneath the bed just before the individual peaks in V or V_x are attained. The flights at the outer edge of blades were tilted at different angles in a sequence of 36°, 33° and 30° (clockwise) to the horizontal. Each of these flights imparted different momentum to the granular bed exhibiting different intensity peaks. Although the position of individual blades with respect to the periodic velocity variation was not noticed, it can be reasoned that the blade with the highest angle would provide a

higher momentum to the bed compared to low inclined blades. These plots are not normalised according to impeller position, but the peaks in velocity can be seen in the sequence corresponding to the blade angle sequence. However if it is assumed that the highest peak is due to the 36° flight-blade, the second highest magnitude peak does not always correspond to the 33° flight-blade.

In Figure 4.5(i), at an impeller speed of 209 rpm, the last peak being the highest peak would correspond to the 36° blade making the first peak correspond to the 33° and the second or middle peak to the 30° blade. The higher magnitude peaks can be correlated to the greater blade angle for impeller speeds 209 and 255. Assuming the 36° blade imparts the highest peak, the behaviour changes at 312 rpm in which case the 30° blade imparts the second highest magnitude peak whereas the 33° blade gives lowest magnitude peak. At medium impeller speeds of 360 and 420 rpm the 30° and 33° blades show similar magnitude peaks. At the higher impeller speed of 516 rpm the behaviour is similar to that at 312 rpm. The bed-velocity (V) shows some fluctuations even between consecutive blade passes at 209 rpm (Figure 4.5i) showing it to be as much repetitive in an impeller rotation as between blade passes. Due to this same magnitude peaks can be seen in the power spectrum in Figure 4.3(i). The velocity curves are rather smooth and the peaks are prominent at 255, 312 and 360 rpm (Figures 4.5ii to iv) with smooth variation between blade passes resulting in a higher peak in power spectra at blade frequency. But the fluctuations between blade passes again start to show up as impeller speed is increased through 360 to 516 rpm (Figures 4.5 iv to vi). This could be due to 'dynamic' mismatch between the ensemble of granules that get fluidised (then fall under the action of gravity) with the passage of the impeller blades resulting in fluctuations at very low impeller speed (209 rpm, Figure 4.5i) and at high impeller speeds (360 to 516 rpm, Figure 4.5iv to 4.5vi) as opposed to medium impeller speeds (255 and 312 rpm, Figure 4.5ii and 4.5iii). At 516 rpm the velocities are very scattered in rotating frame although conserving the repetitive nature.

4.2.2.4 Comparing V_x and V_y

The x-component of bed velocity (V_x) represents the horizontal motion of the bed in the direction of the impeller rotation and the V_y represent the vertical motion of the bed signifying the turnover and the surface renewal of the bed. The V_x (Figure 4.8) shows similar behaviour to that of the bed velocity (V) as in Figure 4.5 with slightly reduced

magnitude. The variation in V_y is compared side by side to the V_x in Figure 4.8. It can be observed that as V_x decreases in magnitude, V_y increases and vice-versa. The peaks in V_x are followed by the dips in V_y. Here the role of the flight angle reverses. The 36° flight-blade causes the lowest magnitude dip in V_y. This means that the higher flight angle causes the bed to move more horizontally than vertically. V_y achieves its highest value between the blade passes as that is the time when the bed relieves from the impact of the blade and falls freely under gravity. However the peaks in V_x do not match exactly with the dips in V_y and show a phase shift of approximately 20°. For example at 312 rpm (Figure 4.8iii), the highest peak of V_x is between (ϕ =) 190° to 205° at which point the V_y is just about to enter its lowest dip between (ϕ =) 210° and 225°. V_y shows very smooth nature at all impeller speeds with narrow scatter at low impeller speeds. V_y shows negative values between all three blade passes at 209 rpm. This negative magnitude V_y shows gradual shift towards positive side with increasing impeller speed. At 255 and 312 rpm it shows negative values twice during each impeller rotation. This reduces to once every impeller rotation at 360 rpm and higher impeller speeds with systematic reduction in magnitude of negative values. The convention for V_y is positive for downward motion. So, negative V_y values signify upward motion that can also be looked at as signature of bumping nature of bed or a momentary disturbance in regular motion. This is because at higher impeller speed the bed gets less time to recover from single blade pass and experiences more consistent impact induced by the fast moving impeller conserving the regular flow.

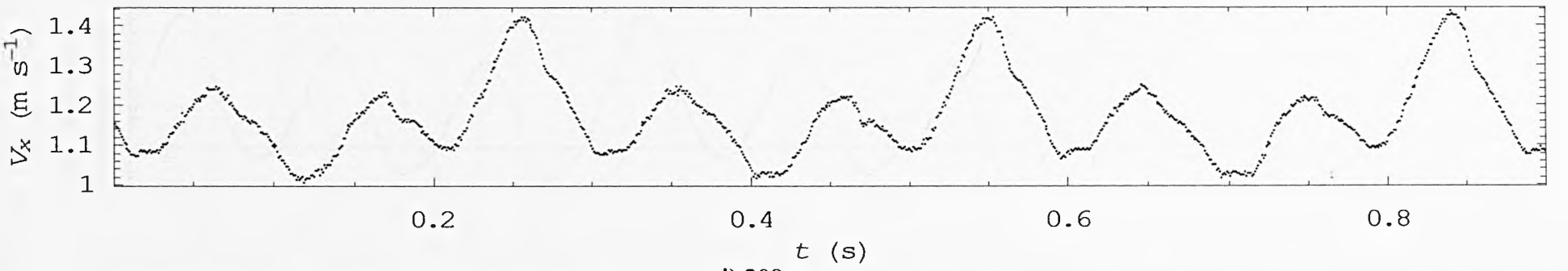

i) 209 rpm

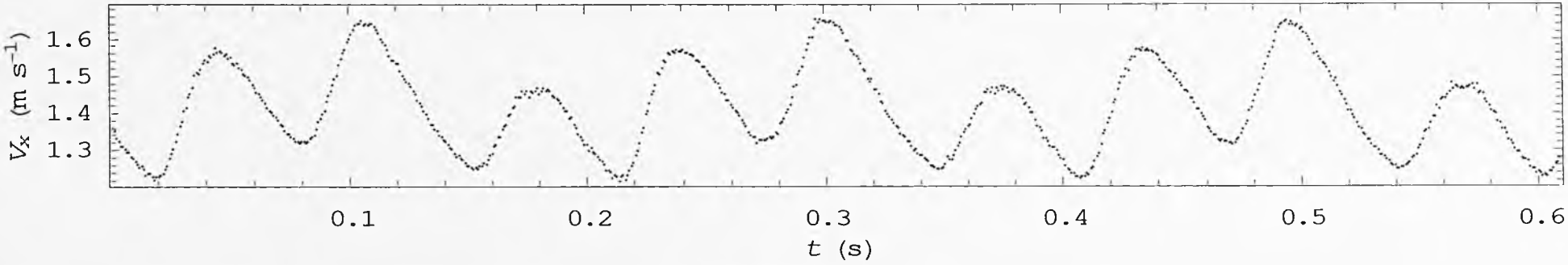

ii) 312 rpm

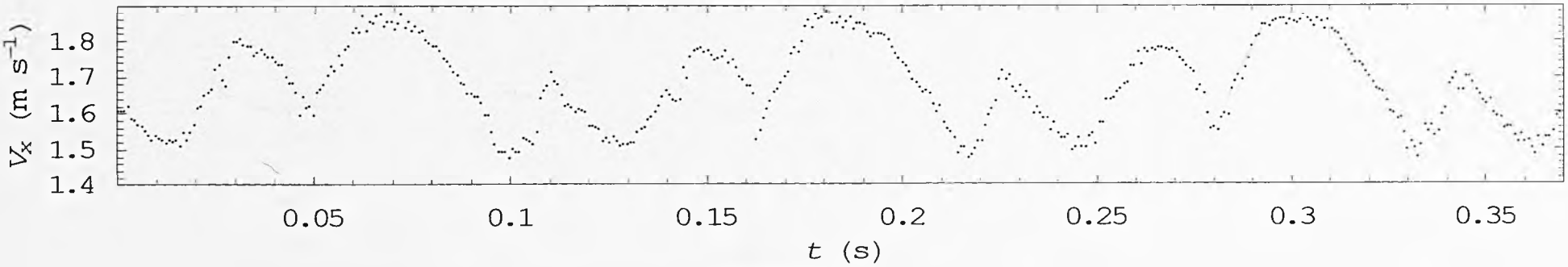

iii) 516 rpm

Figure 4.6: Time resolved V_x at different impeller speeds for three impeller rotations for dry granules batch.

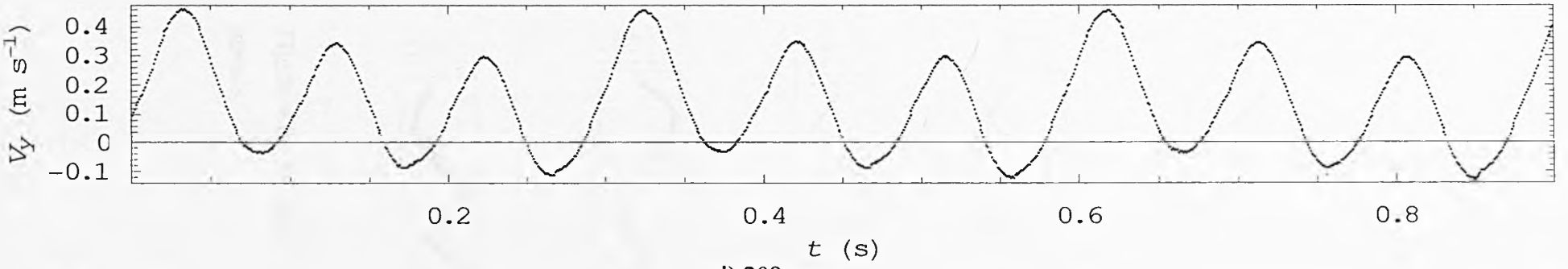

i) 209 rpm

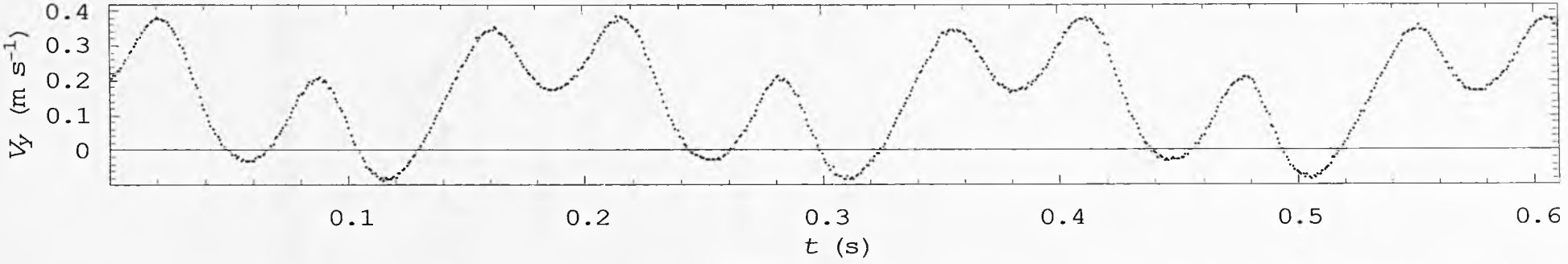

ii) 312 rpm

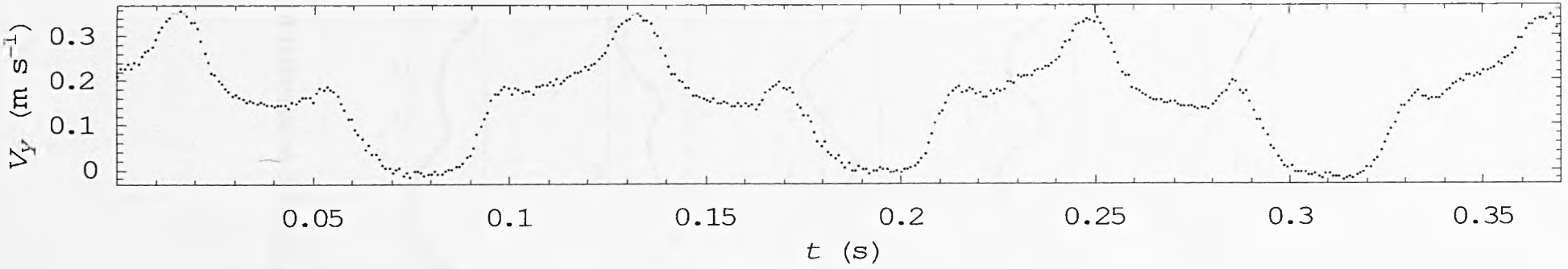

iii) 516 rpm

Figure 4.7: Time resolved V_y at different impeller speeds for three impeller rotations for dry granules batch.

V_x, *x*-component of bed-velocity

V_y, *y*-component of bed-velocity

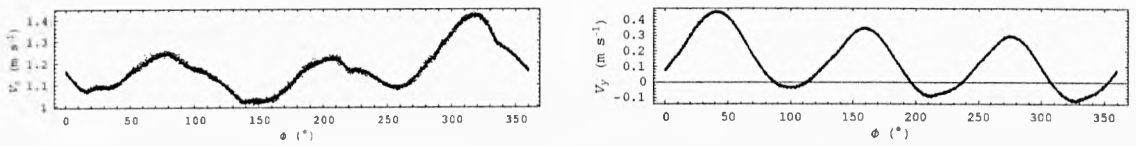

(i) 209 rpm

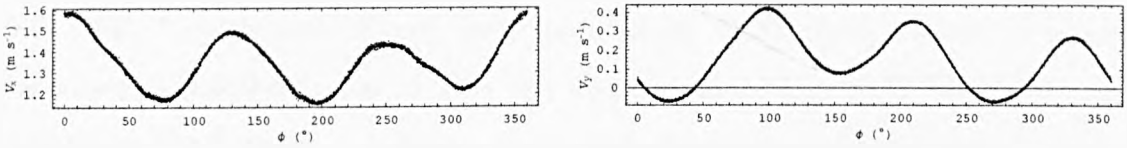

(ii) 255 rpm

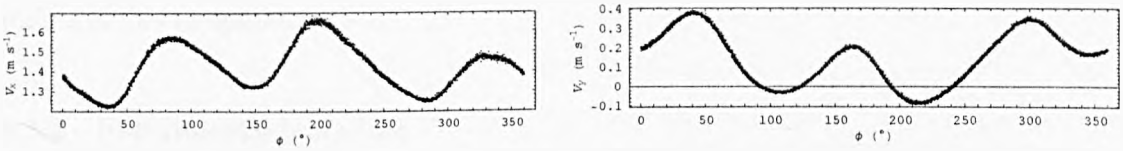

(iii) 312 rpm

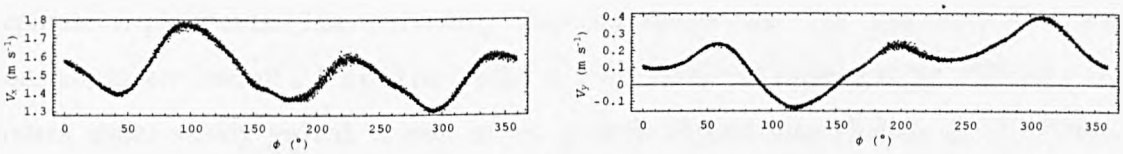

(iv) 360 rpm

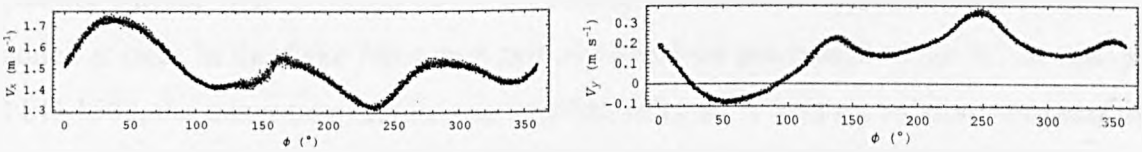

(v) 420 rpm

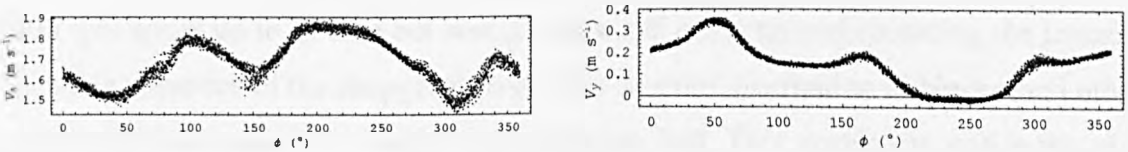

(vi) 516 rpm

Figure 4.8: V_x and V_y variation in a rotational frame of reference at different impeller speeds.

4.3 EFFECT OF BINDER VISCOSITY ON VELOCITY

4.3.1 Materials

The feed powder material used for these experiments was Durcal-40 (Calcium Carbonate) that had an *x50* size (by number) of approximately 24 μm. The binders included Glycerol, PEG-400 (Polyethylene Glycol, avg. molar mass 400 g/mol) and PEG-1500 (Polyethylene Glycol, avg. molar mass 1500 g/mol). Glycerol with a viscosity (η) of 890 mPa.s at 25 °C is very viscous compared to PEG-400 that has η = 93 mPa.s at 25 °C. These two binders are liquid at room temperature. For PEG-1500 the mixture temperature was 55 °C at the time of image capturing and it has viscosity of 95 mPa.s at this temperature.

4.3.2 Experimental procedure

Wet granulation experiments of different binders with Durcal-40 were carried out in separate experiments. The prevailing impeller speed was 312 rpm (5.2 Hz) with constant mixer load of 2.8 kg. The binder to solid ratio was chosen to be 13% w/w that comes under steady growth region in the growth regime map (Iveson et al., 1998a). Glycerol and PEG-400 binders were added by pouring through a funnel on the moving powder surface over a period of 30 s at room temperature. Whereas PEG-1500 was added at once in the flake form on a bed of Durcal-40 pre-heated to 55 °C. In case of PEG-1500, the mixer temperature was maintained at 60 °C and the mixture temperature was recorded to be approximately 55 °C at the time of capturing images. The images were recorded at 27 minute after the addition of binder. The chopper was kept on at 1400 rpm speed up to 27 min but was switched off at the time of recording the images. The main objective of the chopper is to provide an even distribution of binder (and other granulating components) throughout the granular bed. This enabled to notice the true effect of the binder viscosity to a certain extent on bed velocity irrespective of other parameters that influence it. The high speed camera system and the image analysis process were similar to as explained in section 4.2.1.

4.3.3 Results

4.3.3.1 Nature of velocity variation

The bed-velocity data is plotted as a function of time for Glycerol, PEG-400 and PEG-1500 in Figures 4.9 (i), (ii) and (iii) respectively. The consecutive bed-velocities are separated by 888 μs in time (inverse of the framing rate of 1125 fps) that suggests a high temporal resolution. The individual peaks in these graphs correspond to consecutive blade passes. Each time a blade passes underneath the granular bed, it imparts some momentum to the bed. Qualitative as well as quantitative differences can be observed between the velocity patterns for Glycerol (Figure 4.9i) and PEG-400 (Figure 4.9ii) and that for Glycerol and PEG-1500 (Figure 4.9iii). For Glycerol, the velocity fluctuations between consecutive blade passes are sluggish or slowly varying compared to PEG- 400 and PEG-1500 where the fluctuations are more prominent. The bed-velocities for Glycerol are in the range of 0.55–1 ms^{-1}, for PEG-400 it is in the range of 0.95–1.5ms^{-1} and for PEG-1500 it is in the range of 1–1.6ms^{-1}. All the data points in these three graphs can be split into *x*- and *y*- components. Averaging the bed velocity and its components (Table 4.1) reveal that Glycerol, which is almost 10 times more viscous than PEG-400 and PEG-1500 (at 55 °C), slowed down the granular bed by nearly 40% when compared to average bed-velocity for PEG-400 and PEG-1500. It is also interesting to note that the dry granules experiment in section 4.2 at same impeller speed (312 rpm) and mixer load (2800 g) has higher bed velocity. This is anticipated due to the viscous and elastic dissipation of energy during particle collisions as proposed by Ennis (1991). For granules with high viscosity binder the kinetic energy loss would be higher in a collision. So the momentum imparted by the impeller is lost until that energy passes on to the granules on the bed surface away from the impeller blades. Schaefer (1996) too mentioned that the granules made of high viscosity binder tend to be stickier than those with low viscosity binder. Fu et al. (2004b) showed that the granules made with higher viscosity binder tend to exhibit lower restitution coefficient in their impact test results. They also showed that granules made with high viscosity binder tend to exhibit higher contact area on a collision resulting in a higher dissipation of impact kinetic energy. Also as the viscosity of binder increases the amount of binder required for saturation in a granule decreases. So for 13% l/s ratio of these binders with dry powder, the probability of free Glycerol on the granule surface is higher compared to PEG-400 and PEG-1500. This would again contribute towards

slowing down the powder bed. This phenomenon of intertwined effects of liquid content and binder viscosity has also been pointed out by Iveson et al. (2003) in their review paper. A possible correction to the current experiment would be to simultaneously measure the granule sizes that will provide some indication of combined effect of viscosity and granule size. It should also be noted that the viscosity of PEG-1500 is susceptible to variation due to temperature variation likely due to the elevated operating temperature of the process. It was also pointed out by Iveson et al. (2003) that the binder temperature changes affect its wetting and spreading characteristics, which will again contribute to velocity changes. This could also be one of the reasons of slightly higher velocities with PEG-1500 than with PEG-400 even though their viscosities are approximately similar under prevailing operating conditions. However the experiment with PEG-1500 elaborates and supports the argument for the major effect binder viscosity has on the bed velocity.

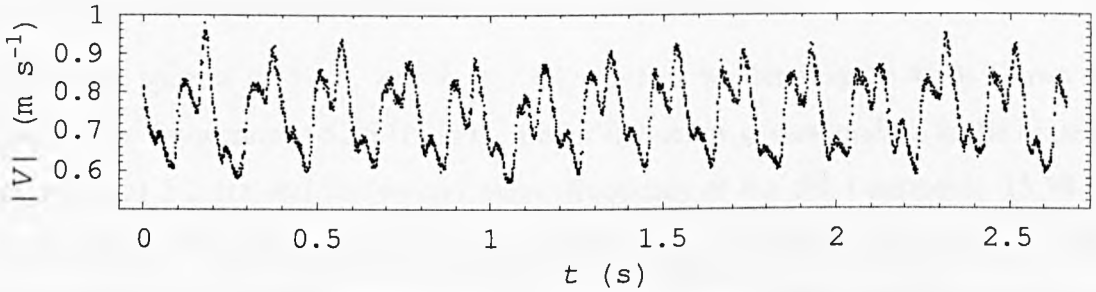

(i) Glycerol as granulating binder.

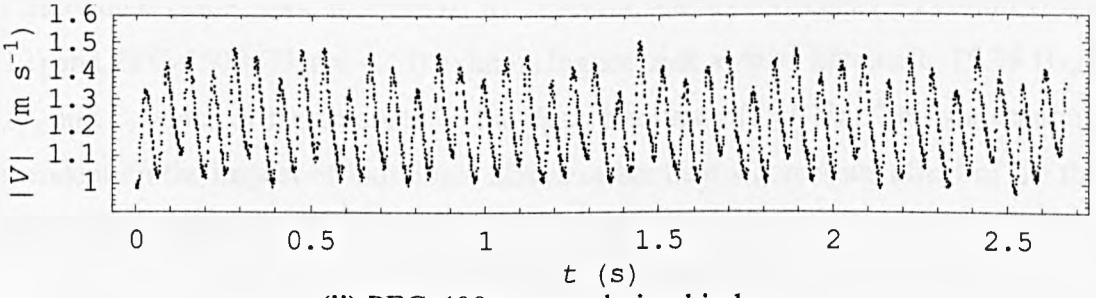

(ii) PEG-400 as granulating binder.

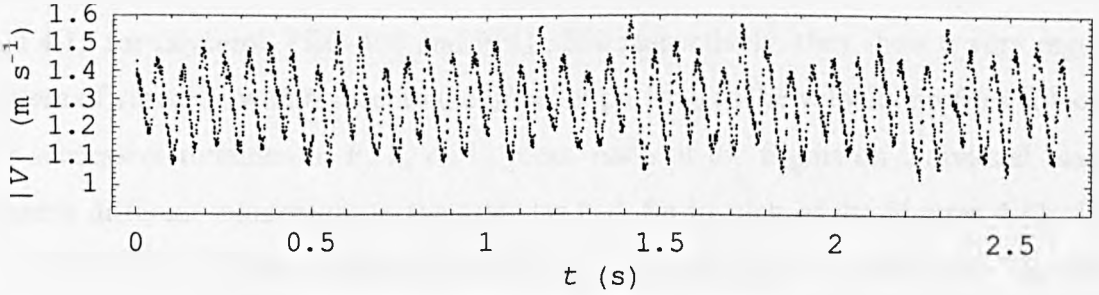

(iii) PEG-1500 as granulating binder.

Figure 4.9: Bed velocity (V) variation with time for wet granulation of three different binders at 27 min granulation time.

Table 4.1: Granular-bed velocity variation for wet granulation of Durcal-40 with three different binders.

Granulating Materials	Velocity / Component	Average (m/s)	Std. Dev. (σ)
Glycerol (η = 890 mPa.s at 25°C) & Durcal-40	V	0.75	0.09
	V_x	0.71	0.12
	V_y	0.19	0.09
PEG-400 (η = 93 mPa.s at 25°C) & Durcal-40	V	1.21	0.13
	V_x	1.20	0.14
	V_y	0.12	0.12
PEG-1500 (η = 95 mPa.s at 55°C) & Durcal-40	V	1.29	0.12
	V_x	1.28	0.13
	V_y	0.11	0.11

4.3.3.2 Interpreting the frequency analysis and rotational motion

The power spectra of V, V_x and V_y for Glycerol as binder (Figure 4.10) shows the fundamental frequency at 5.25 Hz as the major frequency corresponding to the impeller frequency of 5.2 Hz and the second major frequency at the third harmonic 15.38 Hz near the blade frequency of 15.6 Hz (3 × 5.2 Hz). This exhibits the occurrence of bed motion that is more characteristic of or dependent on a complete impeller rotation than an individual blade pass. In contrast to Glycerol, the low viscosity PEG-400 (Figure 4.12) and PEG-1500 (Figure 4.14) exhibits higher peak at third harmonic, 15.39 Hz, for V, V_x and V_y which is characteristic to the blade frequency (15.6 Hz). This shows motion dependent on the impact of individual blades rather than a combined effect of the three blades as an impeller.

When the velocities are plotted in a rotational frame of reference as in Figure 4.11, 4.13 and 4.15 for Glycerol, PEG-400 and PEG-1500 respectively, they show a very regular pattern of variation with respect to the impeller position as the velocity profiles coincide for successive rotations in V, V_x or V_y plots. Each of the flights on individual blades imparts different momentum to the granular bed. So in each of the Figures 4.11, 4.13 and 4.15, three different peaks with different intensity can be observed. The bed-velocity (V) magnitude and behaviour is mostly influenced by V_x and both show similar behaviour and relatively similar magnitudes.

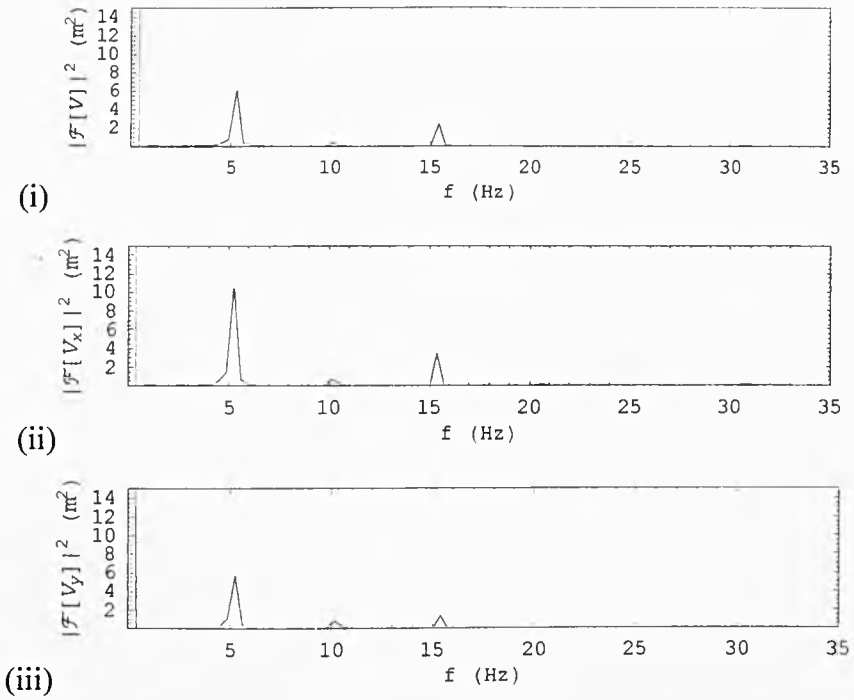

Figure 4.10: Power Spectra for wet granulation of Glycerol & Durcal 40 (at room temperature) for (i) V, average bed-velocity; (ii) V_x, x-component of bed-velocity; (iii) V_y, y-component of bed-velocity.

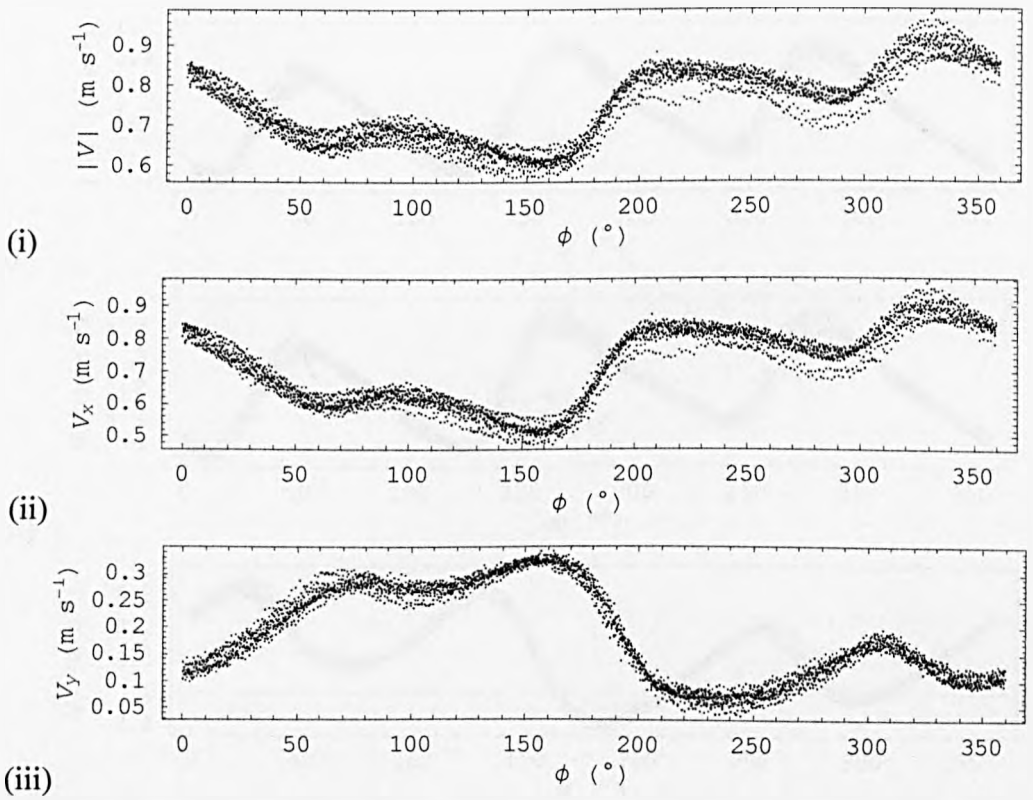

Figure 4.11: Velocity variation in rotational frame for wet granulation of Glycerol & Durcal 40 (at room temperature) for (i) V, average bed-velocity; (ii) V_x, x-component of bed-velocity; (iii) V_y, y-component of bed-velocity.

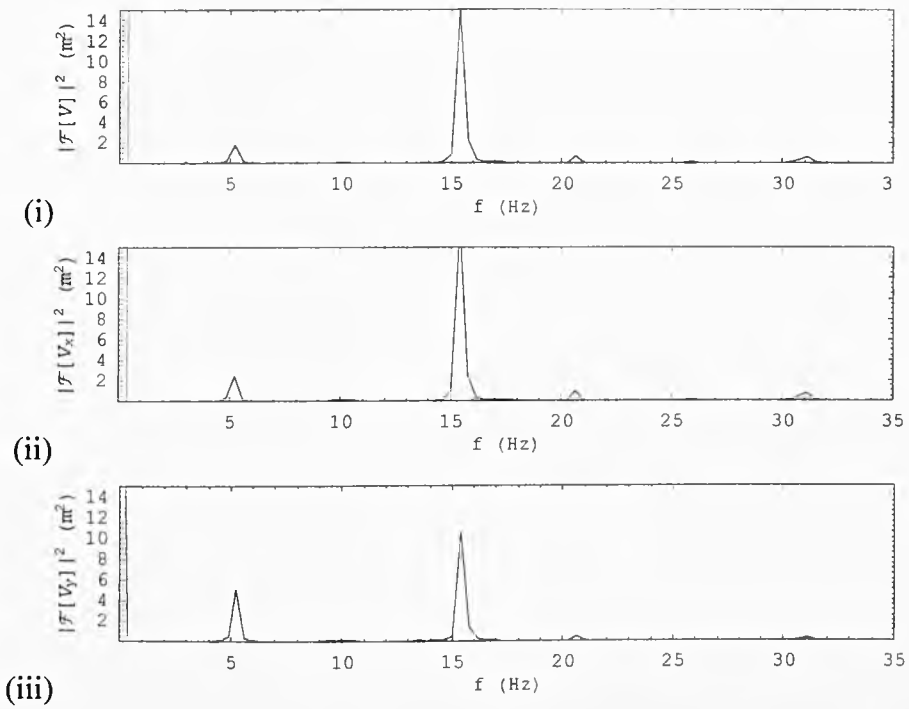

Figure 4.12: Power Spectra for wet granulation of PEG-400 & Durcal 40 (at room temperature) for (i) V, average bed-velocity; (ii) V_x, x-component of bed-velocity; (iii) V_y, y-component of bed-velocity.

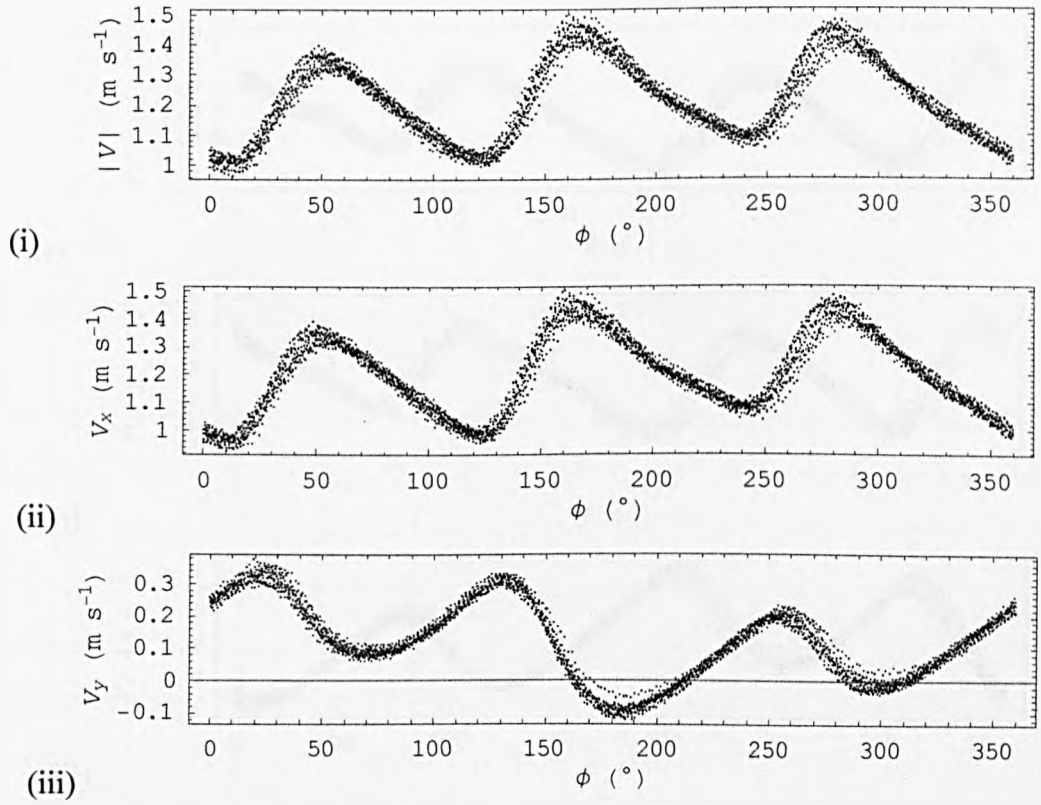

Figure 4.13: Velocity variation in rotational frame for wet granulation of PEG-400 & Durcal 40 (at room temperature) for (i) V, average bed-velocity; (ii) V_x, x-component of bed-velocity; (iii) V_y, y-component of bed-velocity.

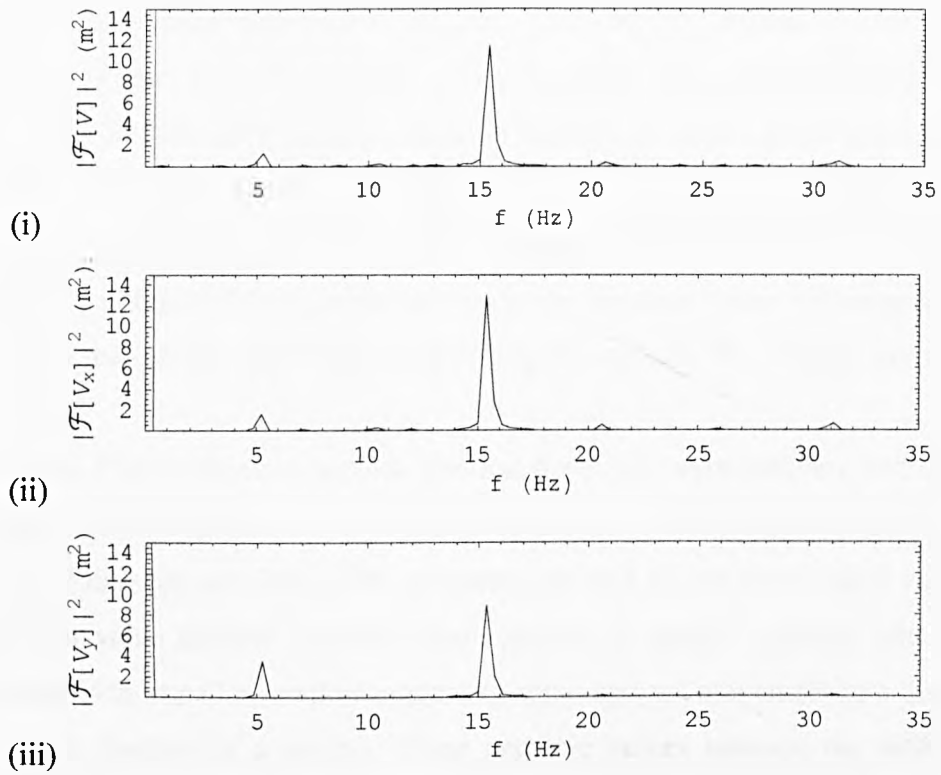

Figure 4.14: Power Spectra for wet granulation of PEG-1500 & Durcal 40 (at 55 °C temperature) for (i) V, average bed-velocity; (ii) V_x, x-component of bed-velocity; (iii) V_y, y-component of bed-velocity.

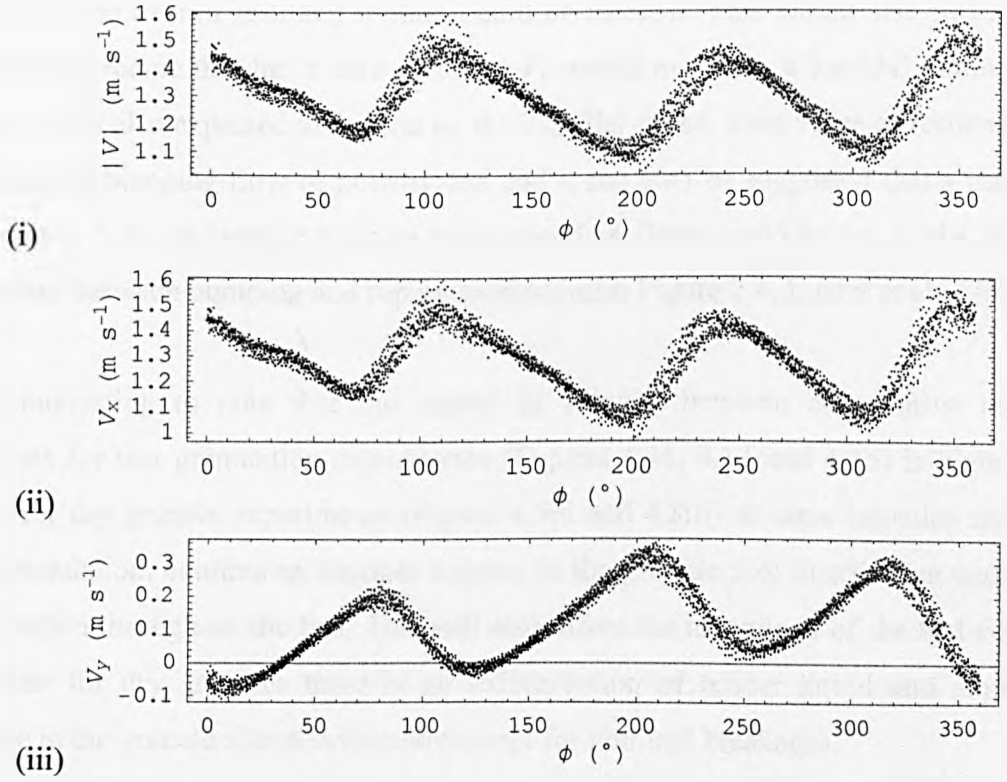

Figure 4.15: Velocity variation in rotational frame for wet granulation of PEG-1500 & Durcal 40 (at 55 °C temperature) for (i) V, average bed-velocity; (ii) V_x, x-component of bed-velocity; (iii) V_y, y-component of bed-velocity.

For Glycerol, individual peaks in bed-velocity show repetitive nature corresponding to blade passes (Figure 4.11) but are not very prominent. This could be due to the high viscosity (visco-elastic property, i.e. viscous as well as elastic property) of glycerol. Due to this not so prominent nature of velocity peaks, a higher peak in power spectra near impeller frequency in Figure 4.10 can be seen exhibiting the effect of the impeller as a whole. V_y in Figure 4.11(iii) does not show any negative values meaning no upward movement at the surface and therefore exhibiting a consistent flow in one direction.

PEG-400 and PEG-1500 show almost identical behaviour with similar curves for V, V_x and V_y plots as in Figure 4.13 and 4.15 respectively. The individual peaks in bed-velocity for PEG-400 and PEG-1500 are prominent and do not show much variation in its maximum value attained between blade passes. V_y attains negative values almost twice during each impeller rotation suggesting some upward movement or a disturbance in flow for a fraction of a second. These negative values increase the difference in average V_y for PEG-400 and PEG-1500 to that of glycerol (Table 4.1). When V_y approaches zero magnitude the bed is in a more translational than a supposedly toroidal motion. However the resultant V_y average, which is positive (as in Table 1) makes it clear that the overall resultant motion could be toroidal. This would also mean that a granulating recipe that has a zero resultant V_y would not show a toroidal motion. This behaviour is also expected to depend on the impeller speed. Zero value of resultant V_y is probable in bumping flow of powder bed and it can also be suggested that a transition from zero V_y to an average positive value (toroidal flow) could be set as the dividing boundary between bumping and roping motion (refer Figure 2.4, Litster et al., 2002).

It is interesting to note that the scatter in velocity between consecutive impeller rotations for wet granulation experiments (Figures 4.11, 4.13 and 4.15) is higher than those for dry granule experiments (Figure 4.5iii and 4.8iii) at same impeller speed. In wet granulation, continuous changes happen in the granule size distribution and liquid distribution throughout the bed. This will also affect the magnitude of the bed velocity. Whereas for dry granules there is no redistribution of binder liquid and almost no change in the granule size distribution (except for nominal breakage).

4.4 EFFECT OF GRANULE SIZE ON VELOCITY

4.4.1 Materials

For this experiment the granules used were dry, made of Durcal-40 and PEG-1500. Several batches of these materials were processed through HSM at 60°C. For each batch 13% l/s ratio was maintained. The granules were then sieved into three size ranges as: 0.71 to 1 mm, 1 to 1.4 mm and 1.4 to 2 mm to produce batches of 2800g material each. So the mixer load for each of the experiments was kept constant at 2800g.

4.4.2 Experimental procedure

Three separate experiments were carried out, one for each granule size range. The camera position was undisturbed and maintained for all the three experiments. The mixer was fed with the batch of granules and run only for a short duration of time. The image recording was started as soon as the impeller steadied on the designated speed of 312 rpm. 3000 images were recorded each time and later processed through VidPIV® to calculate bed velocity and its components. The high speed camera system and the image analysis process were similar to that explained in section 4.2.1.

4.4.3 Results

For bed velocity (V), temporal variation is discussed here but for V_x and V_y only average values are discussed. Generally the average bed velocity and the average V_x tend to increase with an increase in average granule size as in Figure 4.16. For consecutive size ranges the bed velocities showed a marginal increase of around 3%. This increase, although marginal, shows that the granule size indeed has an effect on the bed velocity. The picture becomes clearer and interesting when the temporally averaged bed velocity is split up in to x and y components. Contrary to the increase in V_x, V_y tends to decrease with an increase in the granule size range. Decrease in V_y would mean a slow moving toroid. As these experiments are aimed at providing a general overview of the dependence of the bed velocity on the average granule size, only the average velocities over 3 second are plotted and the standard deviation bars are not included in Figure 4.16. As the mixer load was constant, the number of granules in lower size range would be higher. So for every momentum transfer from the impeller to the granular bed there would be higher number of collisions between the particles in the lower size range

batch. This also means that the momentum loss would be quicker for the lower size range batch as compared to the higher size range batch. Another supporting reason for this could be the trajectory segregation (Williams, 1990) between different size granules. Due to higher air drag on small granules, they will travel less distance than bigger granules before coming to rest or before colliding with the granules coming from behind. It should however also be noted that the granular flow studied here is a dense flow and the air drag may not be that high. It should be emphasised here that as the granules are dry the intertwined effect of binder viscosity and binder content on these experiments can be assumed negligible.

The positive V_y is the downward motion according to the sign convention mentioned. In case of smaller granules the energy dissipation is quicker. Due to this the horizontal motion (V_x) imparted by the impeller to the granule mass is taken over quickly by the gravity force resulting in lower average V_x and higher average V_y. Whereas for bigger granules the energy dissipation is comparatively slow and the horizontal (V_x) is maintained by the impact of each passing impeller blade.

The variation of bed velocity (V) for size ranges 0.71 to 1 mm, 1 to 1.4 mm and 1.4 to 2 mm are shown in a rotating frame of reference in Figures 4.17 (i), (ii) and (iii) respectively. In general the graphs clearly show the momentum imparted by each blade pass as individual peaks in bed velocity. These graphs were adjusted so that the position of highest peak corresponding to the 36° flight-blade can be seen first in the sequence of blade passes. With an increase in granule size the entire bed velocity variation range shifts by certain magnitude. The behaviour is almost identical for the three size ranges of granules. The second and third highest peak in magnitude show same value except for size range 0.71-1 mm, where the 30° flight-blade shows the second highest peak and not the 33° flight-blade.

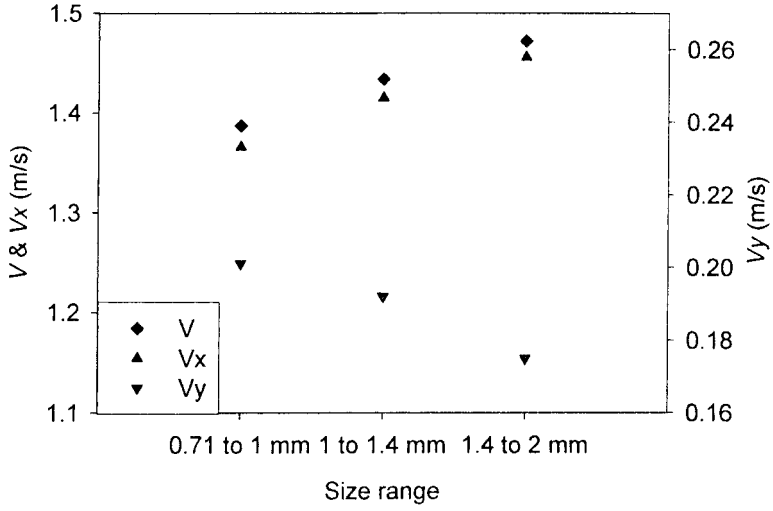

Figure 4.16: Velocity variation as a function of granule size range.

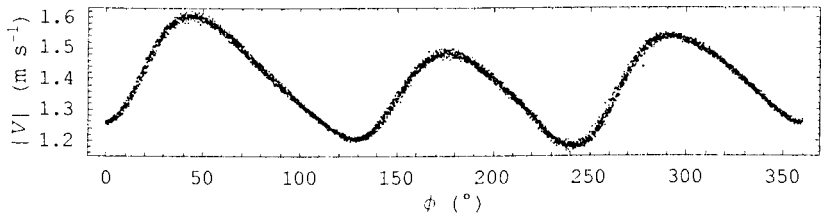

(i) Size range 0.71 to 1 mm.

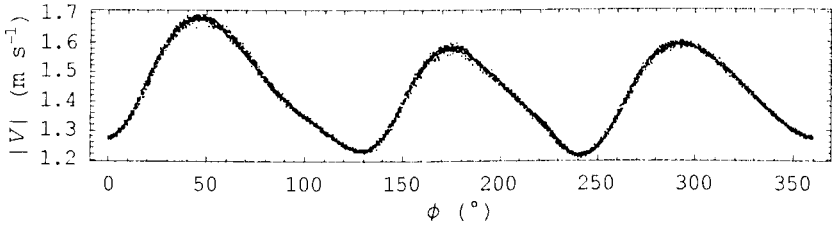

(ii) Size range 1 to 1.4 mm.

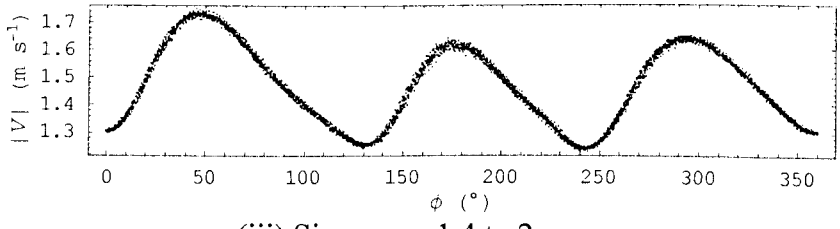

(iii) Size range 1.4 to 2 mm.

Figure 4.17: Bed velocity (V) for dry granules of Durcal-40 & PEG-1500 at three different size ranges.

4.5 VELOCITY VARIATION WITH GRANULATION TIME

These experiments were carried out to look at how the bed velocities vary as a function of granulation time. Dry powder bed could form a powder cloud inside the mixer while the impeller is rotating. So the first bed velocity observation was performed at 1 min after the binder addition was complete. The data used in this section is the bed velocity information and mean granule sizes only. This same experiment was further analysed for velocity at a single interrogation area and granule size distribution for use in chapter 6.

4.5.1 Materials

Materials used for granulation were calcium carbonate (Durcal 40, Omya, France) that had an $x50$ size of approximately 24 μm and polyethylene glycol 4000 (PEG-4000) in flake form. PEG-4000 has average molar mass of 4000 g mol^{-1}. The binder was added to make an overall liquid to solid ratio of 13%.

4.5.2 Experimental procedure

PEG-4000 has a melting range of 53-58 °C. The Durcal 40 was preheated in the mixer to a temperature of 65 °C. The binder was heated separately to 70 °C, and poured onto the powder bed over a period of 2.5 min. The granulation time used for the sampling was started at the end of the binder addition. The temperature of the granulating mixture during granulation was approximately 64 °C. The mixer was operated with an impeller speed of 200 rpm and a chopper speed of 1400 rpm using a 2.8 kg load of material. The high speed camera was set-up as previously described in section 3.1 and was kept ready in order to capture images of the powder bed surface. The mixer lid was opened during image capture at times of 1, 4, 7, 10, 15 and 20 min after binder addition. As the chopper was attached to the mixer lid, it first had to be switched off before opening the mixer lid for a short duration of approximately 30 s at each sampling time. Images were captured for a period of approximately 3 s, which is equivalent to approximately 10 revolutions of the impeller. Granule samples were also collected during the mentioned sampling times to deduce granule size distribution used for further analysis in chapter 6.

The high speed camera used in this experiment was a Photron – DVR (EPSRC-EIP, 2006). The framing rate was set at 1000 fps, which was nearest possible setting to the framing rate of 1125 fps set in previous experiments in sections 4.2 to 4.4. This camera had a resolution of 640×240 pixels at 1000 fps. As the 640 pixels were horizontal count, the camera was tilted by 90° so as to capture the entire granular-bed height. 3000 images were captured over a period of 3 s at every 1, 4, 7, 10, 15 and 20 min time intervals after binder addition. Although this camera had the capacity to record images over a period of 30 min, it was unnecessary to record beyond 3 second at 1000 fps considering the aim of the experiments and the optimal data obtained in 3 s. The images in this experiment were processed in 'mpiv' with recursive MQD algorithm. Bed velocity and its components were calculated as mentioned in section 3.4.1.

4.5.3 Results

It is expected that the velocity variation during a real granulation experiment is a combination of free binder presence and average granule size. The impeller speed and the mixer fill ratio would remain constant during this experiment and so the effect of these two parameters won't count. As in Figure 4.18, the bed velocity at 1 min was found to be the lowest. At 1 min, the binder addition was just complete and one would expect presence of free binder that is not engulfed in a granule. This free viscous binder would have slowed the bed. Also at this early stage the amount of fine powder would be high resulting in faster dissipation of momentum energy imparted by the impeller to the bed. The granule size just after the initial nucleation stage is the highest at 4 and 7 minute (Figure 4.19) and this result in high bed velocities. At this 4 min stage the binder would have been engulfed into the granules with scant free binder. There is a possibility of free powder particles on the granule surface at 4 min. At 7 min granulation time in the compaction stage the trapped air inside the granules makes way to the binder that would also start to make the surface moist. This result in slightly lower velocity at 7 min compared to that at 4 min even though the mean particle size is the highest at 7 min. After this stage the binder gets evenly distributed into the granules and the mean granule size change also steadies (except at 20 min) resulting in more uniform bed velocities as can be seen after 7 min of granulation time. Although the velocities remain steady after 7 min, an increase in granule size was witnessed from 15 min to 20 min. This could be the period of induction growth (refer section 1.2.2), where surface liquid make the granules stick resulting in higher mean. The velocities at 15 and 20 min are

however steady due to a combination effect of surface binder and granule size. As was previously seen, higher V_x magnitude was accompanied by lower V_y magnitude; the same is true in this case.

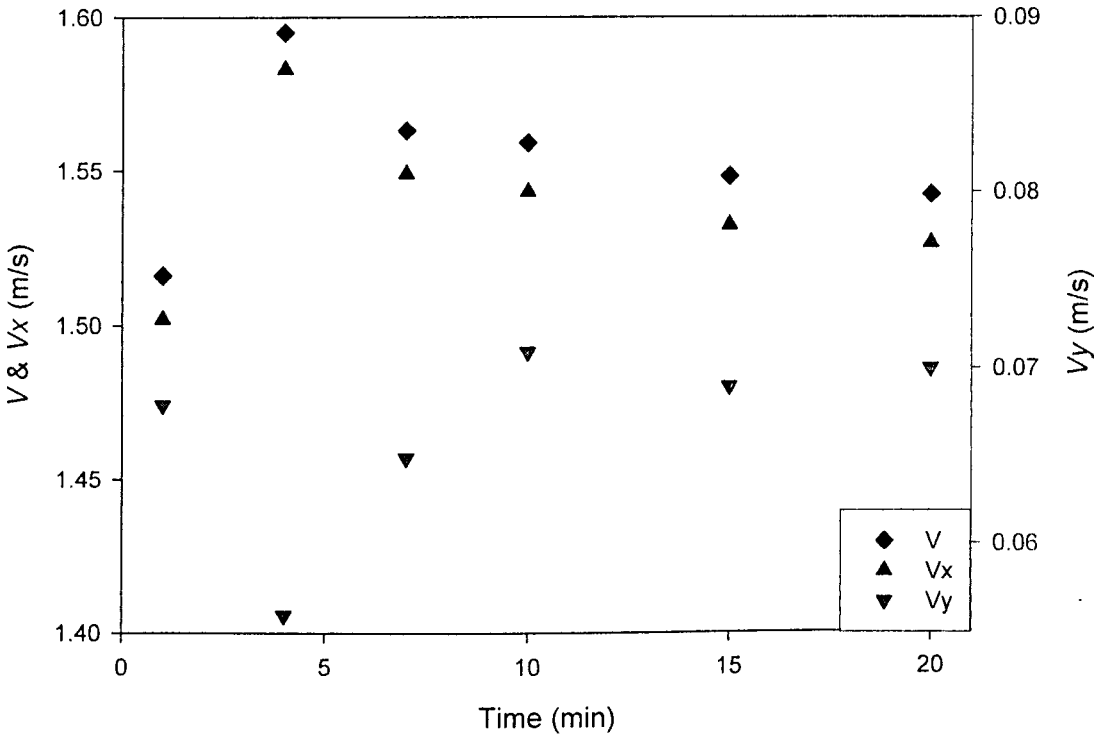

Fig 4.18: *V, Vx & Vy* as a function of time in wet granulation experiment for Durcal-40 and PEG-4000.

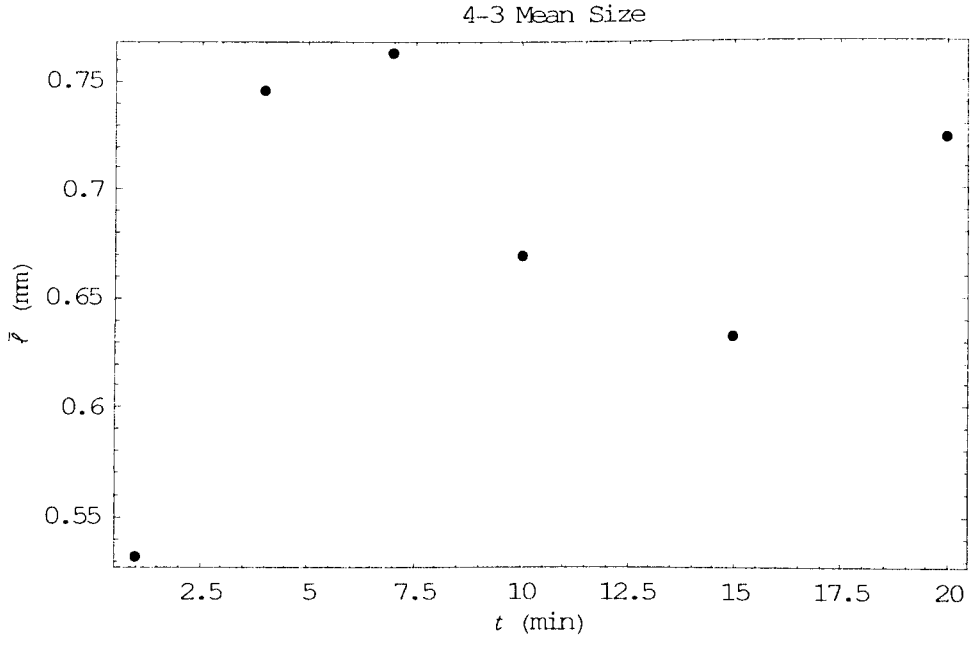

Figure 4.19: Granule mean size, $\overline{d}_{(4,3)}$, variation with granulation time for wet granulation of Durcal-40 and PEG-4000.

Figure 4.20 shows the behaviour of the granular bed in a rotating frame of reference at 1 min granulation time. The magnitude of three peaks varies slightly for each blade but does not show any major difference. V_y (Figure 4.20ii) shows some difference in maximum value attained between blade passes. This behaviour did not change much during the whole granulation period (results not shown here). It is only the velocity variation range that changed over time. The velocity variation behaviour is more like the dry granules, PEG-400 and PEG-1500 results and less like the Glycerol results as PEG-4000 has a lower viscosity than PEG-400. Being a low viscosity binder and due to the low impeller speed it shows occurrence of negative V_y between each blade pass.

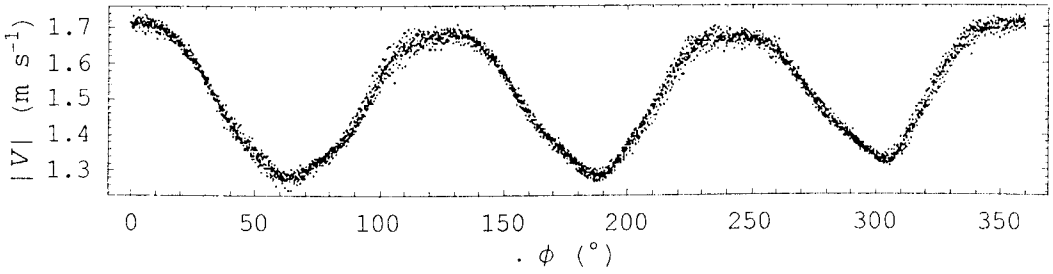

(i) Bed velocity (V).

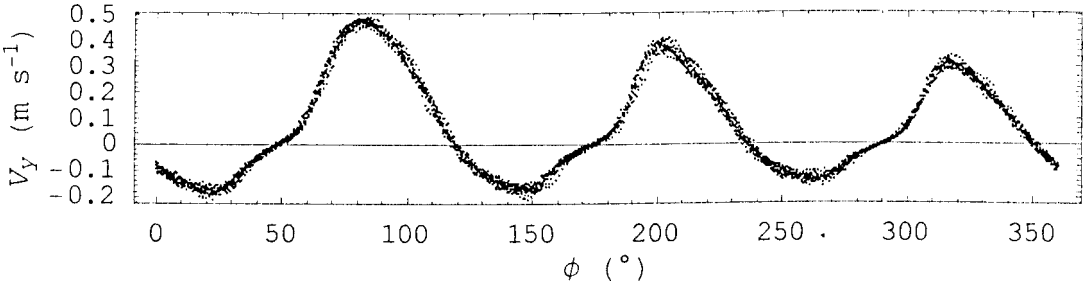

(ii) Y-component of bed velocity (V_y).

Figure 4.20: Velocity variation in a rotating frame of reference for wet granulation of Durcal 40 and PEG-4000 at 1 min of granulation time.

The frequency analysis of velocity shows major peak at blade frequency near 10 Hz in Figure 4.21. This is because PEG-4000 has a lower viscosity at 60°C which is the operating temperature of these experiments and is expected to show behaviour similar to that of PEG-400 and PEG-1500 as in section 4.3.

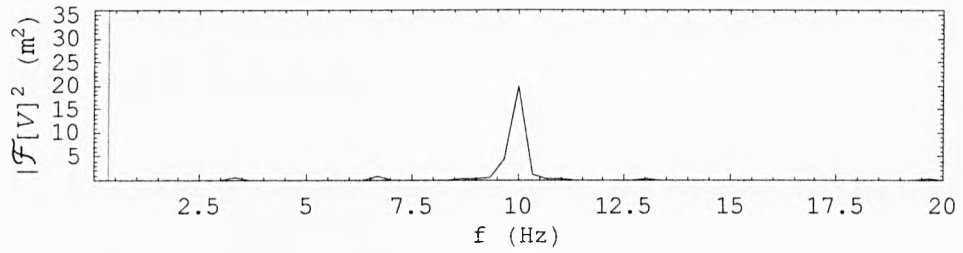

(i) For bed velocity (V).

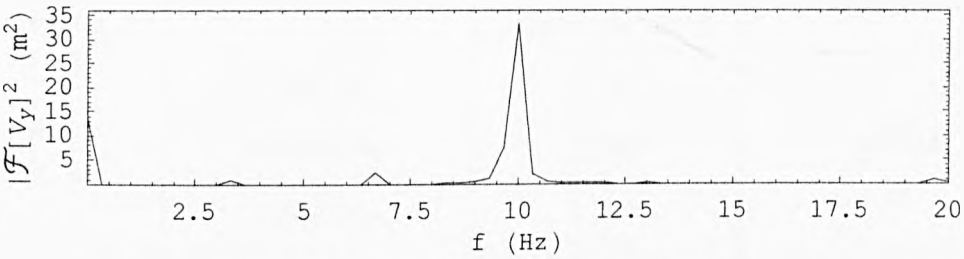

(ii) For y-component of bed velocity (V_y).

Figure 4.21: Frequency analysis of velocity for wet granulation of Durcal-40 and PEG-4000 at 1 min granulation time.

4.6 REPRODUCIBILITY OF EXPERIMENTAL RESULTS

The reproducibility of velocity results was checked by three separate experimental runs on a 2800g batch of dry granules prepared with Durcal-40 and PEG-1500 and sieved into a size range of 0.4 to 2 mm. The impeller speed was kept constant at 312 rpm and the chopper was off. The images were captured with a Photo-Sonics Phantom V7 high speed camera (EPSRC-EIP, 2006). 3000 images were captured and analysed with 'mpiv' for three experimental runs. This was a high resolution camera with 800×600 pixels image size. Only a rectangular strip of the image covering the height of the granular bed was used to investigate velocities.

These experiments showed strikingly similar results with low variation in bed velocity and its components for the three runs. The variation in magnitude between these runs is shown in Table 4.2. It shows a standard deviation of 0.0093 for bed velocity (V) which is quite low. It also shows low standard deviation for V_x and V_y. A plot of bed velocity in rotating frame of reference for all three runs in Figure 4.22 shows a similar correspondence to the impeller position with the same nature of velocity variation. These bed velocity results are adjusted to align the peaks in bed velocity so as to make a

clear comparison between these experimental runs. Aligning the peaks would also align the impeller position for each run.

Table 4.2: Results of reproducibility three separate experimental runs for dry granules under same experimental conditions.

Velocity or component	Experimental run	Average magnitude (m/s)	Standard deviation
V	First run	1.285	0.0093
	Second run	1.303	
	Third run	1.298	
V_x	First run	1.275	0.0097
	Second run	1.294	
	Third run	1.288	
V_y	First run	0.111	0.0062
	Second run	0.099	
	Third run	0.102	

It should be noted that the magnitude of bed velocity was higher for same experimental conditions at 312 rpm in section 4.2. The magnitude was above 1.4 m/s for bed velocity whereas it is around 1.3 m/s in these three runs. Similarly V_x and V_y show higher magnitude for experiment in section 4.2. This can be explained from the fact that although the size range of granules was same the particle size distribution (not measured for these cases) would have been different. As shown earlier in section 4.4 different size granules behave differently to the imparted momentum. Also as the camera position for these experiments was different from the experiments in section 4.2 it would make the comparison unfair.

It should also be noted that wet granulation experiments are sensitive to granulation conditions and should be expected to show higher variation in velocity results between separate experiments under similar conditions. Again this is because of the complexity of wet granulation, the size distribution and the binder distribution throughout the bed

varies from batch to batch to a higher extent and these parameters are also susceptible to small changes in operating conditions.

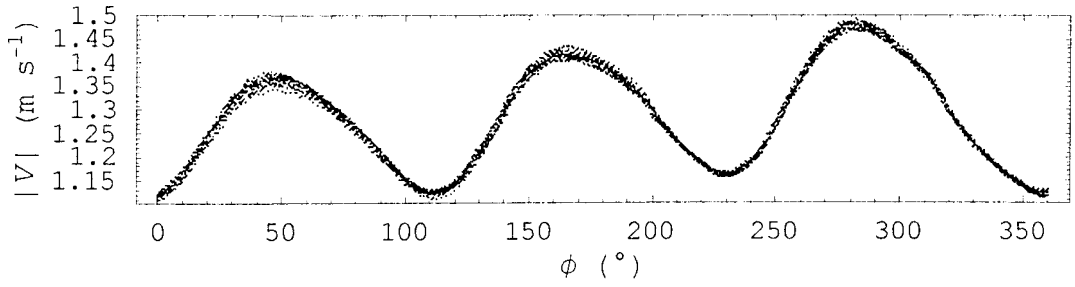

(i) First experimental run.

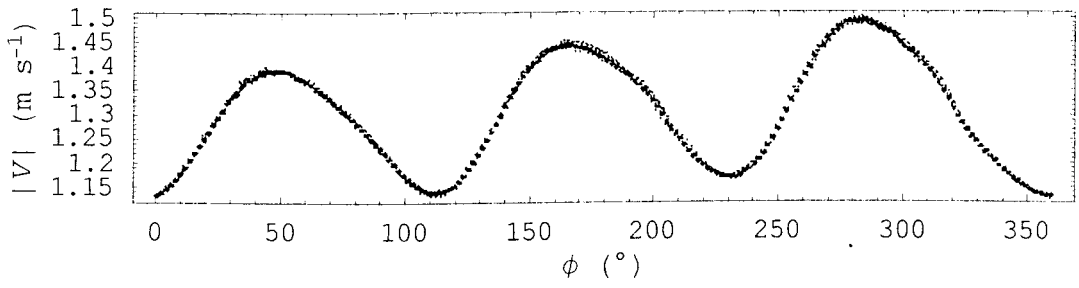

(ii) Second experimental run.

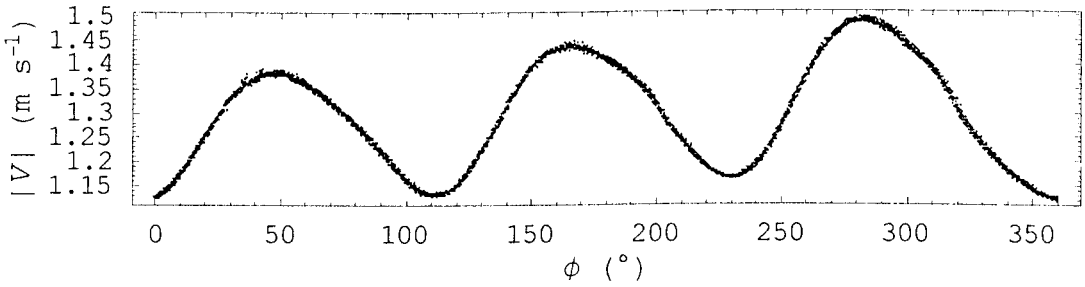

(iii) Third experimental run.

Figure 4.22: Bed velocity (V) plotted in a rotating frame of reference for three separate experimental runs for dry granule batch to compare reproducibility of experimental results under same conditions.

4.7 DISCUSSION AND SUMMARY

The averaged bed velocities showed a general increase in magnitude with increasing impeller speed. The normalised velocities, however, showed decaying behaviour with increasing impeller speed. When velocities were plotted in a rotating frame of reference, it revealed that the bed dynamics is highly dependent on the impeller or blade position. The bed-velocity represents the mean motion characteristics rather than the individual particle motion. However, it can be interpreted that the particles might be experiencing the same perturbations as that of the mean. The behaviour and magnitude of horizontal motion of the bed is similar to that of the resultant bed motion. On the contrary, it was clearly seen in the rotating frame of reference the vertical component of bed motion decreased with increasing bed velocity and vice-versa and has little effect on the magnitude of resultant bed motion. The vertical motion signifies the tumbling behaviour of the bed and the surface renewal characteristics. The toroidal nature of motion in the high shear mixer was supported in this study in accordance to the previous studies done using PEPT and high speed imaging. The existence of positive as well as negative V_y in some cases shows occurrence of a combination of bumping and roping nature. It should however be noted that while calculating the V_y, the changes in bed angle due to different behaviour of different recipes was not taken in consideration due to the constraints of the current investigating technique. The investigation of the impact of changing bed angle on the final V_y value would help in better characterisation of the flow pattern.

An increase in binder viscosity slowed down the powder bed. A ten fold increase in binder viscosity resulted in 40% decrease in bed velocity magnitude. The impact of individual blades on bed was clear in case of low viscosity binder whereas high viscosity binder showed a pronounced signature of the impeller as a whole rather that the individual blades.

The higher size range granules exhibited higher velocities as compared to smaller granules. This phenomenon was justified by momentum transfer loss between particles and trajectory segregation between different sized granules. In case of smaller particles the number of granules in same amount of batch is high causing more loss in momentum transfer from impeller to granules at the surface. In a study by Plank et al. (2003) a 10 fold difference was noticed between dry powder and agglomerated mixture

velocities. This study can be logically related to the velocity variation according to granule size as the dry powder being fine absorb most of the energy.

For a wet granulation experiment, the velocities depend on a combination effect of average granule size and availability of free binder on surface throughout the process. The velocities were found to be low at the start due to free binder and presence of fine powder in the bed. They were highest in the middle period when the granules are big and binder in free form is scant. Velocities were steadied in the later part of granulation when the granules assumed a constant mean size and binder is squeezed out on the surface due to compaction.

The results are highly reproducible at least for dry granules. The velocities are expected to show variability for wet granulation experiments due to changes in operating and environmental conditions on a batch-to-batch basis. The surface velocity calculation is of direct relevance to the calculation of dimensionless spray flux (Eq. 2.2). Although this would require velocity analysis for dry powders as the binder is added onto dry feed material. Dry powder flow dynamics are anticipated to be different with low speeds due to higher energy absorption. The analysis of V_y in rotating frame of reference should provide an insight into the mixing effectiveness.

A bigger goal is tried to be achieved in these experiments that of correlating the effect of operating conditions and feed material properties on the granulating mixture dynamics. The next step is to look at the particle dynamics especially to deduce collision frequencies. The velocity variation was found to be highly correlated to the impeller position and geometry (3 blades). This made the task of separating the velocity fluctuations at a point from the bed velocity (ensemble velocity) difficult for further analysis of collision frequencies. So the next chapter deals with understanding the flow in a simpler system in which the mean (and particle) motion would not be a complex function of mixer geometries.

5

MOTION WITH A DISC IMPELLER

The aim of the research as started was to investigate mean motion as well as particle motion. But the systematic variation in mean motion as seen in chapter 4 made it difficult to separate the mean motion from the particle motion. The solution to make the mean motion simple was to carry out experiments with simpler equipment that would not create a complicated mean motion correlated to the equipment geometry. For this reason a disc impeller was tried in place of the 3-blade impeller. A disc impeller is simply a flat circular disc that could fit on the impeller shaft as shown in Figure 5.1. The experiments were performed on dry granules and the dynamics of the motion was investigated with VidPIV® software. The velocity at single interrogation area was analysed to estimate collision frequency based on Equi-partition of Kinetic energy Kernel (EKK) and radial distribution of velocities was analysed to estimate Smoluchowski Shear Kernel (SSK).

5.1 EXPERIMENTAL

The disc impeller used for these experiments was custom built to simplify the mean flow. The disc impeller was cut into shape out of a solid block of aluminium. Examples of disc impeller studies in high shear granulation can be found in literature (Holm et al., 1996; Muguruma et al., 2000; Knight et al., 2001a).

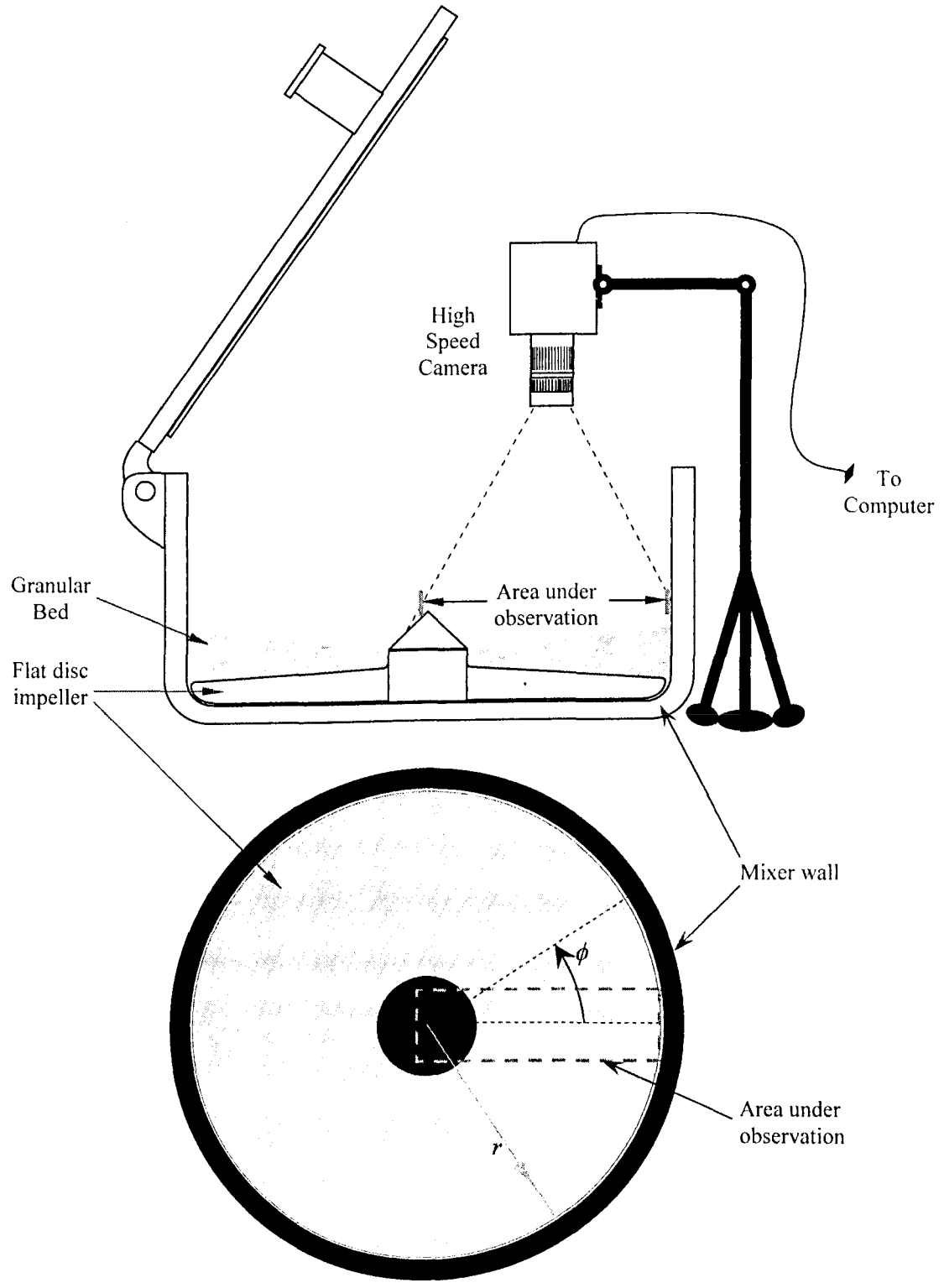

Figure 5.1: Experimental set-up for disc impeller experiments. Top figure: the cross-section of the mixer showing the camera focused vertically downwards. Bottom figure: Top view of the mixer showing the area under observation. It also shows the radial distance (r) and angle ϕ measured at the centre of the disc from the point of observation. For calculating the bed velocity, part of the central shaft in the area under observation was annotated.

5.1.1 Set-up

The granular flow in the case of a flat disc impeller was observed to be different from that for the 3-blade impeller. The bulk of the granules tended to sit on the disc impeller and form a slightly slanted profile from the mixer wall to the centre of the mixer under the experimental conditions. So the high speed camera was focused vertically downwards on to the granular bed as shown in fig 5.1. The camera captured the bed profile variation along the mixer radius from the centre to the wall of the mixer. A seal was fitted between the impeller edge and the mixer wall to prevent the granules from entering the gap between the impeller and the mixer bottom that would otherwise choke the impeller movement. This seal was effective enough for granules for short period of time but was found to be ineffective for fine powder. This was a drawback as the experiments then had to be limited to granules only and no fine powder required for wet granulation could be used.

5.1.2 Material

The granules used for these experiments were dry and made of Durcal-40 and PEG-1500. Several batches of Durcal 40 and PEG-1500 were granulated and then sieved into a size range of 0.71 to 2 mm to make up 2800 g of test material.

5.1.3 Procedure

The batch of dry granules was fed into the mixer. The impeller was started and image capturing was started after the impeller reached the specified impeller speed (i.e. 312 rpm). A Kodak HS – 4540 was used for this experiment. 3000 images were recorded at a framing rate of 1125 fps. So a total recording of approximately 2.67 sec was done. Velocity analysis was done in VidPIV® software at an interrogation size of 16 by 16 pixels. The output velocity files were analysed for bed velocity as well as velocity at a single interrogation area and this is discussed in sections 5.2 and 5.3 respectively.

5.2 BED VELOCITY AS A FUNCTION OF TIME

The bed velocity (V) is an average of the array of velocities over the area under observation that takes into consideration the entire radius after annotating the central shaft part in velocity calculation. This bed velocity (V) is plotted as a function of time (t) in seconds as shown in Figure 5.2. The bed velocity shows a flat profile with time. The positive velocities here mean that the mean motion is in the direction of the impeller rotation according to sign conventions used for velocity evaluation. It does not show any regular pattern of velocity variation although there are couple of dips evident that seem to be repetitive. So a further Fourier analysis was done to check whether the pattern of velocity variation was repetitive and whether it was dependent on equipment used and if so then its influence.

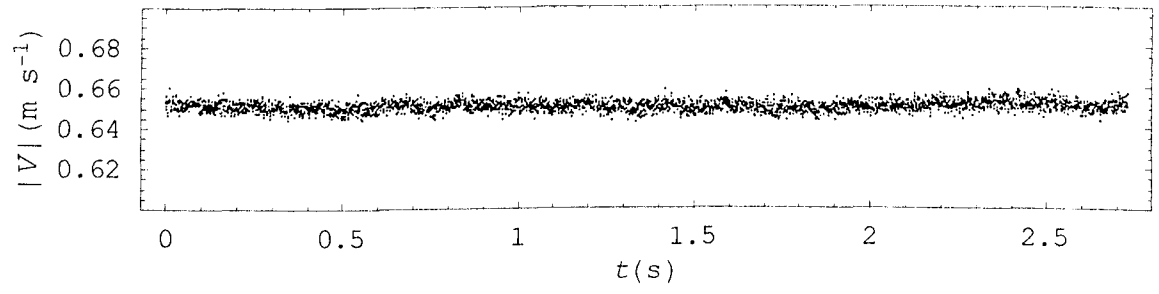

Figure 5.2: Bed velocity at 312 rpm impeller speed.

Frequency analysis of bed velocity shown in Figure 5.3 shows a major peak near to the frequency of the disc impeller (5.2 Hz). The magnitude of this peak (~0.0002 m^2) is far small when compared to similar frequency for the 3-blade impeller e.g. ~2 m^2 in Figure 4.8, and hence its impact on the flow behaviour can be neglected. The next step would be to analyse the velocity at a single interrogation area as bed velocity variation is found to be simple and independent of surrounding influences such as impeller shape.

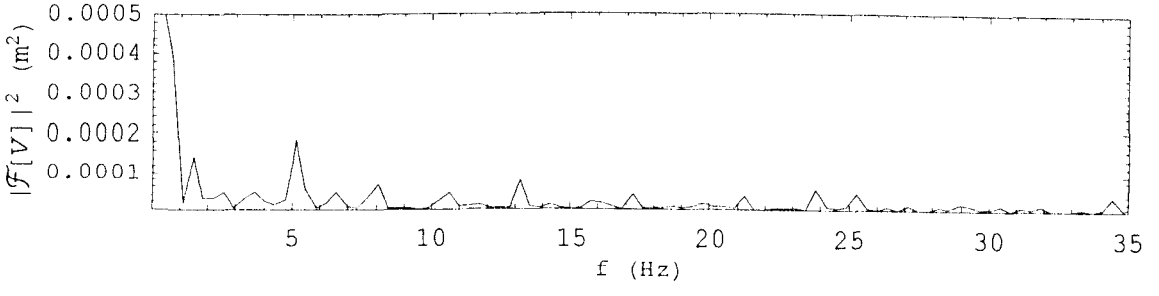

Figure 5.3: Power spectrum of bed velocity at 312 rpm impeller speed.

5.3 VELOCITY VARIATION AT A SINGLE INTERROGATION AREA AS A FUNCTION OF TIME

The velocity vectors from a centrally located interrogation area (Coordinates: x =106, y = 145 pixels) on the granular bed were extracted corresponding to a time duration of 2.67 s. This area is approximately the centre of the radial distance from the impeller centre to the wall of the mixer. Each velocity data point at this position is an average calculated over an area of a size of 16 by 16 pixels (5.3 × 5.3 mm) at the particular time instance in the cross-correlation process in VidPIV®. This velocity is assumed to be representative of the prevalent particle velocities as the size of the individual particles was in the range of 2-7 pixels (0.71 to 2 mm range) as one pixel was approximately 0.33 mm in size. This approximation however needs to be scrutinised in future work as more number of granules in a single interrogation area can lead to attenuated value of granular temperature. One of the possible ways of increasing accuracy is to look at high resolution of a single granule that is by focussing the camera at a smaller window size of the granular bed. The time variation of tangential component of velocity at this region is plotted in Figure 5.4. This plot predominantly shows a velocity varying randomly with time with a spread in an approximate range of 0.7 to 0.85 ms^{-1}. Again the magnitude is positive exhibiting a flow with the direction of rotation of the disc. The magnitude of velocity at this location is quite high compared to the average bed velocity plotted in Figure 5.2 due to the existence of a velocity gradient across the radius of the mixer as will be clear in Figure 5.6 later. The data is subjected to Fourier analysis to check whether there is any systematic component hidden. The power spectrum of this velocity variation in Figure 5.5 shows minor peaks at various frequencies. These peaks show little correspondence to any physical parameter. No major frequency and its multiples can be figured out from Figure 5.5. So the fluctuations in the range 0.7 to 0.85 ms^{-1} can indeed be considered as random and independent of the influence of the impeller geometry. Existence of such a random motion in normal operation which is not dependent on surrounding influences supports the theory of chaotic motion of granules. It is important here to mention that the particle motion is expected to have a component of velocity that exhibits the mean behaviour and another fluctuating component independent of surrounding that would cause the collisions among particles. It is this random component that is important to be identified for calculation of collision velocities if the EKK is to be applied.

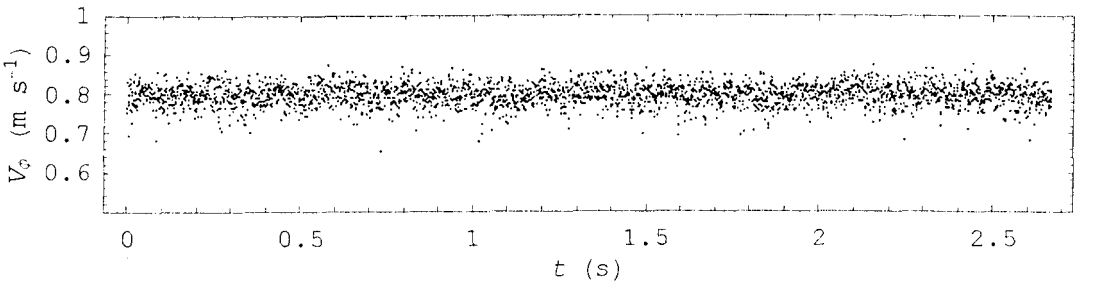

Figure 5.4: Azimuthal component of velocity (V_ϕ) at position x =106, y = 145, at 312 rpm impeller speed.

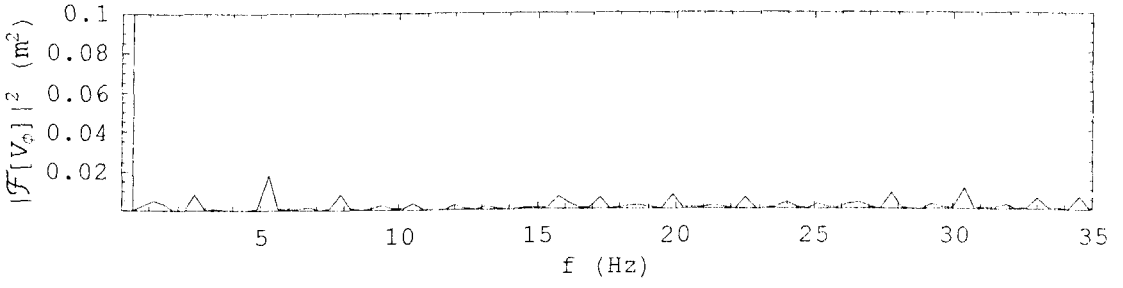

Figure 5.5: Fourier analysis of temporal variation in V_ϕ at position (106, 145) pixels, at 312 rpm impeller speed.

5.4 CALCULATING COLLISION RATE BETWEEN PARTICLES

As the velocities approximating particle velocities are deduced, the next step would be to look at collision rates. The collision rates or frequencies are an indication of how often the particles collide that would result in either an aggregate formation or rebound. As discussed previously in chapter 2, two aggregation kernels EKK & SSK are calculated and compared in this section. For SSK it is necessary to calculate the shear rate first. Whereas, for EKK to be applied it is necessary to show that the particle fluctuating velocities are Gaussian (random).

5.4.1 Collision rate based on shear

The collision frequency based on shear rate (β_{SSK}) suggested by Smoluchowski (as in Eq. 2.14 described in chapter 2) is given by:

$$\beta_{SSK} = \frac{\dot{\gamma}}{6}(l_i + l_j)^3 \qquad (2.14)$$

As the granules were moving in a cylindrical geometry, Cartesian coordinates in the images were converted to polar coordinates. Based on the knowledge of velocity vector field the shear rate ($\dot{\gamma}$) in the above equation can be calculated from equation:

$$\dot{\gamma} = r\frac{\partial}{\partial r}\left(\frac{V_\phi}{r}\right) + \frac{1}{r}\frac{\partial V_r}{\partial \phi} \tag{5.1}$$

where r is radius and ϕ is angle of the impeller, V_r is the radial velocity and V_ϕ is the azimuthal velocity. In this case average velocities are required, and so time average data over the sample period of approximately 2.67 seconds is used. It is also assumed for this analysis that axisymmetric behaviour is exhibited by the flat disc and therefore there is no reason to expect the radial velocity, V_r, to be a function of angle (ϕ). So Eq. 5.1 reduces to:

$$\dot{\gamma} = \frac{dV_\varphi}{dR} - \frac{V_\varphi}{R} \tag{5.2}$$

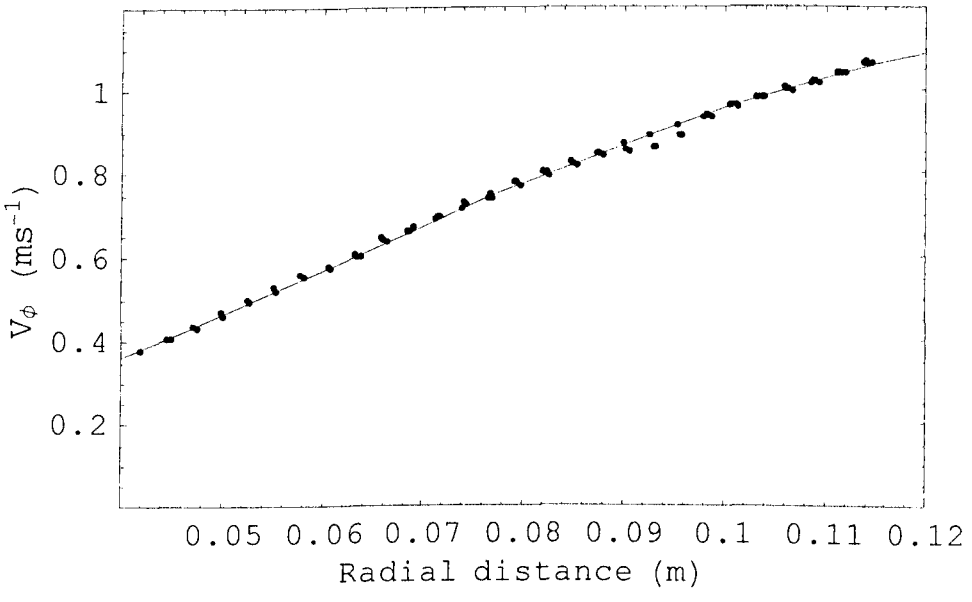

Figure 5.6: Average azimuthal bed surface velocity (V_ϕ) as a function of radial position showing a fitted polynomial used for calculating the shear rate, $\dot{\gamma}$.

Figure 5.6 shows the average azimuthal velocity as a function of radius calculated from the bed surface velocity measurements. The dots in the graph show average azimuthal velocity at a particular interrogation area along the radius of the mixer. Each of the individual group of points at a particular radial distance is an average over three

adjacent interrogation areas. A polynomial fitted to the azimuthal velocity data gives Eq. 5.3.

$$V_{\varphi} = 7.056R + 64.92R^2 - 399.37R^3 \tag{5.3}$$

Calculating the shear rate from Eq. 5.2 using Eq. 5.3 gives Eq. 5.4.

$$\dot{\gamma} = 64.92R - 798.74R^2 \tag{5.4}$$

The average shear rate along the radial distance can be calculated as:

$$\bar{\dot{\gamma}} = \frac{\int_{R_1}^{R_2} \dot{\gamma}(r)\, r\, dr}{\int_{R_1}^{R_2} r\, dr} \tag{5.5}$$

The absolute value of average shear rate along a radial distance between 0.04 and 0.12 was calculated as 0.762 s^{-1} using Eqs. 5.4 and 5.5. As explained in section 2.5.2 (Eq. 2.14), the size independent collision rate constant is $\dot{\gamma}/6$. Therefore, the SSK rate constant is:

$$\beta_{0,SSK} = 0.127 \ s^{-1} \tag{5.6}$$

The azimuthal velocity profile in Figure 5.6 can also be compared with the results of disc impeller study by Muguruma et al. (2000) as discussed in section 2.2.2. The velocities in their case varied in the range of 0.5 to 1.3 ms^{-1} as in Figure 2.3(a). These are little higher than the velocities shown in Figure 5.6, which is expected due to the 1.92 mm mono-disperse particle size range used by them as opposed to 1.36 mm average particle size used in experiments here. Muguruma et al. (2000) showed an angular velocity profile decreasing with impeller radius for the quarter part of the radius near to the mixer wall. The results in Figure 5.6 are at least 2.75 cm away from the wall and the velocity profile near the wall could be different. It is also possible that the velocities noticed here are low due to slippage between the granular material and disc impeller similar to that noticed by Wellm (1997) in his experiments (refer section 2.2.3).

5.4.2 Collision rate based on random motion

Figure 5.7 shows the probability density function of the tangential velocity at point (106, 145). As the Fourier analysis of the velocities at this location revealed a negligible systematic component, the average velocity from this data was simply subtracted to find the velocity fluctuations in azimuthal velocity represented by C_ϕ. This C_ϕ data shows a comfortable fit to Gaussian distribution function (Eq. 2.9) as shown in Figure 5.8.

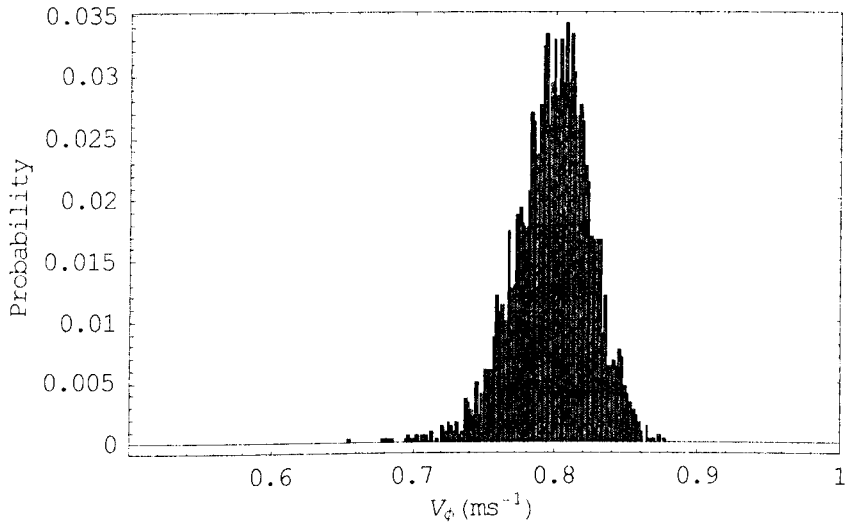

Figure 5.7: Distribution of azimuthal velocity, V_ϕ, for a single interrogation area on the bed surface over a sample period of 2.67 seconds.

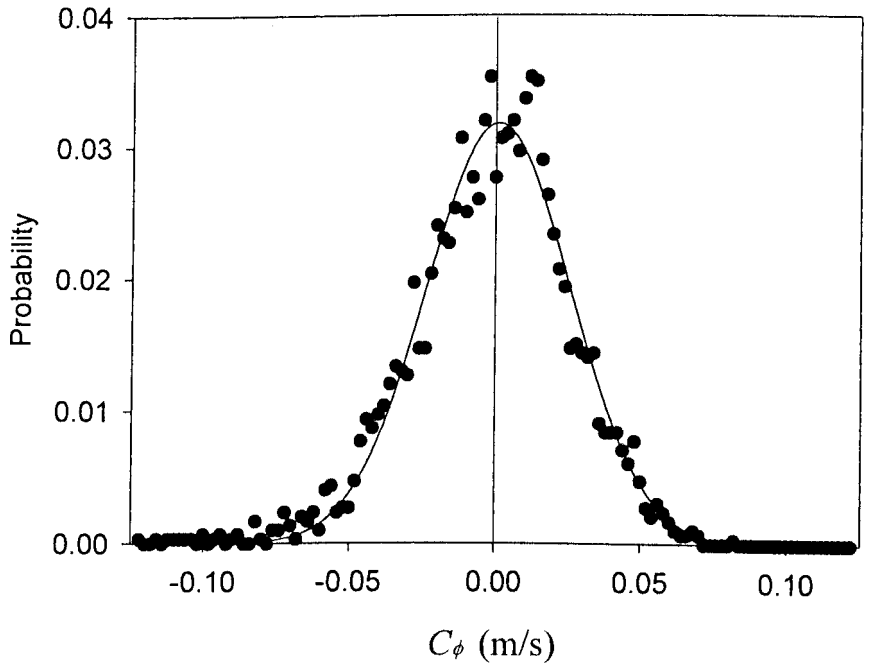

Figure 5.8: Probability density function of azimuthal velocity fluctuations (C_ϕ) with a Gaussian function fit.

Similar analysis to that shown in Figure 5.7 and 5.8 was done on radial component of velocity. The value of standard deviation was found from the Gaussian curve fit and granular temperature in each direction was calculated as square of the standard deviation (equal to variance). The average granular temperature for the single location was calculated by averaging the components of granular temperature in each direction. The standard deviations of the Gaussian curve fit were found to be 0.025 and 0.017 ms^{-1} in tangential and radial directions respectively. According to Kinetic Theory of Granular Flow, the fluctuations in granular velocities are isotropic. But the standard deviations measured in the two orthogonal directions differ by approximately 50%. This is however not favourable needs to be looked at as a first ever estimation and a more accurate investigation such as by increasing spatial resolution of images would be desirable. From the values of standard deviations, the values of granular temperature in tangential and radial directions were found to be 6.2 $\times 10^{-4}$ m^2s^{-2} and 2.9 $\times 10^{-4}$ m^2s^{-2} respectively resulting in an average granular temperature (θ) of 4.5 $\times 10^{-4}$ m^2s^{-2}.

The Gaussian fit is clearly good and provides compelling evidence for using KTGF to calculate the granular temperature. However, it is also possible that if there is a random error in the velocity calculation, it would also show a Gaussian distribution. As previously discussed in section 3.3.3.2, the R.M.S. error at the setting of this analysis (recursive MQD with 50% overlap, interrogation window size 16×16 pixels) was estimated to be in the lower range of 0.005 to 0.01 (in pixel). Let's assume RMS error in PIV calculation of 0.0075 (pixel). This value needs to be converted to units of variance of the Gaussian distribution, i.e. m^2 s^{-2}, for a fair comparison. The size of a single pixel was calculated as 3.32 $\times$ 10^{-4} m and the time difference between two successive images was 8.88 $\times$ 10^{-4} s. So in the units of granular temperature, the error in measurement would be 7.84 $\times$ 10^{-6} m^2s^{-2}. This error is low, in the range $1/9^{th}$ to $1/6^{th}$ of the granular temperature values and shouldn't be a concern for further analysis.

In an ideal case, the modelling parameters such as the granular temperature, the size distribution, the velocity distribution at each point in the mixer would be taken into consideration. However here a global approach is taken into account and a scrutiny at a very high level is avoided. For example the mixture granular temperature is a function of the granular size and the granular temperature as in Eq 2.12, but only an average value of these two will be used to estimate the former. So to calculate the mixture

granular temperature (Eq. 2.12), an average granule mass is required. For this, the average granule density was calculated to be 2500 kg/m^3 based on the primary particle bulk density (2690 kg/m^3) and the binder density (1100 kg/m^3) in a ratio of binder to solid mass of 0.13. The average granule size for calculation purpose is assumed as 1.36 mm based on size range 0.71 to 2 mm. From this data the mixture granular temperature (θ_S) (Eq. 2.12) was calculated to be 1.47×10^{-9} kg m^{2}s^{-2}. Using Eq. 2.13, the EKK rate constant can be calculated from the mixture granular temperature. As these were the preliminary experiments towards understanding particle collision dynamics, here the collision rates are of interest rather than a discussion of collision efficiency and hence the true rate of aggregation. Therefore the aggregation efficiency (ψ) in Eq. 2.13 can be taken as unity. However the radial distribution function (g_0) is still required. This has not been determined, but Gidaspow and Huilin (1998) present the following relationship for calculating an average radial distribution function, g_0, based on the solid volume fraction, ε_S, and the maximum solid volume fraction, ε_m:

$$g_0 = \left[1-\left(\frac{\varepsilon_S}{\varepsilon_m}\right)^{1/3}\right]^{-1} \tag{5.7}$$

Using $\varepsilon_m = 0.636$ for random packed solid spheres and assuming a solid volume fraction of 0.5 in the high shear mixer, the value of g_0 was calculated to be 12.98. From this, the EKK rate constant was calculated from Eq. 2.13 to be:

$$\beta_{0,EKK} = 1.18\times10^{-5}\ \text{m}^{2.5}\text{s}^{-1} \tag{5.8}$$

It is important to point out here that the above estimate is made on the basis of the observations on the surface only. Again the velocities and so the granular temperatures inside the bed are expected to be different than that at the surface resulting in different values of the collision rate.

5.5 COMPARISON BETWEEN COLLISION RATES BESED ON SHEAR AND ON RANDOM MOTION

So far the results have shown that the shear rate and the granular temperature can be calculated from the measured bed surface velocity. It would be of interest to examine the magnitudes of the collision rates from these two mechanisms in order to assess which is of more importance. The SSK and EKK rate constants have already been calculated from the experimental data (Eq. 5.6 and 5.8). In order to compare the relative magnitudes of the SSK collision rate and the EKK collision rate, the size dependent term needs to be evaluated as well. Again, using the average size of 1.36 mm, the overall collision rates are evaluated as (using Eq. 2.11 and Eq. 2.14):

$$\beta_{EKK} = 2.5\times10^{-6}\,m^3s^{-1}$$
$$\beta_{SSK} = 2.56\times10^{-9}\,m^3s^{-1} \qquad (5.9)$$

This comparison suggests that, at least in this case of a flat disc impeller, that granule collision frequency caused by random motion dominates over shear induced collision. This is certainly an interesting result but of a limited use as it stands on its own due to the use of a flat disc impeller, and a number of assumptions that require some more rigorous justification. However, it does contribute to observations that have been made previously (e.g. Hounslow et al., 2001) that the SSK is relatively poor at describing granule size distributions in high shear granulation, compared to the EKK. Additionally it provides confidence in exploring the effect of random motion within high shear granulation as a mechanism for granule collision and the potential for KTGF to be used as a tool for modelling granule motion in high shear granulation.

Aggregation Efficiency

Principally the results and discussion have centred on collision frequency. However this is still not sufficient to describe the granulation process. In addition to an understanding of collision frequency, an understanding of aggregation efficiency is required. When the granules do collide, how often to they stick to each other? The collision frequency of the granules may be high, but if the aggregation efficiency is very low, then a low rate of aggregation might be observed.

As a first step to investigating this, a comparison is made with a published value for the EKK aggregation rate constant. Hounslow et al. (2001) present an EKK aggregation

rate constant of 1.3×10^{-9} kg $m^{0.5}s^{-1}$. Their model included breakage rates, however these were relatively low. Using the same average size of 1.36 mm for the size dependence gives an EKK aggregation rate of 5.54×10^{-13} m^3s^{-1}. Comparing this with the collision rate in Eq. 5.9 suggests that the aggregation efficiency could be of the order of 2×10^{-7} (i.e. only about 2 in 10 million collisions results in aggregation). This appears very low, but as stated it is very much a first step estimate. It is at least reassuring that it is somewhere between zero and unity. Obviously this is not a fair comparison used in this estimate. Although the materials and equipment used between the published aggregation rate and the collision rate calculated here were similar, the published rate was from a granulation experiment using a 3-blade impeller.

5.6 CORRELATION ANALYSIS OF VELOCITIES

As the particles are moving in a velocity field, they will collide with each other due to the difference in their velocities. Suppose if the variation in velocities between the colliding particles is similar to each other then they will not come in contact or rather follow the flow of the bulk. As mentioned in section 2.4.1, it is also necessary to show that the velocities of particles involved in a collision are independent of each other or in other words are uncorrelated to satisfy the assumptions of KTGF in order to apply KTGF. A fair analysis to prove this point would be to look at the correlation between the fluctuating velocity components of adjacent non-overlapping interrogation areas. Correlation is a general term for correlation coefficient between two random variables. In this case, the C_x and C_y are (supposedly) random variables. The value of correlation can vary between 1 and -1 (Moore et al., 1999). A positive correlation means an increasing relationship and a negative correlation means a decreasing relationship between the random variable. Values near to 1 or -1 means that the variables are dependant on each other strongly and values nearer to 0 means the correlation is weak and the variables are independent. The Pearson's sample correlation coefficient (r) can be written as (Devore et al., 1994):

$$r = \frac{\sum(x-\bar{x})(y-\bar{y})}{\sqrt{\sum(x-\bar{x})^2\sum(y-\bar{y})^2}} \tag{5.10}$$

where x and y are the two random variables and $\bar{x}$ and $\bar{y}$ are the means of x and y respectively. Ideally, a correlation for velocities in 3D would be desirable as the

granules are moving a 3D geometry. But due to the limitation of the current investigating technique, a correlation analysis in 2D has to be done.

As the interrogation analysis was done with 50% overlap between adjacent interrogation areas, instead of choosing the adjacent interrogation areas alternate areas were chosen for correlation analysis in which case the velocity calculations at each area would be independent of the other areas. Four alternate interrogation areas are shown in Figure 5.9. Distance between the centres of interrogation areas for example between {1} and {2} was 16 pixels and each interrogation area size was of 16 by 16 pixels (5.3×5.3 mm) dimension. To understand the correlation between the velocities at these alternate areas, temporal fluctuating velocities (C_ϕ and C_r) at {1} were correlated to temporal fluctuating velocities at {2}, {3} and {4} and similarly that at {2} correlated to velocities at {3}. This covers all possible direction for correlation except the direction perpendicular to the surface in 3rd dimension.

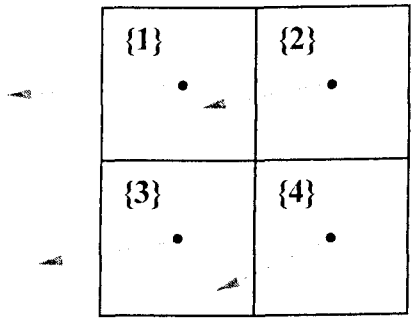

Reference point coordinates in pixels:
{1} = (122, 121)
{2} = (138, 121)
{3} = (122, 137)
{4} = (138, 137)

Figure 5.9: Depiction of velocity vectors at four adjacent non-overlapping interrogation areas.

Table 5.1: Correlation coefficient (Eq. 5.10) values between adjacent non-overlapping interrogation areas from Figure 5.9.

Velocity component	Interrogation areas	{1}	{2}	{3}	{4}
C_ϕ	{1}	1	-	-	-
	{2}	0.074	1	-	-
	{3}	0.081	0.032	1	-
	{4}	0.063	-	-	1
C_r	{1}	1	-	-	-
	{2}	0.010	1	-	-
	{3}	-0.016	-0.022	1	-
	{4}	0.030	-	-	1

Table 5.1 shows that the correlation between alternate interrogation areas is less than 8% for C_ϕ and less than 3% for C_r. The level of correlation is insignificant and proves the point that the granules are moving independent of each other and comply with the theory of chaotic motion of particles responsible for particle-particle collisions in KTGF.

5.7 DISCUSSION AND CONCLUSION

The bed surface velocity field of a high shear mixer fitted with a flat disc impeller was analysed to determine the shear rate and distribution of fluctuating velocities. The temporal velocity fluctuations at a fixed point were found to fit a Gaussian distribution, consistent with KTGF from which the granular temperature was determined. The collision rates due to shear and that due to random motion were calculated and compared. The collision frequency due to random motion was found to be approximately three orders of magnitude larger than that due to shear suggesting that random motion plays a dominant role in the particle-particle collision and provided further support for the use of the EKK over the SSK in population balance modelling of high shear granulation. A brief discussion on the aggregation efficiency suggests that it may be of the order of 10^{-7} with very few of the many granule-granule collisions resulting in aggregation for the condition considered. The correlation analysis of velocities between alternate interrogation areas showed poor correlation confirming the random behaviour of fluctuations in velocities at these points.

The disc impeller was primarily built to simplify the flow structure but was found to be unsuitable for real granulation experiments. This limited the ability of simultaneous measurement of collision frequencies and aggregation rates. Similar commercial high shear mixers equipped with a disc impeller can be employed to understand the flow behaviour during real granulation process. Due to this fact further analysis was carried out on real granulation experiments with the 3-blade impeller (in chapter 6).

6

ESTIMATION OF AGGREGATION EFFICIENCY

The previous chapter described dominance of EKK based collisions over SSK. The important difficulty in the previous chapter of simultaneous extraction of aggregation rates and estimation of collision rates in granulation to understand aggregation efficiencies is addressed in this chapter. The experiments in this chapter deal with the 3-blade impeller instead of a disc impeller. The collection of samples during experiments and subsequent determination of granule size distribution (GSD) helped in statistical extraction of aggregation rates prevalent in a high shear granulation process by using population balance equations. A methodology to extract collision frequency based on EKK is developed different from the methodology in previous chapter. This was made possible by calculating fluctuation in velocities at a localised point on the bed surface by fitting a Savitzky-Golay Derivative (SGD) curve to the temporal variation in velocities at that point. By comparing the aggregation rates and the collision rates, the aggregation efficiencies are estimated.

6.1 EXTRACTION OF VELOCITIES AT A SINGLE INTERROGATION AREA

The experimental setup was as described in section 3.1. The experimental data sourced for this analysis is from section 4.5, which is the experiment for comparing velocity with granulation time. The granulation of Durcal-40 and PEG-4000 was carried over a period of 20 min. During this experiment granule samples were collected to measure the GSD and simultaneously images were recorded for velocity measurement. The powder bed surface velocity field was obtained from these high speed images using 'mpiv' (Mori et al., 2003), the PIV toolbox in MATLAB (refer section 3.3.3) with recursive

MQD algorithm at 50% overlap between adjacent interrogation areas each of 8×8 pixels size. For the analysis in this chapter, velocity data at a central interrogation area of size 8×8 pixels as shown in Figure 6.1 was binned. This data was extracted from 2999 image pairs of 3000 images recorded over 3 sec at 1000 fps recording speed. So the final data was a matrix of 2999 velocity data points with time. The 8×8 pixels area is assumed to represent the particle velocities at the bed surface as it approximately represents 2×2 mm size area on the bed surface. This compares well with the mean size of the granules, which varied in the range of 0.5 to 0.8 mm (Table 6.2), found from the GSD of the samples collected during granulation. The velocities were sampled for both x and y components at time intervals of 1, 4, 7, 10, 15 and 20 min during granulation. The reference x and y directions are also shown in Figure 6.1.

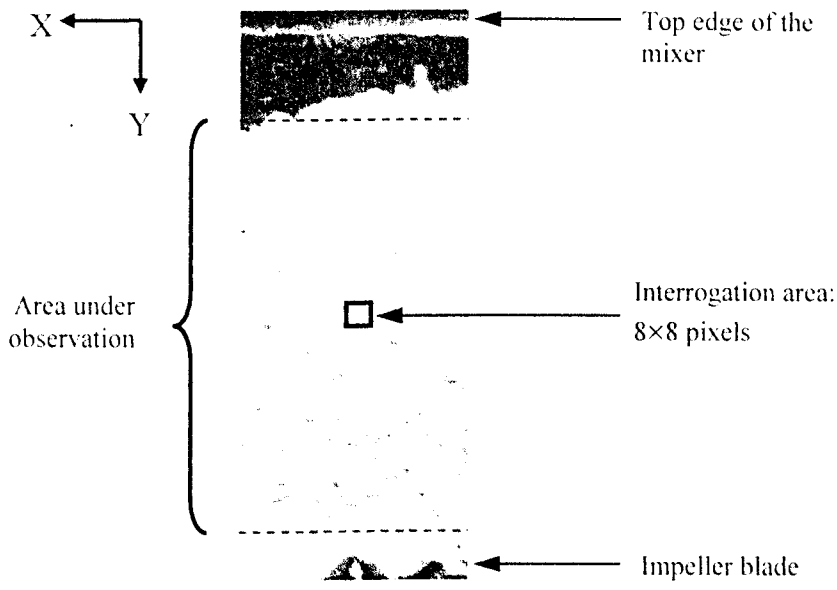

Figure 6.1: Extraction of velocity from a central region as an average over an interrogation area of 8×8 pixels approximated to granular velocities.

The distribution of x-component of velocity (V_x) at this interrogation area is shown in Figure 6.2 at 1 min granulation time. The velocities at this central interrogation area are in the range of 1 to 2 ms^{-1} and show a similar behaviour to the average bed velocity behaviour plotted in Figure 4.17(i). The range of velocity variation (1 to 2 ms^{-1}) is bigger at this point compared to average bed velocity in Figure 4.17(i). This should be expected as the bed velocity is an average of low and high velocities across the bed surface. Particle velocities are expected to be higher near the impeller blade as was found in various PEPT studies on HSM such as by Stewart et al. (2001a). This

phenomenon as previously discussed can be attributed to loss in momentum during its transfer from impeller to the particles and then to the particles further from the impeller.

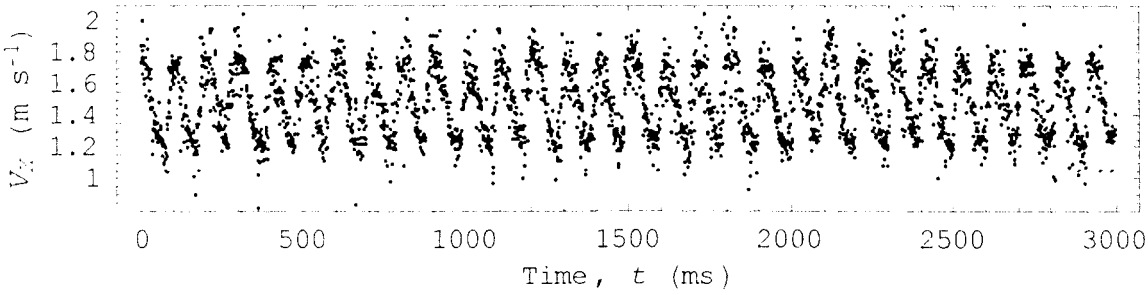

Figure 6.2: X-component of velocity (V_x) variation for the interrogation area shown in Figure 6.1 at 1min granulation time of wet granulation of Durcal 40 and PEG-4000.

6.2 FLUCTUATIONS IN VELOCITY AT A SINGLE INTERROGATION AREA

The importance of velocity data at a single interrogation area is that it should represent the fluctuation in particle velocity. So a methodology needs to be developed to differentiate between the mean motion or the motion of particles due to the bulk material and the fluctuations in velocity in short time intervals irrespective of the bulk. These fluctuations would cause the particles to collide and thus coalesce or otherwise. Periodic averaging is not an option in this case as it will not negate the effect of the impeller position/geometry. Although the velocity data in Figure 6.2 looks sinusoidal, it was found to be unsuitable for fitting a sinusoidal curve and sinusoidal curves did not provide a comfortable fit. So instead Savitzky-Golay smoothing filter which is a low pass filter was chosen.

Savitzky-Golay smoothing filter

A low pass filter basically replaces data points with local average of surrounding data points. If the underlying function has a nonzero second derivative then a simple filter would introduce bias in the averaging, whereas Savitzky-Golay (SG) smoothing filter preserves the higher moments in the data and at the same time reduces the distortion of essential features of the data. It approximates the underlying function by a polynomial of higher order, typically quadratic of quartic. For a detailed discussion on SG smoothing filter the reader can refer to Press et al. (1992). The curve obtained from SG smoothing filter is fitted to the velocity data at the single interrogation area and a

residual C_x and C_y corresponding to V_x and V_y is calculated. The fit for V_x and V_y at 1 min granulation time are shown in Figures 6.3 and 6.4 respectively.

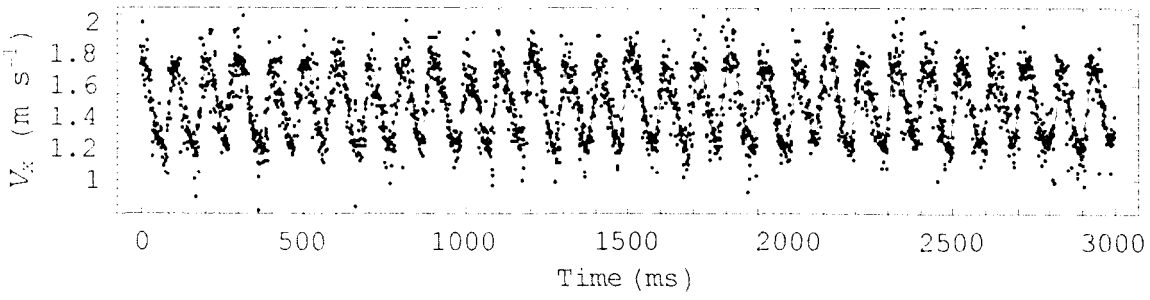

Figure 6.3: V_x from Figure 6.2 fitted with Savitzky-Golay derivative.

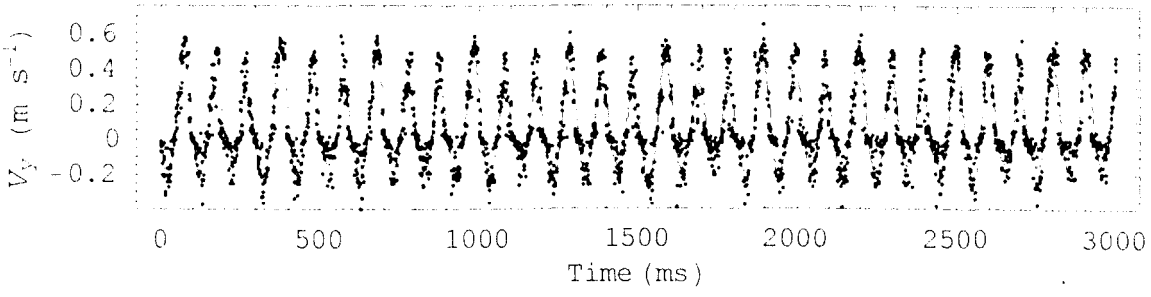

Figure 6.4: Y-component of velocity (V_y) at a single interrogation area at 1 min granulation time fitted with Savitzky-Golay derivative.

6.3 CALCULATING GRANULAR TEMPERATURE (θ)

The probability distribution curves of residuals C_x and C_y at 1 min granulation time are plotted in Figures 6.5(i) and 6.5(ii) respectively. These velocities are the fluctuations in particle velocity that are responsible for collisions among particles. Figure 6.5 also shows a comfortable Gaussian fit to these fluctuating velocities confirming the random nature of particle velocity fluctuations. The granular temperature (θ) is extracted from these fits as the square of standard deviation (σ^2). Average θ is found by averaging granular temperature in both orthogonal directions of the velocity field on the bed surface. The θ_x and θ_y was found to be 8.56×10^{-3} m^2s^{-2} and 9.02×10^{-3} m^2s^{-2} respectively resulting in an average θ of 8.79×10^{-3} m^2s^{-2}. This granular temperature is more than one order of magnitude higher than that for disc impeller experiments. This should be expected due to low velocities or slow dynamics in experiments with the disc impeller. θ_s from Eq. 2.12 can be written as:

$$\theta_s = m_s \theta \tag{2.12}$$

To calculate m_n in above equation, the $\bar{d}_{(4,3)}$ [#] mean granule size at each sampling time was used. The density for the granule was approximated to 2500 kg/m^3 from the individual densities and ratio (13% l/s ratio) of Durcal 40 and PEG-6000. θ_s was calculated to be in the range 1.7×10^{-9} to 5.8×10^{-9} kg m^2 s^{-2} depending on the values of average θ and mean granule size. The values of granule mean size and granular temperatures at different time intervals are summarised in Table 6.2.

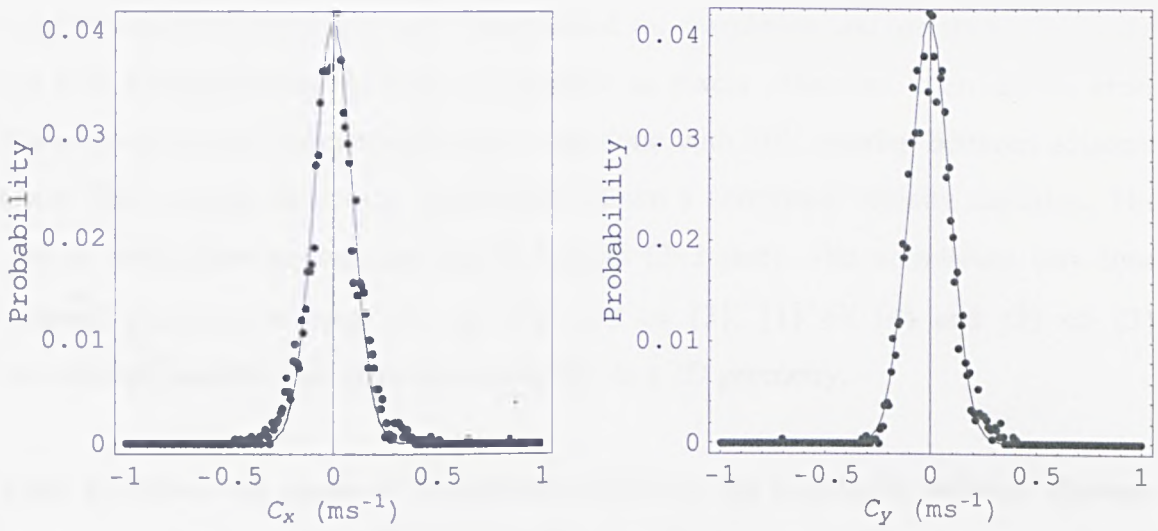

(i) (ii)

Figure 6.5: Gaussian distribution of velocity fluctuation in (i) C_x, and (ii) C_y at 1 min granulation time.

The values of granular temperatures also have to be verified for their authenticity. This can be done similar to as in section 5.4.2 for disc impeller experiments by comparing variance in granular temperature with the error in PIV calculations in equivalent units. The velocity analysis was done with recursive MQD with 50% overlap and an interrogation window size of 8×8 pixels. As discussed in section 3.3.3.2, an error of 0.01 pixel in calculation is assumed. The size of a pixel was 2.5×10^{-4} m and time difference between consecutive images was 10^{-3} s resulting in an equivalent error of 6.25×10^{-6} m^{2}s^{-2}. This value is far too low than the average granular temperature value of 8.79×10^{-3} m^{2}s^{-2}, nearly 0.07%.

$\bar{d}_{(4,3)}$ is the size of the granule that has same ratio of volume to mass as the whole distribution.

6.4 CORRELATION ANALYSIS OF VELOCITIES

Correlation analysis is already introduced in a short introduction in section 5.6. Similar analysis is done in this section to evaluate the random behaviour of particle fluctuating motion irrespective of surroundings in experiments of high shear granulation with the 3-blade impeller. The residual velocities (C_x and C_y) calculated after fitting SG smoothing filter to temporal velocities at the single interrogation area are subjected to correlation analysis. The four alternate interrogation areas in the central region of the images captured during experiments were investigated for correlation and are shown in Figure 6.6 with corresponding reference coordinates in pixels. Alternate interrogation areas were chosen as the correlation analysis was done with 50% overlap between adjacent areas. This overlap obviously would have shown a correlated velocity variation. The size of each interrogation area was 8×8 pixel (2×2 mm). The correlation was done between interrogation areas {1} ⇔ {2}, {1} ⇔ {3}, {1} ⇔ {4} and {2} ⇔ {3} covering all possible directions on bed surface in a 2D geometry.

Table 6.1 shows the values of correlation coefficients for correlation between alternate interrogation areas shown in Figure 6.6. The correlation between C_x values varies in the range 8% to 17%. This is a little higher than the correlation seen for disc impeller. It should however be noted that a large part of these fluctuations is not correlated, which could be enough for assuming the particle motion to be random. On the contrary, the results for correlations between C_y values are not that encouraging showing correlation as high as 45%. There could be a couple of reasons for such a high correlation. It could be that the SG smoothing filter is not able to represent well the mean motion component in U_y. Also as the interrogation area size approaches the granule size there is higher probability of granules moving from one interrogation area to the adjacent area resulting in higher correlation between them. Otherwise it might mean that the fluctuations are actually correlated to such a higher extent. Assuming it to be highly correlated there still remains a major uncorrelated part, the influence of which needs to be debated. Having said that, the paradox of uncorrelated C_x and highly correlated C_y remains to be understood. More importantly it is seen that all the evidence discussed before suggest random fluctuations of particles except this single observation in C_y. Assuming the fluctuations to be random it would be possible to do further analysis of results to estimate collision efficiencies.

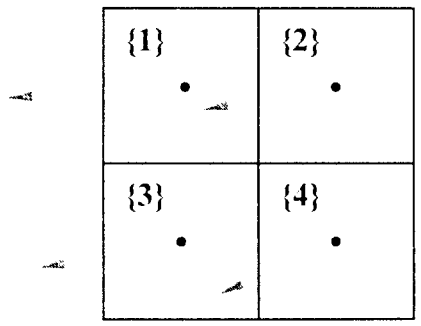

Reference point coordinates in pixels:
{1} = (119, 219)
{2} = (127, 219)
{3} = (119, 227)
{4} = (127, 227)

Figure 6.6: Depiction of velocity vectors at four adjacent non-overlapping interrogation areas at 1 min granulation time in an experiment with the 3-blade impeller.

Table 6.1: Correlation coefficient (Eq. 5.9) values for correlation between alternate interrogation areas {1}, {2}, {3} and {4} from Figure 6.6 for x and y velocity fluctuations.

Velocity component	Interrogation areas	{1}	{2}	{3}	{4}
C_x	{1}	1	-	-	-
	{2}	0.167	1	-	-
	{3}	0.075	0.165	1	-
	{4}	0.114	0.139	0.088	1
C_y	{1}	1	-	-	-
	{2}	0.449	1	-	-
	{3}	0.313	0.335	1	-
	{4}	0.404	0.354	0.289	1

6.5 EXTRACTION OF AGGREGATION RATES WITH DESCRITISED POPULATION BALANCE MODELLING (DPBM)

For this analysis, Eq. 2.10 is used for the size dependent aggregation rate constant (β^*). The time dependent aggregation rate constant, β_0, was found by minimising the overall sum of square errors between the experimentally measured granules size distribution and the discretised population balance model solution. This was basically solved in DPB package (version 6.0.4) written in *Mathematica* by Hounslow (2002). The simulation results are shown in appendix D. The GSD (number distribution) of the samples was done in a Camsizer® (Retsch Technology GmbH, Germany) with $\sqrt[3]{2}$

progression of sizes. Camsizer® works on the principle of processing images of uni-layered granular material captured with a pair of CCD cameras. The aggregation rate constant was converted into consistent basis ($m^{2.5}$ s^{-1}) units using a shape factor of $\pi/6$ (for sphere) and an assumed voidage of 0.5. The simulation of the binary aggregation population balance equation fitted to the mass weighted granule size distribution is shown in Figure 6.7. The simulation shows good qualitative fit with the minimum sum of square errors of 0.027. The fitted time dependent aggregation rate constant was found to be (in $m^{2.5}$ s^{-1}):

$$\beta_0 = 7.52\times10^{-13} - 5.56\times10^{-16} t \tag{6.1}$$

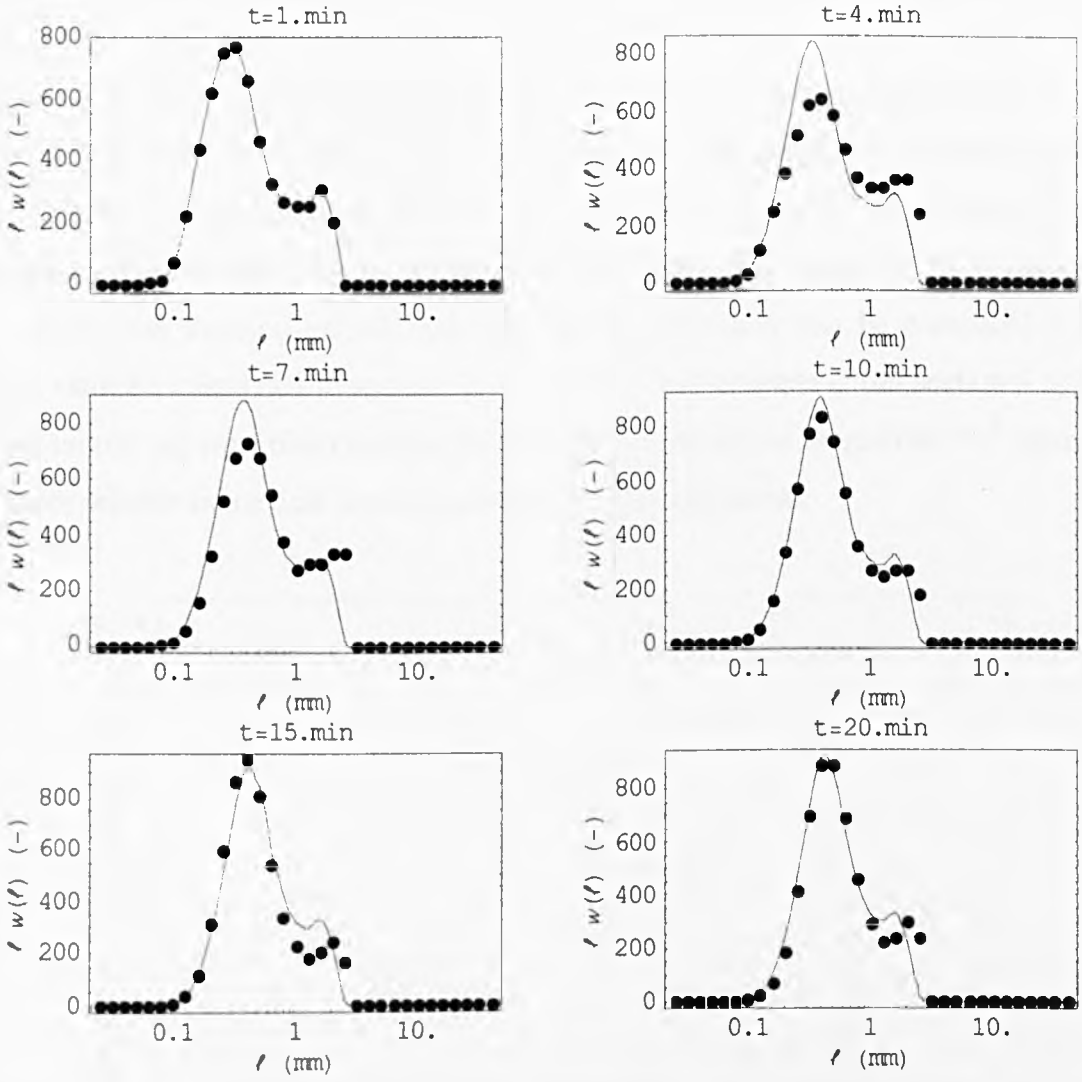

Figure 6.7: Mass weighted granule size distributions for the experimentally measured samples (•) and the solution of the binary aggregation population balance equation (–) using the time dependent aggregation rate constant given in Equation 6.1.

6.6 ESTIMATION OF AGGREGATION EFFICIENCY

To estimate the aggregation efficiencies Eq. 2.13 can be rearranged as:

$$\psi = \frac{\beta_0}{g_{i,j}\sqrt{3\theta_S/\rho}} \tag{6.2}$$

Same value of g_0 (=12.98) was used as calculated from Eq. 5.6 in chapter 5 for disc impeller experiment. Aggregation efficiency was calculated for the six sample times during the granulation experiment using Eq. 6.2 and values of mixture granular temperature (calculated with average granule size). As discussed earlier in section 2.4.2, the aggregation efficiencies depend on the granule size, utilising granule size for calculating the aggregation efficiency emphasizes this fact. Figure 6.8 shows how the aggregation efficiency changed with granulation time. It shows relatively high aggregation efficiency short time after binder addition (1 minute), approximately 4 in a 100 million collisions result in successful aggregation. However, the efficiency quickly approximately halves from about 3.84×10^{-8} to about 1.82×10^{-8} by 4 minutes after binder addition. The aggregation efficiency then continues to steadily reduce during the 20 minute wet massing period. This aggregation efficiency can be compared to the rough estimate calculated in section 5.5 of 2×10^{-7}. This estimate (from section 5.5) was based on two separate observations. So the current estimate of magnitude 10^{-8} seems to be more reliable as the data is sourced from a single experiment.

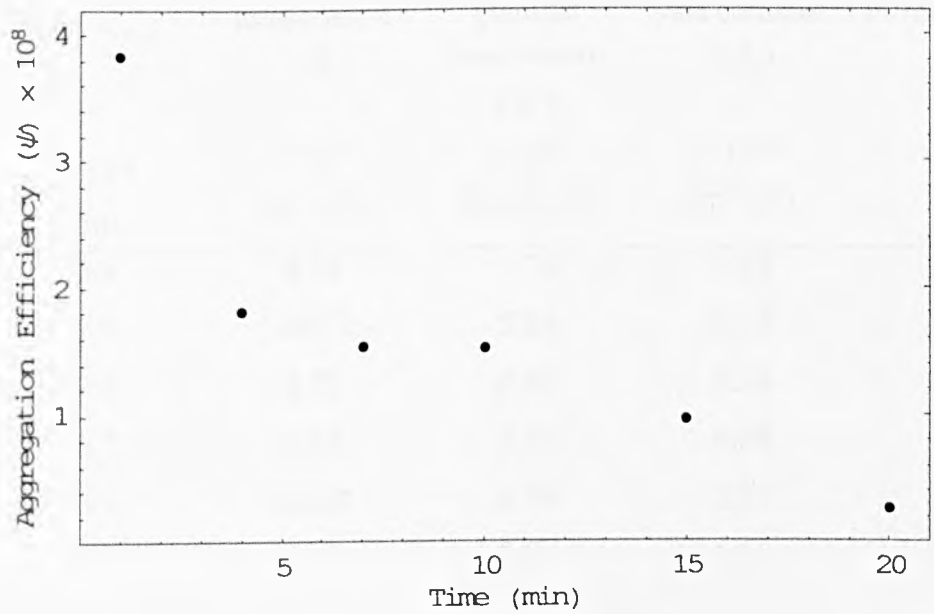

Figure 6.8: Aggregation efficiency ($\psi \times 10^8$) as a function of time for wet granulation of Durcal 40 and PEG-4000.

The change of the aggregation efficiency during granulation (Figure 6.8) can be conceptually described as follows from the perspective of granule composition and impact velocities. Soon after addition of the binder, the aggregation efficiency is relatively high. There is plenty of surface liquid available for granules to be 'sticky' enough to aggregate. Additionally the average granule size is relatively low suggesting that impact momentum will be relatively low and hence impacting particles will be more likely to be captured than rebound. As granulation progresses, the granule surface become less wet due to collecting drier smaller primary particles or granules. As a consequence of repeated impacts granules become denser and internal liquid tends to be squeezed back to the granule surface. This mechanism is often described as consolidation (Ennis et al., 1997). The liquid on the surface allows the granules to aggregate, but at an overall reduced rate compared to the initial binder distribution period, due to the internal binder transport within the granules. Additionally with increasing granulation time the granules become denser and larger, suggesting that impact momentum will increase and the chance of granules rebounding after impact will increase, leading to a net reduction in the observed aggregation efficiency.

Table 6.2: Summary of values of granular temperatures, mean particle sizes, aggregation rates, and aggregation efficiencies in a wet granulation experiment of Durcal 40 and PEG-4000.

Time	Granule mean size, $\bar{d}_{(4,3)}$	Granular temperature (θ)	Mixture granular temperature (θ_S)	Aggregation rate constant (β_0)	Aggregation efficiency (ψ)
(min)	$\times 10^{-4}$ (m)	$\times 10^{-3}$ ($m^2 s^{-2}$)	$\times 10^{-9}$ ($kg\ m^2 s^{-2}$)	$\times 10^{-13}$ ($m^{2.5} s^{-1}$)	$\times 10^{-8}$
1	5.3	8.79	1.74	7.19	3.84
4	7.5	10.57	5.73	6.19	1.82
7	7.6	9.72	5.65	5.18	1.53
10	6.7	9.52	3.73	4.18	1.52
15	6.3	10.28	3.39	2.51	0.96
20	7.2	10.10	5.00	0.85	0.27

As the calculations made above for the aggregation efficiencies depended on the assumption of solid volume fraction to be 0.5. However this does not depict the real situation in a high shear mixer. So a sensitivity analysis is necessary that will consider solid volume fractions (ε_m) in the range of 0.05 to 0.6. The calculations of this analysis are shown in Table 6.3. The values show aggregation efficiency to be as high as 3 in 10 million at ε_m = 0.05 and 1 min of granulation time to a low of less than 1 in a billion at ε_m = 0.6 and 20 min of granulation time. That is the aggregation efficiency has a inverse relationship to the solid volume fraction in a high shear mixer. The higher the solid volume fraction, the higher are the chances of successful granule aggregation.

Table 6.3: Sensitivity analysis of changing solid volume fraction on aggregation efficiencies in a wet granulation experiment of Durcal 40 and PEG-4000.

Time	Aggregation efficiency (ψ) at ε_m = 0.05 $\times 10^{-7}$	Aggregation efficiency (ψ) at ε_m = 0.6 $\times 10^{-9}$
1	2.84571	9.576
4	1.34812	4.5365
7	1.13842	3.83085
10	1.12962	3.80123
15	0.712562	2.39782
20	0.197349	0.664093

Observations of the granular surface velocities provide reasonable indication that the particle velocities can be described using KTGF, and hence that the EKK is more reliable physically based size dependent aggregation kernel compared to SSK. Combining this with calculated granular temperature (or indeed estimates from continuum or discrete numerical models) allows collision frequencies to be calculated. This only leaves a suitable model for the aggregation efficiency to be found in order to build a predictive high shear granulation model. One would also expect that a suitable model for 'effective' granular temperature would be needed as it is expected to change depending on the state of bed flow. It should be expected that aggregation efficiency will depend on the granule properties (e.g. the amount of binder available, the granule size etc.) and perhaps the impact velocity (again, impact velocity can be estimated from granular temperature: Goldschmidt et al., 2002).

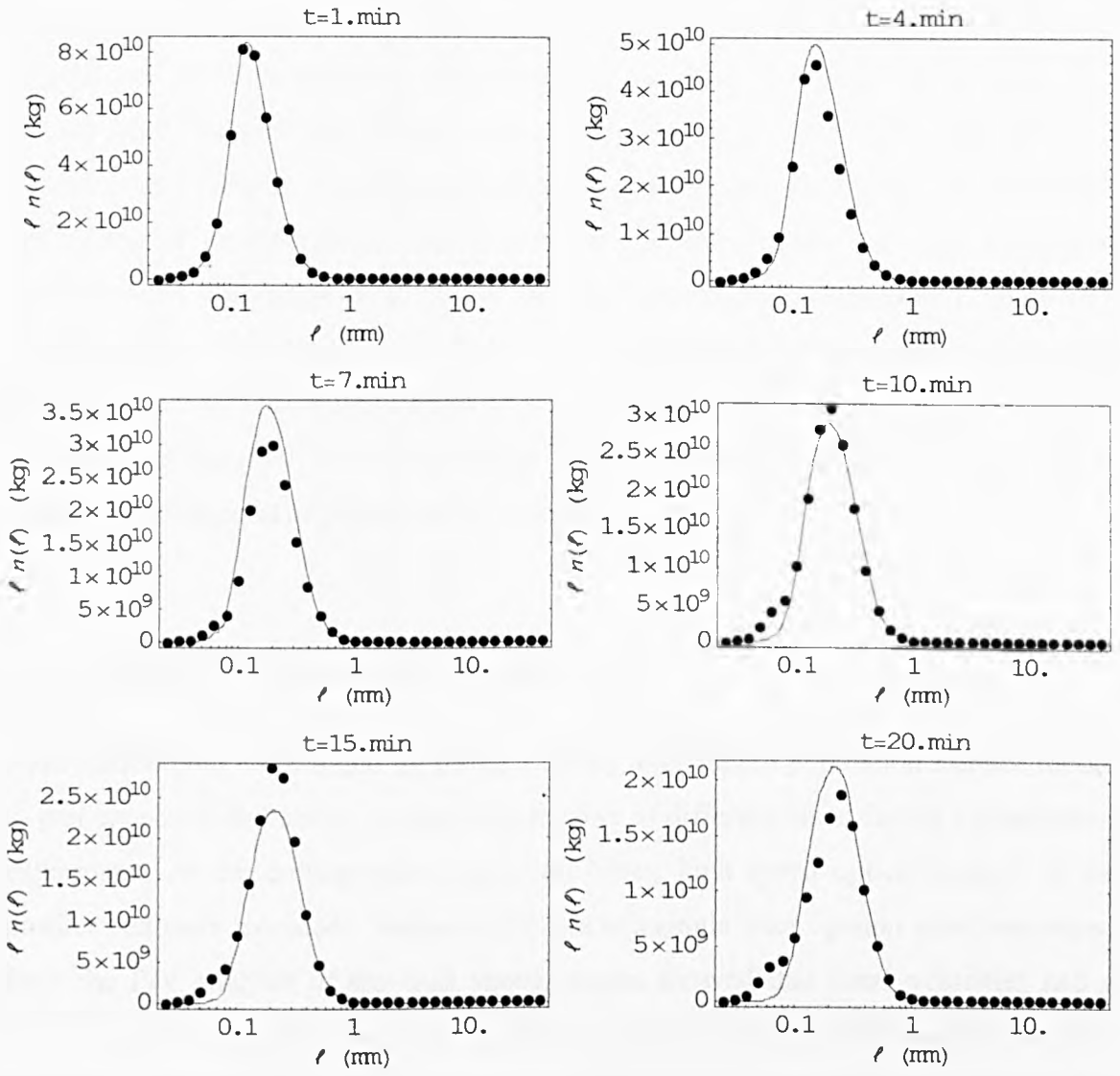

Figure 6.9: Number weighted granule size distributions for the experimentally measured samples (•) and the solution of the binary aggregation population balance equation (–) using the time dependent aggregation rate constant given in Equation (6.1).

Some discussion should also be made on some of the limitations of this analysis. This analysis is based on the velocity field at the bed surface. Although two orthogonal components of velocity have been taken into account, the third dimension is not considered. Additionally the flow behaviour within the bulk flow could be different to that exhibited on the surface, which emphasizes on the need for high resolution 3D investigation of the flow. Additionally this analysis does not take into account breakage rate processes. Figure 6.9 shows the number weighted granule size distributions. Despite a general increase in granule size, a noticeable small shoulder of material at about 50 μm appears after about 10 minutes. This is clearly evidence of an attrition/breakage process during granulation. As this breakage is not taken into account

in the population balance model used in this paper, it can be expected that the fitted aggregation rate constant is underestimating the true underlying aggregation rate. This in turn would suggest that the aggregation efficiency is possibly underestimated to a certain extent. Despite this, it appears that the aggregation only model is a reasonable description of the overall high shear granulation, and certainly this small extent of attrition is not observable on the mass weighted granule size distribution (Figure 6.7). Finally, only a single value of efficiency at each time has been used, whereas the efficiency is also expected to depend on size and other granule properties. In this sense the efficiency reported here is an average value and, as is explained above, should be expected to change as average granule properties change.

6.7 SUMMARY AND CONCLUSION

Aggregation rates were found by fitting a binary aggregation population balance model to granule size distributions sampled at a number of different times during a granulation experiment. At the corresponding sampling times, high speed optical images of the powder bed were recorded. Surface velocities at a single interrogation area determined from the PIV analysis of the high speed images showed that these velocities had a systematic and a random component, with the random component exhibiting a Gaussian frequency distribution. It was found that the KTGF allowed estimation of the collision frequency of the granules from the powder velocities. By comparing the fitted aggregation rate constant with the collision frequencies, an estimate of aggregation efficiency was made. Aggregation efficiency was found to be initially high after binder addition, but decreased as the granulation proceeded. This appears consistent with a conceptual description of the binder nucleation and wetting and consolidation processes of granulation. This analysis provides a platform from which a predictive high shear granulation model can be built by separating the contributions of granule motion and composition to the overall change in the granule size distribution.

7

CONCLUSION

7.1 THESIS CONCLUSION

A novel technique was developed by combining optical high speed imaging and particle image velocimetry. With this technique it is possible to interrogate surface velocities at high resolution spatially and temporally. The highest temporal resolution achieved in this thesis is 1125 velocity data points per second and the highest spatial resolution is reported as 2 × 2 mm (8×8 pixels). Investigation of mean motion in a high shear mixer using this PIV technique resulted in a high resolution understanding of the nature of the surface flow. This technique also helped in extracting velocities from a single interrogation area, the size of which was comparable to the granule size in the experimental batches.

The flow behaviour was found to be highly dependent on the structure and position of the impeller blade. In case of the 3-blade impeller, it was seen that individual blades impart different momentum to the granular bed due to different angles of the flights attached to each blade. It was also seen that variability in short duration of time intervals compared to time for a single blade pass in high at higher impeller speeds. Effect of operating conditions and feed material properties on the variation in bed velocity was investigated. For experiments with dry granules the bed velocity increased with increasing impeller speed, but the normalised velocity was found to decrease with impeller speed. The higher viscosity binder slowed down the bed and the bed showed sluggish response to the momentum imparted by each impeller blade when compared to low viscosity binder. The smaller granule range batch showed slightly lower velocities

compared to bigger size granules. This was explained as the loss of momentum in more number of collisions as the number density of smaller granules is high in the same weight batch and due to trajectory segregation. Velocities in wet granulation experiment at different time intervals varied as a function of the mean granule size and the availability of binder on the granule surface. Earlier on the velocities were low due to free binder and small mean granule size but then the velocities steadied as the granules consolidated and assumed a uniform mean size. The reproducibility for dry granules was very good. But it was also commented that reproducibility may not be as good for wet granulation due to batch-to-batch variations in operation.

For the disc impeller the flow was rather simple. This provided the basis to calculate velocity fluctuations from which the particle collision frequency based on EKK was estimated. The collision frequency based on SSK was also calculated by calculating shear rate from a polynomial fit to average velocities along radius. This also proved the point that PIV studies are useful in finding instantaneous shear fields. The collision frequency due to EKK was found to be three orders of magnitude higher than that due to SSK. It was also experienced that the disc impeller was unsuitable for wet granulation experiments due to the shortcomings in the design. Due to this the focus was shifted back to wet granulation with the 3-blade impeller.

In the wet granulation experiments with the 3-blade impeller, bed images were recorded simultaneously with granule sample collection. From the bed images velocities were calculated using 'mpiv' and velocities at a single interrogation area were binned. A Savitzky-Golay smoothing filter was fitted to the velocity at this single interrogation area and velocity fluctuations at that point were calculated. The probability distribution of fluctuations in velocity was found to exhibit a Gaussian behaviour supporting the theory of random motion of particles provided the velocities represented underlying particle velocities. Granular temperature was extracted from the Gaussian fit from which the EKK based particle collision frequency was calculated. The PBM from the GSD of the samples provided the time dependent aggregation rate from the wet granulation experiment. From the knowledge of collision frequency and aggregation rate, aggregation efficiency was estimated. The aggregation efficiency was found to be of the order of 4 in 100 million in the initial stages but quickly dropped as the granulation proceeded. The aggregation efficiency was also estimated to vary in the

range of 3 in 10 million at $\varepsilon_m = 0.05$ and 1 min of granulation time to a low of less than 1 in a billion at $\varepsilon_m = 0.6$ and 20 min of granulation time. Although the x-component of velocity fluctuations showed low correlation between alternate interrogation areas, the y-component showed high correlation weakening the assumption of random motion of particles. It was suggested that the Savitzky-Golay smoothing filter might be unable to depict the mean flow hidden in the velocity at the single interrogation area and a better analysis would be useful.

7.2 RECOMMENDATIONS FOR FUTURE WORK

1. Velocity calculation through PIV

It is possible that some error might be introduced due to low resolution of the individual granule images. At higher image resolution of the granules the individual granule displacement will be pronounced. However taking into consideration the resolution of the high speed camera, it can be recommended that the camera does not need to be focused on the entire granular bed and instead only be focused on a small size physical window that would rather look at less number of particles at high resolution. Although this will give better estimation of particle velocities, it would be difficult to look simultaneously at the entire bed.

In the current analysis, consecutive images approximately 0.001 s apart in time were interrogated for velocity calculation in PIV software. It would be interesting to interrogate images with different time lag in the same sequence of images to look at variation in velocity calculation.

2. Population balance modelling

The population balance modelling (PBM) here was 1-dimensional and only took into consideration the binary aggregation phenomena. It would be recommended that a 2-dimensional PBM can be done with simultaneous measurement of binder size distribution (the amount of binder in the different sized granules) in the collected samples along the experiment. Also breakage phenomena can be incorporated into the population balance equation. This would provide a better estimate of aggregation rate constant.

3. 3D investigation

One of the shortcomings of the optical PIV investigation is that only surface velocities can be estimated. It can not interrogate velocities beneath the surface. It can be recommended that for a future work a combination of techniques can be employed to investigate the flow inside a granulator. The nearest competitor of PIV is Positron Emission Particle Tracking (PEPT) that can track tracer particles inside the bulk material. The shortcomings of one technique are the strong points of other and so these can complement each other well.

4. Disc impeller experiments

The disc impeller was found to provide a very smooth flow independent of the structure of the impeller that made extracting the fluctuating particle velocity simple. However it was found to be unsuitable for wet granulation experiment. Wet granulation experiments can be carried out in industrial built high shear mixer with a disc impeller suitable for wet granulation. Similar treatment can be done on this experiment as in chapter 5 combined with PBM as in chapter 6.

NOMENCLATURE

The units are indicative. Any variation in the text is notified then and there.

Roman symbols

A	area flux of powder traversing the spray zone, m^2s^{-1}.
c	velocity at a single interrogation area, $m.s^{-1}$.
C	random fluctuating velocity, $m.s^{-1}$.
Cor	cross-correlation function
D	mixer diameter, m
$\overline{d}_{(4,3)}$	mean granule size, m
d_d	droplet diameter, m
f	blade frequency, Hz
g_0	average radial distribution function
h	fill height, m
l_i, l_j	linear dimensions of a particle, m
m_n	mass of a particle, kg
N	number concentration of particles, m^{-3}
r	particle position from the centre of the rotor, m
R	stator radius or mixer radius, m
St_{def}	Stoke's deformation number
t	time, s
v	local mean velocity, $m\ s^{-1}$
v_c	collision velocity, $m\ s^{-1}$
v_θ	circumferential component of particle velocity, $m\ s^{-1}$
v_r	radial component of particle velocity, $m\ s^{-1}$
V	bed speed/velocity, $m\ s^{-1}$
V_x	x-component of bed velocity, $m\ s^{-1}$
V_y	y-component of bed velocity, $m\ s^{-1}$
$\dot{V}$	volumetric spray rate, $m^3\ s^{-1}$
W	width of spray zone

Greek symbols

Ψ_a	dimensionless spray flux
θ	granular temperature, m^2s^{-2}
θ_S	mixture granular temperature, kg m^2 s^{-2}
β	aggregation rate,
β_0	time dependent aggregation rate,
ψ	aggregation efficiency
ρ	density, kg m^{-3}
$\dot{\gamma}$	shear rate, s^{-1}
ω	angular speed of rotation, rad s^{-1}
ϕ	angle of impeller position, (°)
η	viscosity, mPa s (cP)
ε_S	solid volume fraction
ε_m	maximum solid volume fraction
σ_r	tensile strength of a granule, Pa
σ_f	fracture strength of a granule, Pa
σ	Standard deviation

Acronyms

1 D	One Dimensional
2 D	Two Dimensional
3 D	Three Dimensional
CCD	Charge-Coupled Device
COR	Cross-correlation
DEM	Discrete Element Modelling
DFT	Discrete Fourier Transform
DPB	Descritised Population Balance
EKK	Equi-partition of Kinetic energy Kernel
EPSRC	Educational and Physical Sciences Research Council
EIP	Engineering Instrument Pool
fps	Frames per second
GSD	Granule Size Distribution

HSC	High Speed Camera
HSI	High Speed Imaging
HSG	High Shear Granulation
HSM	High Shear Mixer
KTGF	Kinetic Theory of Granular Flow
l/s	Liquid to solid ratio by mass
MQD	Minimum Quadric Differences
PBM	Population Balance Modelling
PEG	Poly-Ethylene Glycol
PEPT	Positron Emission Particle Tracking
PSD	Particle Size Distribution
RMS	Room Mean Square
rpm	Revolutions per minute
SGD	Savitzky-Golay Derivative
SSK	Smoluchowski Shear Kernel
USP	United States Pharmacopeia

REFERENCES

Adrian R.J., 2005. Twenty years of particle image velocimetry. *Experiments in Fluids*. 39, 159–169.

Bardin M., P.C. Knight, J.P.K. Seville, 2004. On control of particle size distribution in granulation using high-shear mixers. *Powder Technology* 140, 169–175.

Biggs C.A., C.F.W. Sanders, A.C. Scott, A.W. Willemse, A.C. Hoffmann, T. Instone, A.D. Salman and M.J. Hounslow, 2003. Coupling granule properties and granulation rates in high-shear granulation. *Powder Technology* 130, 162–168.

Björna I.N., Anders Janssonb, Magnus Karlssona, Staffan Folestada, Anders Rasmusonb, 2005. Empirical to mechanistic modelling in high shear granulation. *Chemical Engineering Science* 60, 3795–3803.

Bouwman A.M., Marinella R. Visser, Anko C. Eissens, Johannes A. Wesselingh, Henderik W. Frijlink, 2004. The effect of vessel material on granules produced in a high-shear mixer. *European Journal of Pharmaceutical Sciences* 23, 169–179.

Bridgwater J., S. Forrest and D.J. Parker, 2004. PEPT for agglomeration? *Powder Technology* 140, 187–193.

Broadbent C.J., J. Bridgwater, D.J. Parker, S.T. Keningley, P. Knight, 1993. A Phenomenological Study of a Batch Mixer Using a Positron Camera. *Powder Technology*, 76, 317–329.

Chapman S., T.G. Cowling, 1970. *The Mathematical Theory of Non-Uniform Gases*, 3rd edition, Cambridge Uni. Press.

Conway S.L., A. Lekhal, J.G. Khinast, B.J. Glasser, 2005. Granular flow and segregation in a four-bladed mixer. *Chemical Engineering Science* 60, 7091–7107.

Cundall P.A., O.D.L. Stack, 1979. A discrete numerical model for granular assemblies. *Geotechnique* 29, 47–65.

Darelius A., Rasmuson A., Niklasson-Björn I., Folestad S., 2005. High shear wet granulation modelling—a mechanistic approach using population balances. *Powder Technology* 160, 209–218.

Devore J., R. Peck, 1994. *Introductory Statistics*, second edition, West publishing company, New York, USA.

Edwards M.F., T. Instone, 2001. Particulate products – their manufacture and use. *Powder Technology* 119, 9–13.

Ennis B.J., 1991. A microlevel-based characterization of granulation phenomena. *Powder Technology* 65, 257–272.

Ennis B.J., 1996. Agglomeration and size enlargement session summary paper. *Powder Technology* 88, 203–225.

Ennis B.J. and J.D. Litster, 1997. Particle size enlargement, in: R. Perry and D. Green (Editors), *Perry's Chemical Engineers' Handbook* (7th ed.), McGraw-Hill, New York, 20-56 – 20-89.

EPSRC - Engineering Instrument Pool (EIP), 2006. http://www.eip.rl.ac.uk/

Forrest S., J. Bridgwater, P.R. Mort, J. Litster, D.J. Parker, 2003. Flow pattern in granulating systems. *Powder Technology* 130 (1–3), 91–96.

Fu J.S., Y.S. Cheong, G.K. Reynolds, M.J. Adams, A.D. Salman, M.J. Hounslow, 2004a. An experimental study of the variability in the properties and quality of wet granules. *Powder Technology* 140, 209–216.

Fu J.S., M.J. Adams, G.K. Reynolds, A.D. Salman, M.J. Hounslow, 2004b. Impact deformation and rebound of wet granules. *Powder Technology* 140, 248–257.

Gidaspow D., 1994. Multiphase Flow and Fluidization – Continuum and Kinetic Theory Descriptions. *Academic Press Limited*, London, UK.

Gidaspow D., L. Huilin, 1998. Equation of state and radial distribution functions of FCC particles in a CFB. *AIChE Journal* 44, 279–293.

Goldschmidt M.J.V., 2001. *Hydrodynamic Modelling of Fluidised Bed Spray Granulation*. Ph.D. thesis, Twente University Press, Netherlands.

Goldschmidt M.J.V., R. Beetstra, J.A.M. Kuipers, 2002. Hydrodynamic modelling of dense gas-fluidised beds: comparison of the kinetic theory of granular flow with 3D hard-sphere discrete particle simulations. *Chemical Engineering Science* 57, 2059–2075.

Hapgood, K.P., 2000. *Nucleation and binder dispersion in wet granulation*. PhD thesis, Department of Chemical Engineering, University of Queensland, Australia.

Holm P., M. Bonde, T. Wigmore, 1996. Pelletisation by granulation in a roto-processor RP-2. Part I: Effects of process and products variables on granule growth. *Pharm. Tech. Eur.* 8, 22–36.

Hoornaert F., P.A.L. Wauters, G.M.H. Meesters, S.E. Pratsinis, B. Scarlett, 1998. Agglomeration behaviour of powders in Lodige mixer granulator. *Powder Technology* 96 (2), 116–128.

Hounslow, M.J., R.L. Ryall, V.R. Marshall, 1988. A discretised population balance for nucleation, growth and aggregation. *AIChE Journal* 34, 1821–1832.

Hounslow M.J., 1998. The population balance as a tool for understanding particle rate processes. *Kona Powder and Particle*, 16, 179–193.

Hounslow M.J., J.M.K. Pearson, T. Instone, 2001. Tracer studies of high-shear granulation: II. Experimental results. *AIChE Journal* 47, 1984–1999.

Hounslow, M.J., 2002. Descritised Population Balance (DPB) package in *Mathematica® 5* (Wolfram Research Inc.). Particle Products Group, Department of Chemical and Process Engineering, The University of Sheffield, U.K.

Hounslow, M.J., 2005. *Particle Rate Processes, 1st hadout edition.* Particle Products Group, Department of Chemical and Process Engineering, The University of Sheffield, U.K.

Iveson S.M., J.D. Litster, 1998a. Growth regime map for liquid-bound granules. *AIChE Journal* 44, 1510–1518.

Iveson S.M., J.D. Litster, 1998b. Liquid-bound granule impact deformation and coefficient of restitution. *Powder Technology* 99, 234–242.

Iveson S.M., 2001a. Granule coalescence modelling: including the effects of bond strengthening and distributed impact separation forces. *Chemical Engineering Science* 56, 2215–2220.

Iveson S.M., J.D. Litster, K. Hapgood, B.J. Ennis, 2001b. Nucleation, growth and breakage phenomena in agitated wet granulation processes: a review. *Powder Technology* 117(1–2), 3–39.

Iveson S. M., P.A.L. Wauters, S. Forrest, J.D. Litster, G.M.H. Meesters and B. Scarlett, 2001c. Growth regime map for liquid-bound granules: further development and experimental validation. *Powder Technology* 117(1–2), 83–97.

Iveson Simon M., Neil W. Page, Jim D. Litster, 2003. The importance of wet-powder dynamic mechanical properties in understanding granulation. *Powder Technology* 130, 97– 101.

Johansen, A. and T. Schaefer, 2001. Effects of interactions between powder particle size and binder viscosity on agglomerate growth mechanisms in a high shear mixer. *European Journal of Pharmaceutical Sciences* 12, 297–309.

Kendall K., 1988. Agglomerate strength. *Powder Metallurgy* 31, 28–31.

Knight, P.C., 1993. An investigation of the kinetics of granulation using a high shear mixer. *Powder Technology* 77, 159–169.

Knight P.C., T. Instone, J.M.K. Pearson, M.J. Hounslow, 1998. An investigation into the kinetics of liquid distribution and growth in high shear mixer agglomeration. *Powder Technology* 97(3), 246–257.

Knight, P.C., A. Johansen, H.G. Kristensen, T. Schaefer, and J.P.K. Seville, 2000. An investigation of the effects on agglomeration of changing the speed of a mechanical mixer. *Powder Technology* 110, 204–209.

Knight P.C., J.P.K. Seville, A.B. Wellm, T. Instone, 2001a. Prediction of impeller torque in high shear powder mixer. *Chemical Engineering Science* 56, 4457–4471.

Knight P.C., 2001b. Structuring agglomerated products for improved performance. *Powder Technology* 119, 14–25.

Knight Peter, 2004. Challenges in granulation technology. *Powder Technology* 140, 156–162.

Kristensen H.G., P. Holm, T. Schæfer, 1985. Mechanical properties of moist agglomerates in relation to granulation mechanisms Part II. Effects of particle size distribution. *Powder Technology* 44, 239–247.

Kristensen H.G., 1996. Particle agglomeration in high shear mixers. *Powder Technology* 88(3), 197–202.

Kuo H.P., P.C. Knight, D.J. Parker, M.J. Adams, J.P.K. Seville, 2004. Discrete element simulations of a high-shear mixer. *Advanced Powder Technology* 15 (3), 297–309.

Laurent B.F.C., J. Bridgwater, D.J. Parker, 2000. Motion in a particle bed agitated by a single blade. *AIChE Journal* 46 (9), 1723–1734.

Litster J.D., K.P. Hapgood, J.N. Michaels, A. Sims, M. Roberts, S.K. Kameneni, T. Hsu, 2001. Liquid distribution in wet granulation: dimensionless spray flux. *Powder Technology*, 114, 32–39.

Litster J.D., K.P. Hapgood, J.N. Michaels, A. Sims, M. Roberts, S.K. Kameneni, 2002. Scale-up of mixer granulators for effective liquid distribution. *Powder Technology* 124 (3), 272–280.

Litster J., B. Ennis, 2004. *The science and engineering of granulation processes.* Kluwer Academic Publishers, London, UK.

Moore D.S., G.P. McCabe, 1999. *Introduction to the practice of statistics.* Third edition, W. H. Freeman and Company, New York, USA.

Mori N. and K-A.Chang, 2003. Introduction to MPIV - User reference manual: http://sauron.urban.eng.osaka-cu.ac.jp/~mori/softwares/mpiv/index.php

Muguruma Y., T. Tanaka, Y. Tsuji, 2000. Numerical simulation of particulate flow with liquid bridge between particles (simulation of centrifugal tumbling granulator). *Powder Technology* 109 (1–3), 49–57.

Ogawa S., A. Umemura, N. Oshima, 1980. On the equation of fully fluidized granular materials. *Z. angew. Math. Phys.* 31, 483–493.

Parker D.J., C.J. Broadbent, P. Fowles, M.R. Hawkesworth, P. McNeil, 1993. Positron emission particle tracking – a technique for studying flow within engineering equipment. *Nuclear Instruments & Methods in Physics Research A*, 326, 592–607.

Parker D.J., R.N. Forster, P. Fowles, P.S. Takhar, 2002. Positron emission particle tracking using the new Birmingham positron camera. *Nuclear Instruments and Methods in Physics Research A*, 477, 540–545.

Pearson J.M.K., M.J. Hounslow, T. Instone, 2001. Tracer studies of high-shear granulation: I. Experimental Results. *AIChE Journal* 47, 1984–1999.

Plank R., B. Diehl, H. Grinstead, J. Zega, 2003. Quantifying liquid coverage and powder flux in high-shear granulators. *Powder Technology* 134, 223–234.

Press W. H., Brian P. Flannery, Saul A. Teukolsky, William T. Vetterling, 1986. *Numerical Recipes: The Art of Scientic Computing.* Cambridge University Press, Cambridge, UK.

Press W. H., Brian P. Flannery, Saul A. Teukolsky, William T. Vetterling, 1992. *Numerical Recipes in C: The Art of Scientific Computing*. Cambridge University Press, Cambridge, UK.

Ramaker J.S., M. Albada Jelgersma, P. Vonk, N.W.F. Kossen, 1998. Scale down of a high-shear pelletisation process: flow profile and growth kinetics. *International Journal of Pharmaceutics* 166 (1), 89–97.

Ramaker J.S., 2001. Fundamentals of high-shear pelletisation process. Ph.D. thesis, Rijksuniversiteit Groningen, Netherlands.

Ramakrishna D., 2000. *Population Balances: Theory and Applications to Particulate Systems in Engineering*. Academic Press, CA, USA.

Reynolds G.K, C.A. Biggs, A.D. Salman, M.J. Hounslow, 2004. Non-uniformity of binder distribution in high-shear granulation. *Powder Technology* 140, 203–208.

Reynolds G.K, J.S. Fu, Y.S. Cheong, M.J. Hounslow, A.D. Salman, 2005. Breakage in granulation: a review. *Chemical Engineering Science* 60, 3969–3992.

Rhodes Martin, 1999. *Introduction to Particle Technology*. John Wiley & Sons, England.

Rumpf H., 1962. *The strength of granules and agglomerates*. In: Knepper, W. (Ed.), Agglomeration. AIME, Interscience, New York, pp. 379–418.

Russell P., B. Diehl, H. Grinstead, J. Zega, 2003. Quantifying liquid coverage and powder flux in high-shear granulators. *Powder Technology* 134, 223–234.

Sanders C.F.W., A. Willemse, A.D. Salman and M.J. Hounslow, 2003. Development of a predictive high-shear granulation model. *Powder Technology* 138, 18–24.

Sastry K.V.S., 1975. Similarity size distribution of agglomerates during their growth by coalescence in granulation or green pelletization. *International Journal of Mineral Processing* 2, 187 – 203.

Schaefer T., P. Holm, H.G. Kristensen, 1986. Comparison between granule growth in a horizontal and a vertical high speed mixer: I. Granulation of dicalcium phosphate. *Arch. Pharm. Chem., Sci. Ed.* 14, 1–16.

Schaefer T., B. Taagegaard, L.J. Thomsen, H.G. Kristensen, 1993. Melt pelletization in a high shear mixer. IV. Effects of process variables in a laboratory scale mixer, *European Journal of Pharmaceutical Sciences* 1, 125–131.

Schaefer Torben, 1996. Melt pelletization in a high shear mixer VI: Agglomeration of a cohesive powder. *International Journal of Pharmaceutics* 132, 221–230.

Scott A.C., 2000a. Heterogeneity in high-shear granulation. PhD thesis, Clare College, Cambridge, UK.

Scott A.C., M.J. Hounslow and T. Instone, 2000b. Direct evidence of heterogeneity during high-shear granulation. *Powder Technology* 113, 205–213.

Smith J.O., 2003. *Mathematics of the Discrete Fourier Transform (DFT).* http://ccrma.stanford.edu/~jos/mdft/, ISBN 0-9745607-0-7.

Smoluchowski M., 1917. Mathematical theory of the kinetics of the coagulation of colloidal solutions. *Zeitschrift für Physikalische Chemie* 92, 129.

Stewart R.L., J. Bridgwater, D.J. Parker, 2001a. Granular flow over a flat-bladed stirrer. *Chemical Engineering Science* 56, 4257–4271.

Stewart R.L., J. Bridgewater, Y.C. Zhou, A.B. Yu, 2001b. Simulated and measured flow of granules in a bladed mixer – a detailed comparison. *Chemical Engineering Science* 56, 5457–5471.

Tan H.S., M.J.V. Goldschmidt, R. Boerefijn, M.J. Hounslow, A.D. Salman, J.A.M. Kuipers, 2004. Building population balance model for fluidized bed melt granulation: lessons from kinetic theory of granular flow. *Powder Technology* 142, 103–109.

Tardos G. I., M.I. Khan, P.R. Mort, 1997. Critical parameters and limiting conditions in binder granulation of fine powders. *Powder Technology* 94(3) 245–258.

Wellm A. B., 1997. *Investigation of a High Shear Mixer/Agglomerator.* Ph.D. thesis, the University of Birmingham, UK.

Willert C.E., M. Gharib, 1991. Digital particle image velocimetry. *Experiments in Fluids* 10, 181–193.

Williams J.C., 1990. Chapter 4: Mixing and segregation in powders, in: *Principles of Powder Technology*, ed. M.J. Rhodes, John Wiley & Sons, Chichester.

Zhou Y.C., B.D. Wright, R.Y. Yang, B.H. Xu, A.B. Yu, 1999. Rolling friction in the dynamic simulation of sandpile formation. *Physica A*, 269, 536–553.

Zhou Y.C., A.B. Yu, R.L. Stewart, J. Bridgwater, 2001. Microdynamic analysis of the particle flow in a cylindrical bladed mixer. *Chemical Engineering Science* 59, 1343–1364.

Appendix A:

MATLAB code to automate PIV processing

This program was originally written by Dr G. K. Reynolds, PPG, University of Sheffield.

pivprocess.m

```
function
pivprocess(fnamebase,ext,begin,foutnamebase,xsize,ysize,croprect,fps,pixperm,
rgbtrue,filter)

%fnamebase = pre number filename for input data
%ext = image extension (e.g. 'jpg' or 'tif')
%begin = first frame number (internal number)
%foutnamebase = output data prenumber filename (the number of the second
%image is appended to the filename)
%xsize = PIV x direction interrogation size
%ysize = PIV y direction interrogation size
%croprect = [xmin ymin width height] of cropping region
%fps = frames per second (/s)
%pixperm = pixels per metre in image
%rgbtrue = 0 for grayscale, 1 for rgb
%filter = 0 for no filtering, 1 for filtering (trying to remove NaN)

dt=1/fps;

addpath('C:\MATLAB_SV7\work\dace_toolbox');
addpath('C:\MATLAB_SV7\work\mpiv_toolbox');
warning off all;
%begin=0
finish=begin;

check=1;

while (check)
   finish=finish+1;
   if ((finish/10)<1)
      app='000';
   elseif ((finish/100)<1)
      app='00';
   elseif ((finish/1000)<1)
      app='0';
   elseif ((finish/10000)<1)
      app='';
   end
   fname=[fnamebase app int2str(finish) '.' ext];
```

```
   if (exist(fname)==0)
      check=0;
      finish=finish-1;
   end
end
finish

check=1;
i=begin;

if ((i/10)<1)
   app='000';
elseif ((i/100)<1)
   app='00';
elseif ((i/1000)<1)
   app='0';
elseif ((i/10000)<1)
    app='';
end
fname=[fnamebase app int2str(i) '.' ext]
B=imread(fname);
if (rgbtrue)
   B=rgb2gray(B);
end
B=imcrop(B,croprect);
%B=im2double(histeq(B));

while (check)
   i=i+1;
   if (i==finish)
      check=0;
   elseif (i>finish)
      error('error i>finish');
   end

   A=B;
   if ((i/10)<1)
      app='000';
   elseif ((i/100)<1)
      app='00';
   elseif ((i/1000)<1)
      app='0';
   elseif ((i/10000)<1)
      app='';
   end
   fname=[fnamebase app int2str(i) '.' ext]

   B=imread(fname);
   if (rgbtrue)
      B=rgb2gray(B);
   end
```

```
   B=imcrop(B,croprect);
   %B=im2double(histeq(B));

   [xi,yi,iu,iv]=mpiv(A,B,xsize,ysize,.5,.5,10,10,dt,'mqd',1,0);
   if (filter)
      [iu_f,iv_f,iu_i,iv_i]=mpiv_filter(iu,iv,2,2,3,0);
      iu=iu_i;
      iv=iv_i;
   end

   fname=[foutnamebase app int2str(i) '.txt']
   xi=xi/pixperm;
   yi=yi/pixperm;
   iu=iu/pixperm;
   iv=iv/pixperm;
   pivout(xi,yi,iu,iv,fname);

end

return
```

pivout.m

```
function pivout(xi,yi,iu,iv,fname)

fid = fopen(fname,'w');

for i=1:length(xi);
   for j=1:length(yi);
      if (isnan(iu(i,j)))
         iu(i,j)=0;
      end
      if (isnan(iv(i,j)))
         iv(i,j)=0;
      end
      fprintf(fid,'%e \t %e \t %e \t %e \n',xi(i),yi(length(yi)+1-j),iu(i,j),iv(i,j));
%       sprintf('%e \t %e \t %e \t %e \n',xi(i),yi(length(yi)+1-j),iu(i,j),iv(i,j))
   end
end

fclose(fid);

return
```

Appendix B:

C++ code to process vector array files

These programs were originally written by Dr G. K. Reynolds, PPG, University of Sheffield.

1. To calculate mean motion

```
// hsgvel - a program to calculate average velocities
// and granular temperature from PIV data
// written by Gavin Reynolds with Amol Nilpawar
// October 2003

#include <fstream.h>
#include <string.h>
#include <stdlib.h>
#include <stdio.h>
#include <math.h>

struct pivdata
{
        double ** xi;
        double ** vi;
};

int CountLinesofData( char *filename);
int MaxFiles(char *filename, int min);
void ReadData(pivdata & d, char * f, int n);
double Average(double * d, int n);
double GranTemp(double * d, int n, double av);

int main()
{
        pivdata avdata;
        pivdata data;
        double thetax;
        double thetay;
        char fname[100];
        char temp[100];
        int nlines;
        char *foutname="output.txt";
        ofstream fout(foutname,ios::out);
        int max,min=0;

        cout << "Enter filename prefix: ";
        cin >> fname;

        max=MaxFiles(fname,min);
```

```
cout << "Starting..." << "\n" << flush;

fout << "filename\taverageX\taverageY\tThetaX\tThetaY\tSumTheta\n";

for (int i=min;i<=max;i++)
{
        if(i<10)
                sprintf(temp,"%s00%i.dat",fname,i);
        else if (i<100)
                sprintf(temp,"%s0%i.dat",fname,i);
        else
                sprintf(temp,"%s%i.dat",fname,i);

        fout << temp << "\t";
        nlines=CountLinesofData(temp);

        data.xi = (double **) new double*[2];
        data.vi = (double **) new double*[2];
        avdata.xi = (double **) new double*[2];
        avdata.vi = (double **) new double*[2];
        for (int i=0;i<2;i++)
        {
                data.xi[i]=(double *) new double[nlines];
                data.vi[i]=(double *) new double[nlines];
                avdata.xi[i]=(double *) new double[1];
                avdata.vi[i]=(double *) new double[1];
        }

        ReadData(data,temp,nlines);

        for (i=0;i<2;i++)
        {
                avdata.xi[i][0]=Average(data.xi[i],nlines);
                avdata.vi[i][0]=Average(data.vi[i],nlines);
                fout << avdata.vi[i][0] << "\t";
        }

        thetax=GranTemp(data.vi[0],nlines,avdata.vi[0][0]);
        thetay=GranTemp(data.vi[1],nlines,avdata.vi[1][0]);

        fout << thetax << "\t" << thetay << "\t" << thetax+thetay << "\n";

        delete [] data.xi;
        delete [] data.vi;
        delete [] avdata.xi;
        delete [] avdata.vi;

        cout << "\t" << temp << "\n";
}
```

```
        fout.close();
        cout << "\nOutput written in " << foutname << "\n";
        return 0;
}


//function counts number of lines of data in a file
int CountLinesofData(char * filename)
{
        char c;
        int size=0;
        bool datainline = false;
        ifstream fin(filename,ios::in|ios::nocreate);
        if (!fin.is_open())
        {
                cout << "Error opening file\n" << flush;
                return -1;
        }
//count no. lines in file:
        while(fin.get(c))
        {
                switch(c)
                {
                case '\n':
                        if (datainline)
                                size++;
                        datainline = false;
                        break;
                default:
                        datainline = true;
                        break;
                }
        }
//if data in last line, but EOF instead of '\n' then increment size
        if (datainline)
                size++;
        fin.close();

//      cout << "Size of population: " << size << "\n" << flush;

        return size;
}

int MaxFiles(char *filename, int min)
{
        char temp[100];
        int max;
        bool exist=true;
        ifstream fin;

        max=min;
```

```
	do
	{
		if(max<10)
			sprintf(temp,"%s00%i.dat",filename,max);
		else if (max<100)
			sprintf(temp,"%s0%i.dat",filename,max);
		else
			sprintf(temp,"%s%i.dat",filename,max);
//		cout << temp << "\n";

		fin.open(temp,ios::in| ios::nocreate);
		if(fin.is_open())
		{
			max++;
			fin.close();
		}
		else
		{
			max--;
			exist=false;
		}
	} while (exist);

	return max;
}


void ReadData(pivdata & d, char * f, int n)
{
	ifstream fin;

	fin.open(f,ios::in|ios::nocreate);

	for (int i=0;i<n;i++)
	{
		fin >> d.xi[0][i] >> d.xi[1][i] >> d.vi[0][i] >> d.vi[1][i];
	}

	fin.close();
}

double Average(double * d, int n)
{
	double sum=0;

	for (int i=0;i<n;i++)
	{
		sum+=d[i];
	}
```

```
        return (double)sum/n;
}

double GranTemp(double * d, int n, double av)
{
        double sum=0;

        for (int i=0;i<n;i++)
        {
                sum+=pow((d[i]-av),2);
        }

        return (double)sum/n;
}
```

2. <u>To extract temporal varying velocities from a single interrogation point</u>

```
// hsgvel - a program to calculate average velocities
// and granular temperature from PIV data
// written by Gavin Reynolds with Amol Nilpawar
// October 2003

#include <fstream.h>
#include <string.h>
#include <stdlib.h>
#include <stdio.h>
#include <math.h>

struct pivdata
{
        double ** xi;
        double ** vi;
};

int CountLinesofData( char *filename);
int MaxFiles(char *filename, int min);
void ReadData(pivdata & d, char * f, int n);
double Average(double * d, int n);
double GranTemp(double * d, int n, double av);

double xcoord,ycoord;

int main()
{
        pivdata avdata;
        pivdata data;
        double thetax;
        double thetay;
```

```
char fname[100];
char temp[100];
int nlines;
char *foutname="output.txt";
char *foutav="average.txt";
ofstream fout(foutname,ios::out);
int max,min=2;
bool first=true;
double xmin,ymin,xmax,ymax;
int nx,ny;
pivdata averagedata;
int i,j;

cout << "Enter filename prefix: ";
cin >> fname;
cout << "\nEnter first file number: ";
cin >> min;
cout << "\n\nFor temporal velocity extraction, please enter x-coord: ";
cin >> xcoord;
cout << "\n and y-coord: ";
cin >> ycoord;

max=MaxFiles(fname,min);
cout << "\n" << max << "\n" << flush;

if (max==min)
{
        cout << "\nAborting.... no files to read....\n" << flush;
        exit(0);
}

cout << "Starting..." << "\n" << flush;

fout << "filename\taverageX\taverageY\tThetaX\tThetaY\tSumTheta\n";

for (i=min;i<=max;i++)
{
        if(i<10)
                sprintf(temp,"%s000%i.txt",fname,i);
        else if (i<100)
                sprintf(temp,"%s00%i.txt",fname,i);
        else if (i<1000)
                sprintf(temp,"%s0%i.txt",fname,i);
        else
                sprintf(temp,"%s%i.txt",fname,i);

        fout << temp << "\t";
        nlines=CountLinesofData(temp);

        data.xi = (double **) new double*[2];
        data.vi = (double **) new double*[2];
```

```
avdata.xi = (double **) new double*[2];
avdata.vi = (double **) new double*[2];
for (int i=0;i<2;i++)
{
        data.xi[i]=(double *) new double[nlines];
        data.vi[i]=(double *) new double[nlines];
        avdata.xi[i]=(double *) new double[1];
        avdata.vi[i]=(double *) new double[1];
}

ReadData(data,temp,nlines);

if (first)
{
        averagedata.xi=(double**) new double * [2];
        averagedata.vi=(double**) new double * [2];
        for (int i=0;i<2;i++)
        {
                averagedata.xi[i]=(double *) new double[nlines];
                averagedata.vi[i]=(double *) new double[nlines];
        }

        for (i=0;i<nlines;i++)
                for (j=0;j<2;j++)
                {
                        averagedata.xi[j][i]=data.xi[j][i];
                        averagedata.vi[j][i]=0;
                }
//      averagedata.xi=data.xi;
        first=false;
}

for (i=0;i<nlines;i++)
        for (j=0;j<2;j++)
                averagedata.vi[j][i]+=data.vi[j][i];

//      averagedata.vi=averagedata.vi+data.vi;

for (i=0;i<2;i++)
{
        avdata.xi[i][0]=Average(data.xi[i],nlines);
        avdata.vi[i][0]=Average(data.vi[i],nlines);
        fout << avdata.vi[i][0] << "\t";
}



thetax=GranTemp(data.vi[0],nlines,avdata.vi[0][0]);
thetay=GranTemp(data.vi[1],nlines,avdata.vi[1][0]);

fout << thetax << "\t" << thetay << "\t" << thetax+thetay << "\n";
```

```
                delete [] data.xi;
                delete [] data.vi;
                delete [] avdata.xi;
                delete [] avdata.vi;

                cout << "\t" << temp << "\n" << flush;
        }

        fout.close();

//      for (i=0;i<nlines;i++)
//              for (j=0;j<2;j++)
//                      averagedata.vi[j][i]/=((double)(max-min));

//      averagedata.vi=averagedata.vi/((double)(max-min));

        fout.open(foutav,ios::out);

        for (i=0;i<nlines;i++)
        {
                for (j=0;j<2;j++)
                        fout << averagedata.xi[j][i] << "\t";
                for (j=0;j<2;j++)
                        fout << (averagedata.vi[j][i]/((double)(max-min))) << "\t";

                fout << "\n";
        }

        fout.close();

        delete [] averagedata.xi;
        delete [] averagedata.vi;

        cout << "\nOutput written in " << foutname << "\n" << flush;

        return 0;
}


//function counts number of lines of data in a file
int CountLinesofData(char * filename)
{
        char c;
        int size=0;
        bool datainline = false;
        ifstream fin(filename,ios::in|ios::nocreate);
        if (!fin.is_open())
        {
                cout << "Error opening file\n" << flush;
                return -1;
```

```
        }
//count no. lines in file:
        while(fin.get(c))
        {
                switch(c)
                {
                case '\n':
                        if (datainline)
                                size++;
                        datainline = false;
                        break;
                default:
                        datainline = true;
                        break;
                }
        }
//if data in last line, but EOF instead of '\n' then increment size
        if (datainline)
                size++;

        fin.close();

//      cout << "Size of population: " << size << "\n" << flush;

        return size;
}

int MaxFiles(char *filename, int min)
{
        char temp[100];
        int max;
        bool exist=true;
        ifstream fin;

        max=min;

        do
        {
                if(max<10)
                        sprintf(temp,"%s000%i.txt",filename,max);
                else if (max<100)
                        sprintf(temp,"%s00%i.txt",filename,max);
                else if (max<1000)
                        sprintf(temp,"%s0%i.txt",filename,max);
                else
                        sprintf(temp,"%s%i.txt",filename,max);
//              cout << temp << "\n";

                fin.open(temp,ios::in| ios::nocreate);
                if(fin.is_open())
                {
```

```
                        max++;
                        fin.close();
                }
                else
                {
//                      max--;
                        exist=false;
                }
        } while (exist);

        if (max!=min)
                max--;

        return max;
}


void ReadData(pivdata & d, char * f, int n)
{
        ifstream fin;
//      double xcoord=106,ycoord=145;
        char temp[50];

        sprintf(temp,"vel_%i_%i.dat",(int)xcoord, (int)ycoord);

        fin.open(f,ios::in|ios::nocreate);

        ofstream fvout(temp,ios::out|ios::app);

        for (int i=0;i<n;i++)
        {
                fin >> d.xi[0][i] >> d.xi[1][i] >> d.vi[0][i] >> d.vi[1][i];
                if ((d.xi[0][i]==xcoord)&&(d.xi[1][i]==ycoord))
                        fvout << d.vi[0][i] << "\t" << d.vi[1][i] << "\n";
        }

        fin.close();
        fvout.close();
}

double Average(double * d, int n)
{
        double sum=0;

        for (int i=0;i<n;i++)
        {
                sum+=d[i];
        }

        return (double)sum/n;
}
```

```
double GranTemp(double * d, int n, double av)
{
	double sum=0;

	for (int i=0;i<n;i++)
	{
		sum+=pow((d[i]-av),2);
	}

	return (double)sum/n;
}
```

Appendix C:

'Mathematica' code for processing velocity array files to produce velocity graphs, frequency analysis and plots in rotating frame of reference.

Code originally written by Prof. M. J. Hounslow (PPG, University of Sheffield) and subsequently modified by the author.

209 rpm

209 rpm

Setup and read the data

```
<<Statistics`DescriptiveStatistics`
<<Graphics`ComplexMap`
<<Graphics`Graphics3D`
Mean[{1}]
```

1

```
SetDirectory["C:\D\Velocity Evaluation\Fourier_Analysis\Diff_rpm"]
```

C:\D\Velocity Evaluation\Fourier_Analysis\Diff_rpm

```
data=ReadList["209rpm.txt",Real,RecordLists→True];
Dimensions[data]
```

{3000,3}

```
{tlist,Vxlist,Vylist}=Transpose[data];
speedlist = Sqrt[Vxlist^2 + Vylist^2];
```

$$\frac{1}{2(tlist[[2]]-tlist[[1]])}$$

562.499

```
Mean[{1}]
```

1

Time Domain

Velocities

```
{ {"", "Average", "Standard Deviation"},
 {"Speed", Mean[speedlist], StandardDeviation[speedlist]},
 {"Vx", Mean[Vxlist], StandardDeviation[Vxlist]},
 {"Vy", Mean[Vylist], StandardDeviation[Vylist]}
```

} // TableForm

	Average	Standard Deviation
Speed	1.19017	0.0882537
V_x	1.171	0.0968999
V_y	0.12931	0.164178

Speed

ListPlot[Transpose[{tlist, speedlist}], ImageSize → {4177, 177}, AspectRatio → 1/5, PlotRange → {Automatic, Automatic}, PlotStyle → {AbsolutePointSize[2]}, TextStyle → {FontSize → 18}, Frame → True, FrameLabel → {"t (s)", "|V| (m s^{-1})"}]

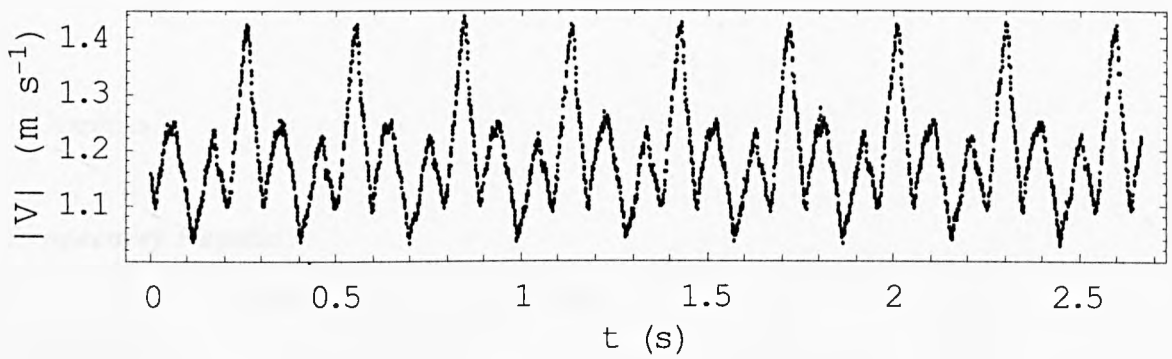

□Graphics□

V_x

ListPlot[Transpose[{tlist, Vxlist}], ImageSize → {4177, 177}, AspectRatio → 1/5, PlotRange → {Automatic, Automatic}, PlotStyle → {AbsolutePointSize[2]}, TextStyle → {FontSize → 18}, Frame → True, FrameLabel → {"t (s)", "V_x (m s^{-1})"}]

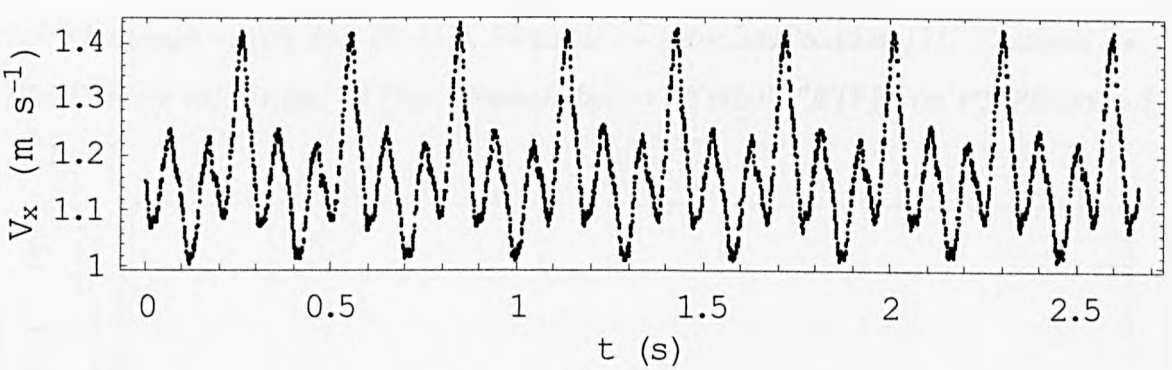

□Graphics□

V_y

ListPlot[Transpose[{tlist, Vylist}], ImageSize → {4177, 177}, AspectRatio → 1/5, PlotRange → {Automatic, Automatic}, PlotStyle → {AbsolutePointSize[2]}, TextStyle → {FontSize → 18}, Frame → True, FrameLabel → {"t (s)", /V_y (m s^-1)"}]

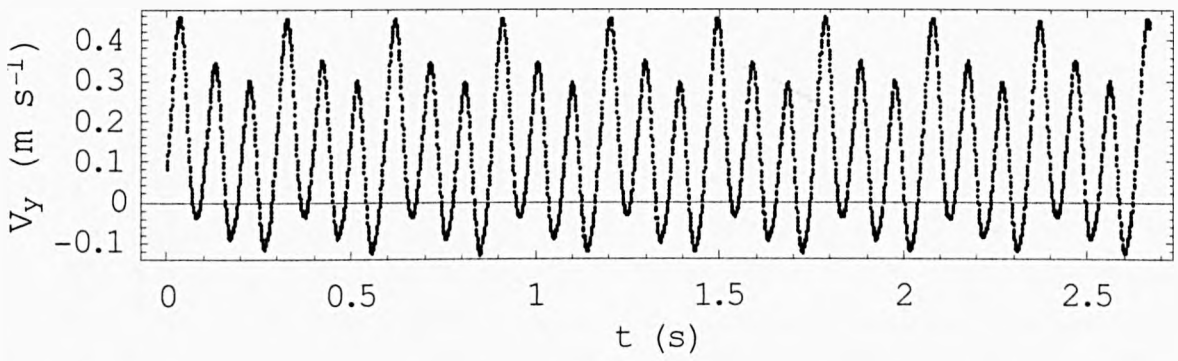

□Graphics□

Frequencey Domain

flist=Table[t,{t,0,Length[tlist]-1}]/Last[tlist];

Length[flist]

3000

ftspeed=Fourier[speedlist];

ftvx=Fourier[Vxlist];

ftvy=Fourier[Vylist];

Power Spectra

Speed

ListPlot[Transpose[{flist, Abs[ftspeed]^2}], ImageSize → {4177, 177}, AspectRatio → 1/5, PlotRange → {{0, 35}, {0, 15}}, PlotStyle → {AbsolutePointSize[3]}, TextStyle → {FontSize → 18}, Frame → True, FrameLabel → {"f (Hz)", "/F[V]/^2 (m^2)"}, PlotJoined → True]

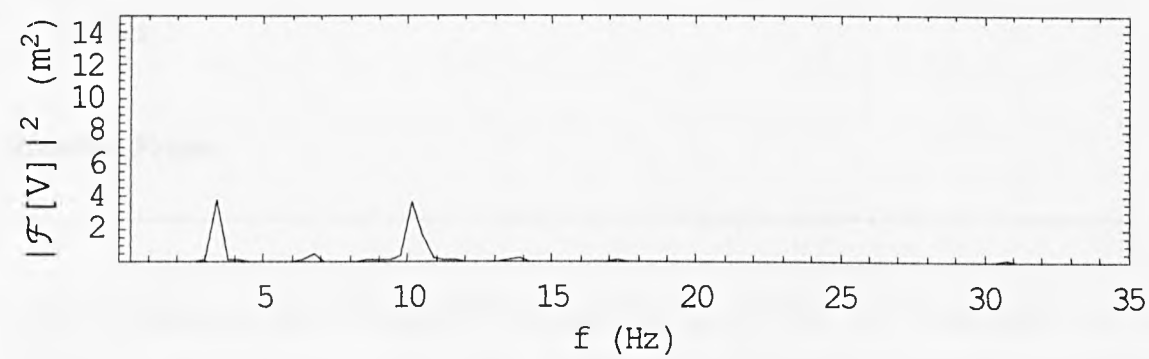

□Graphics□

V_x

ListPlot[Transpose[{flist, Abs[ftvx]^2}], ImageSize → {4177, 177}, AspectRatio → 1/5, PlotRange → {{0, 35}, {0, 15}}, PlotStyle → {AbsolutePointSize[3]}, TextStyle → {FontSize → 18}, Frame → True, FrameLabel → {"f (Hz)", "|F[V_x]|^2 (m^2)"}, PlotJoined → True]

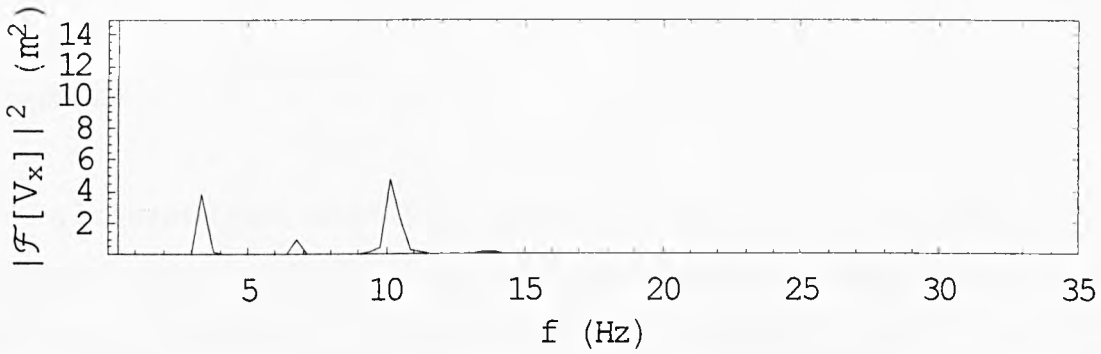

□Graphics□

V_y

ListPlot[Transpose[{flist, Abs[ftvy]^2}], ImageSize → {4177, 177}, AspectRatio → 1/5, PlotRange → {{0, 35}, {0,20}}, PlotStyle → {AbsolutePointSize[3]}, TextStyle → {FontSize → 18}, Frame → True, FrameLabel → {"f (Hz)", "|F[V_y]|^2 (m^2)"}, PlotJoined → True]

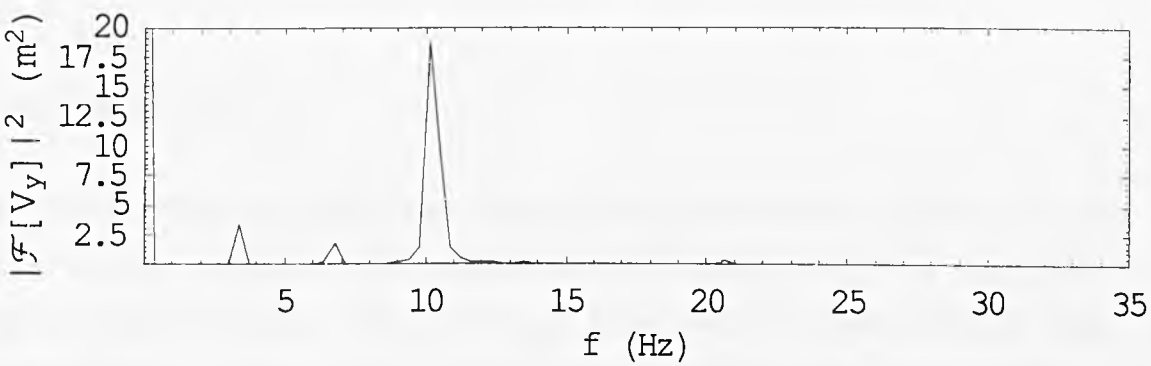

□Graphics□

Rotating Frame

ListPlot[Transpose[{flist, Abs[ftvx]^2}], ImageSize → {4177, 177}, AspectRatio →1/5, PlotRange →{{3.37, 3.39}, {3.7, 3.9}}, PlotStyle → {AbsolutePointSize[3]}, TextStyle

→ {FontSize → 18}, Frame → True, FrameLabel → {"f (Hz)", "|F[V_x]| ^{2} (m^2)"}, PlotJoined → True]

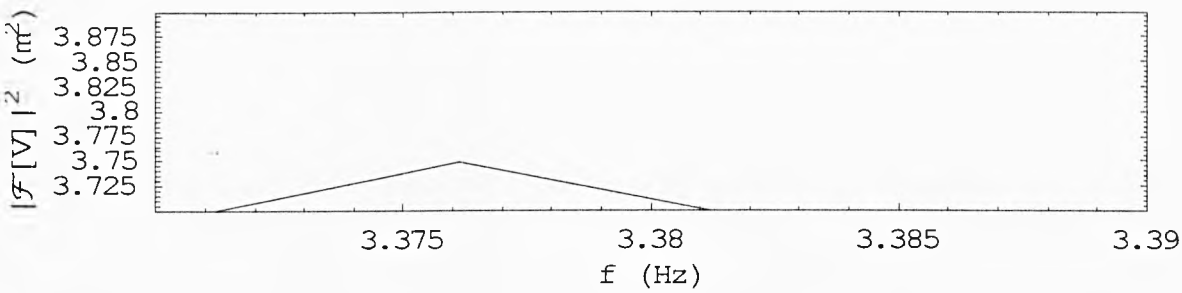

□Graphics□

ListPlot[Transpose[{flist, Abs[ftvx]^2}], ImageSize → {4177, 177}, AspectRatio →1/5, PlotRange →{{10.1, 10.2}, {3, 4}}, PlotStyle → {AbsolutePointSize[3]}, TextStyle → {FontSize → 18}, Frame → True, FrameLabel → {"f (Hz)", "|F[V] | ^{2} (m^2)"}, PlotJoined → True]

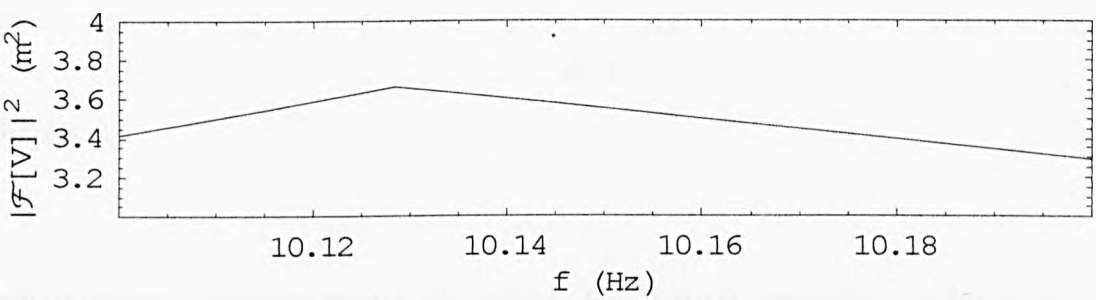

□Graphics□

flist[[Range[1,94]]]

{0,0.375125,0.75025,1.12538,1.5005,1.87563,2.25075,2.62588,3.001,3.37613,3.75125,4.12638,4.5015,4.87663,5.25175,5.62688,6.002,6.37713,6.75225,7.12738,7.5025,7.87763,8.25275,8.62788,9.003,9.37813,9.75325,10.1284,10.5035,10.8786,11.2538,11.6289,12.004,12.3791,12.7543,13.1294,13.5045,13.8796,14.2548,14.6299,15.005,15.3801,15.7553,16.1304,16.5055,16.8806,17.2558,17.6309,18.006,18.3811,18.7563,19.1314,19.5065,19.8816,20.2568,20.6319,21.007,21.3821,21.7573,22.1324,22.5075,22.8826,23.2578,23.6329,24.008,24.3831,24.7583,25.1334,25.5085,25.8836,26.2588,26.6339,27.009,27.3841,27.7593,28.1344,28.5095,28.8846,29.2598,29.6349,30.01,30.3851,30.7603,31.1354,31.5105,31.8856,32.2608,32.6359,33.011,33.3861,33.7613,34.1364,34.5115,34.8866}

*omega=2 * 10.128376116931998`/3*

21.2128

philist=omega tlist;

Speed

ListPlot[Transpose[{180/π Mod[1.015 philist, 2π], speedlist}], ImageSize → {4177, 177}, AspectRatio → 1/5, PlotRange → Automatic, PlotStyle → {AbsolutePointSize[2]}, TextStyle → {FontSize → 18}, Frame → True, FrameLabel → {"ϕ (°)", "|V| (m s^{-1})"}]

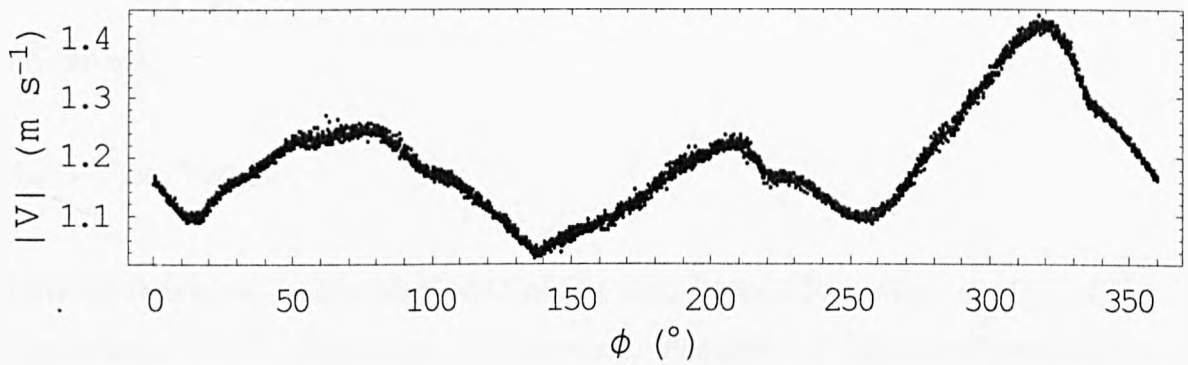

□Graphics□

V_x

ListPlot[Transpose[{180/π Mod[1.015 philist, 2π], Vxlist}], ImageSize → {4177, 177}, AspectRatio → 1/5, PlotRange → Automatic, PlotStyle → {AbsolutePointSize[2]}, TextStyle → {FontSize → 18}, Frame → True, FrameLabel → {"ϕ (°)", "V_x (m s^{-1})"}]

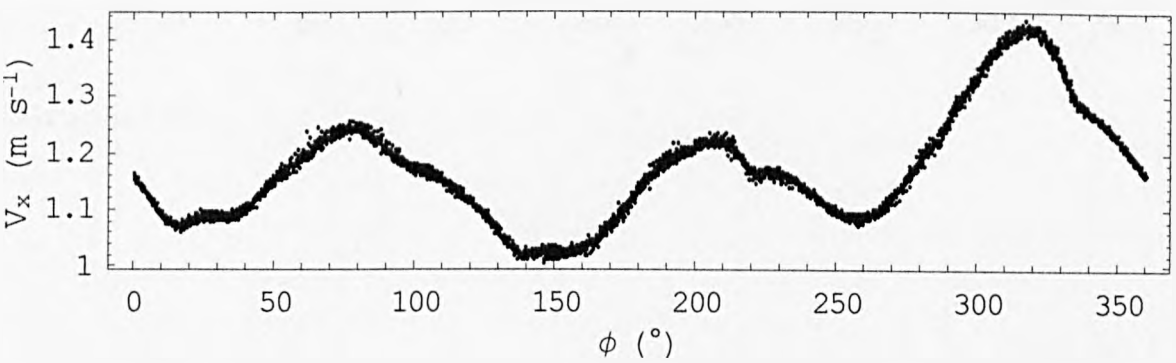

□Graphics□

V_y

ListPlot[Transpose[{180/π Mod[1.015 philist, 2π], Vylist}], ImageSize → {4177, 177}, AspectRatio → 1/5, PlotRange → Automatic, PlotStyle → {AbsolutePointSize[2]}, TextStyle → {FontSize → 18}, Frame → True, FrameLabel → {"ϕ (°)", "V_y (m s^{-1})"}]

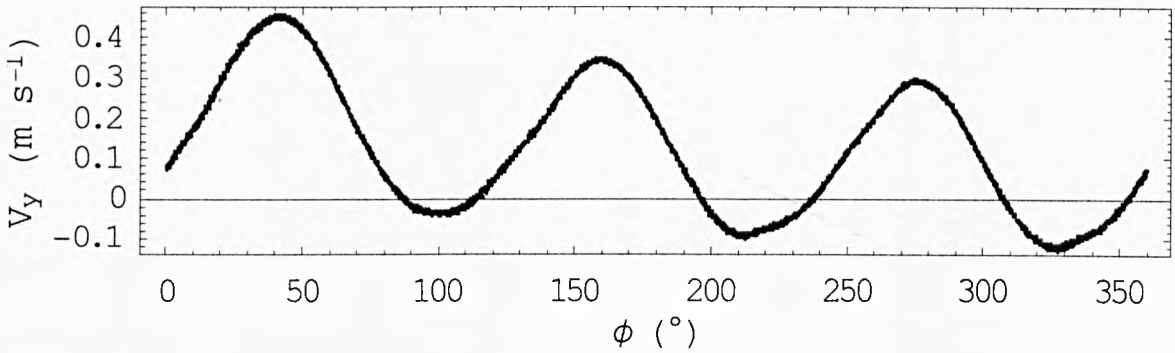

□Graphics□

Ratio=Vylist/Vxlist;

ListPlot[Transpose[{180/π Mod[1.015 philist, 2π], Ratio}], ImageSize → {4177, 177}, AspectRatio → 1/5, PlotRange → Automatic, PlotStyle → {AbsolutePointSize[2]}, TextStyle → {FontSize → 18}, Frame → True, FrameLabel → {"ϕ (°)", "V_y/ V_x "}]

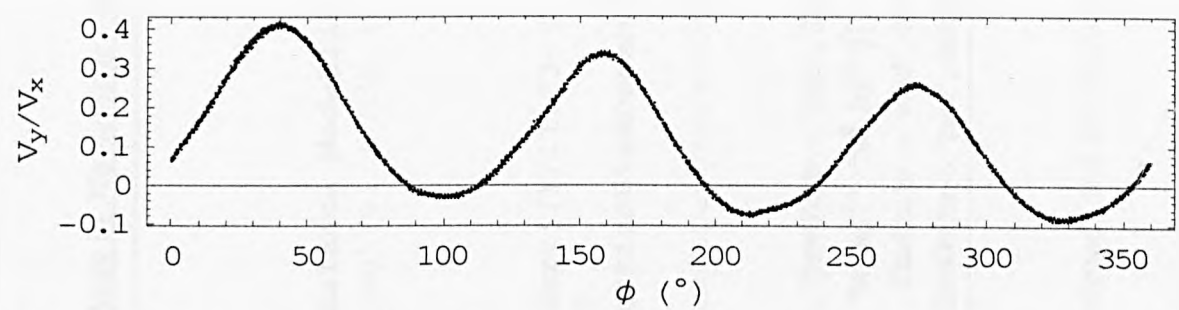

□Graphics□

Appendix D:

Aggregation rate extraction with 'DPB' package in *Mathematica* written by Prof. M.J. Hounslow (2002)

Start-up stuff

Read in the package

```
Off[General::"spell1"]
Off[General::"spell"]
SetDirectory["C:\D\Population Balance Modelling\Vel + GSD_july05"]
C:\D\Population Balance Modelling\Vel + GSD_july05
<<DPB`
$DPBVersion
6.0.4
```

Define a model

```
EKEKernel[l1_,l2_]:=(l1+l2)^2 Sqrt[(1/l1)^3+(1/l2)^3]
ShearKernel[l1_,l2_]:=(l1+l2)^3 ;
model={Aggregation->True,AggregationSizeDependence→EKEKernel,AggregationRateConstant-
>Function[{t}, beta0]}
{Aggregation→True,AggregationSizeDependence→EKEKernel,AggregationRateConstant→Function[{t},beta0]
}
```

Set the plot options

```
momentplotoptions = {TimeScaleFactor -> 1/60., TimeUnits -> "min", SizeScaleFactor → 10^3, SizeUnits -> "mm",
    MomentUnits → {"kg^-1", "m kg^-1", "m^2 kg^-1", "m^3 kg^-1", "m^4 kg^-1"}};
numberplotoptions = {TimeScaleFactor -> 1/60., TimeUnits -> "min", SizeScaleFactor → 10^3, SizeUnits -> "mm", AmountUnits -> "kg", PlotRange → All};
massplotoptions = {TimeScaleFactor -> 1/60., TimeUnits -> "min", SizeScaleFactor → 10^3, SizeUnits -> "mm", AmountUnits -> "-", PlotRange → All};
```

Read the data

```
file="Vel+GSD_July05.csv";
```

Read in the data, scaling time from minutes to seconds and size from microns to metres

```
rawdata=ReadSSFile[file,RecordSeparators->"\n",SizeScaleFactor->10^-3,TimeScaleFactor->60.]
```

```
{{60.,240.,420.,600.,900.,1200.},{0.00003,0.000032,0.000036,0.00004,0.000045,0.000051,0.000057,0.0
00064,0.000072,0.000081,0.00009,0.000102,0.000114,0.000128,0.000144,0.000161,0.000181,0.000203,0.0
00228,0.000256,0.000287,0.000322,0.000362,0.000406,0.000456,0.000512,0.000575,0.000645,0.000724,0.
000813,0.000912,0.001024,0.001149,0.00129,0.001448,0.001625,0.001825,0.002048,0.002299,0.00258,0.0
02896,0.003251,0.003649,0.004096,0.004598,0.005161,0.005793,0.006502,0.007298,0.008192,0.009195,0.
010321},{{0.0002,0.0005,0.0006,0.0007,0.0021,0.0043,0.0075,0.0122,0.0203,0.0316,0.0465,0.0899,0.10
93,0.125,0.1196,0.1045,0.0869,0.07,0.0535,0.0388,0.0275,0.0189,0.012,0.0067,0.0042,0.0023,0.0014,0
.0008,0.0006,0.0004,0.0003,0.0002,0.0001,0.0001,0.0001,0.0001,0.,0.,0.,0.,0.,0.,0.,0.,0.,0.,0.,
0.,0.,0.},{0.0002,0.0005,0.0007,0.001,0.0025,0.0056,0.0085,0.0125,0.0169,0.0242,0.0356,0.0722,0.09
29,0.1163,0.1147,0.1039,0.0877,0.0744,0.0607,0.0473,0.038,0.0272,0.0188,0.0134,0.009,0.0057,0.0032
,0.0022,0.0012,0.0009,0.0006,0.0004,0.0003,0.0002,0.0002,0.0001,0.0001,0.0001,0.,0.,0.,0.,0.,0.,0.
,0.,0.,0.,0.,0.,0.},{0.0002,0.0005,0.0005,0.0006,0.002,0.0045,0.0072,0.0092,0.0118,0.0148,0.0198,0
.0349,0.0537,0.0763,0.0997,0.1062,0.1035,0.1019,0.0871,0.0726,0.057,0.0428,0.0323,0.0226,0.0141,0.
0094,0.0057,0.0034,0.0021,0.0011,0.0006,0.0005,0.0004,0.0003,0.0002,0.0001,0.0001,0.0001,0.0001,0.
,0.,0.,0.,0.,0.,0.,0.,0.,0.,0.,0.},{0.0002,0.0004,0.0005,0.0013,0.0034,0.0072,0.0115,0.0138,0.0165
,0.0176,0.0224,0.0374,0.0467,0.0663,0.0862,0.0978,0.1027,0.0976,0.0891,0.0769,0.0624,0.047,0.0338,
0.0227,0.0154,0.0098,0.0053,0.003,0.0017,0.0011,0.0006,0.0004,0.0003,0.0002,0.0002,0.0001,0.0001,0
.0001,0.,0.,0.,0.,0.,0.,0.,0.,0.,0.,0.,0.,0.},{0.0002,0.0004,0.0005,0.0008,0.003,0.0061,0.0091,0.0
117,0.0126,0.0141,0.0197,0.0339,0.0426,0.0529,0.0655,0.0833,0.0992,0.104,0.1021,0.0912,0.0748,0.05
94,0.0419,0.0283,0.0185,0.0099,0.0063,0.0033,0.0017,0.001,0.0006,0.0004,0.0002,0.0002,0.0001,0.000
1,0.0001,0.0001,0.,0.,0.,0.,0.,0.,0.,0.,0.,0.,0.,0.,0.},{0.0002,0.0005,0.0006,0.0016,0.0051,0.0102
,0.0151,0.0164,0.017,0.0161,0.0199,0.0331,0.0392,0.0487,0.0546,0.0596,0.0742,0.0882,0.0906,0.0931,
0.0814,0.0697,0.055,0.0394,0.0284,0.0177,0.01,0.0062,0.0032,0.0017,0.0012,0.0006,0.0004,0.0003,0.0
002,0.0002,0.0001,0.0001,0.0001,0.,0.,0.,0.,0.,0.,0.,0.,0.,0.,0.,0.}}}
```

Convert the raw data to a standard dataset format. Normalise to make the third moment refer to a solids volume fraction of 0.5

```
data=DeltaNtoN[rawdata,NormaliseMoment→{3,0.5 6/π}];
data=AddEmptyChannels[data,6];
```

Plot the data

MomentPlot[data,momentplotoptions]

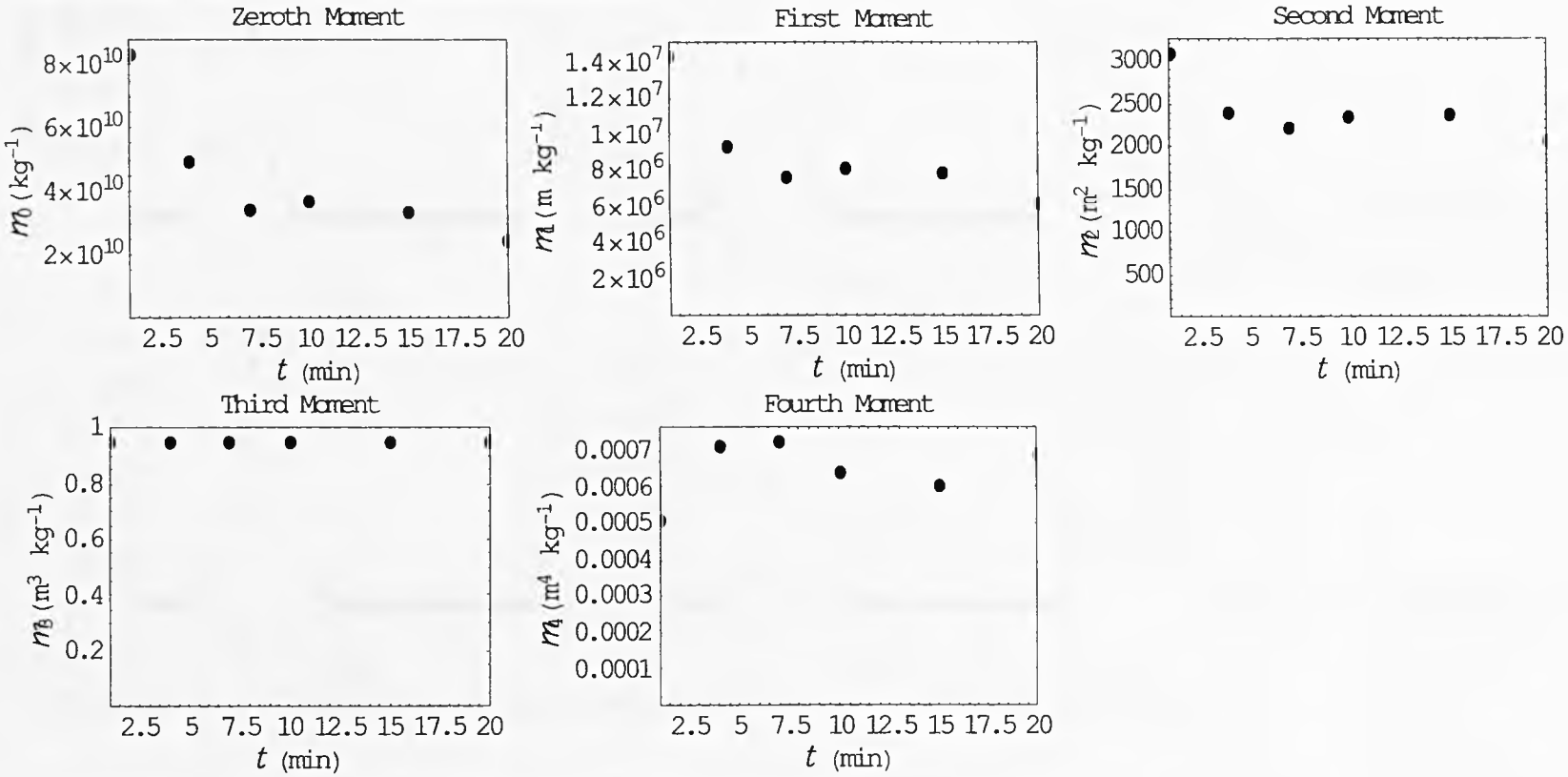


```
{-Graphics-,-Graphics-,-Graphics-,-Graphics-,-Graphics-}
```

NumberPlot[data,numberplotoptions]

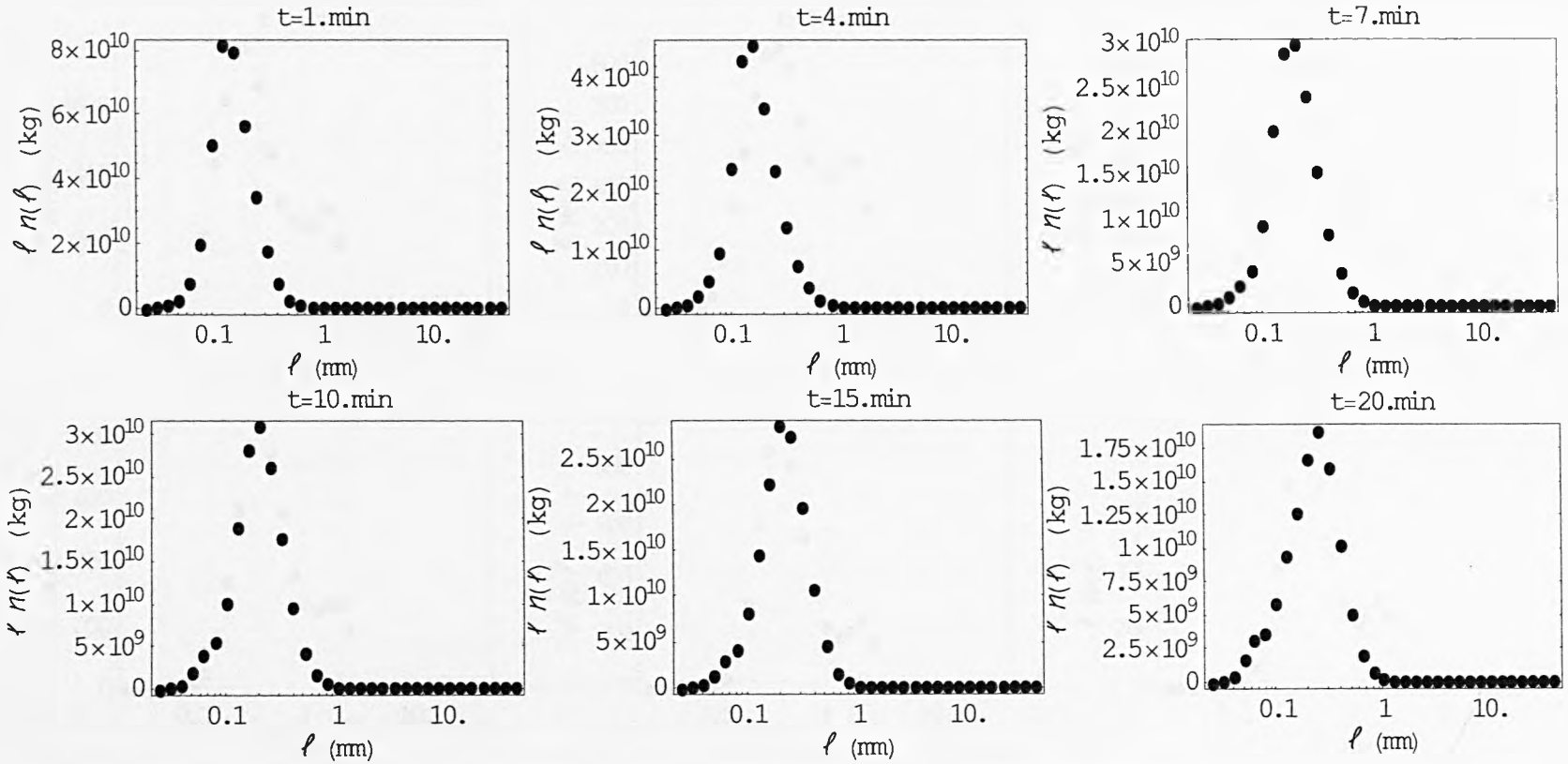

{-Graphics-,-Graphics-,-Graphics-,-Graphics-,-Graphics-,-Graphics-}

MassPlot[data,massplotoptions]

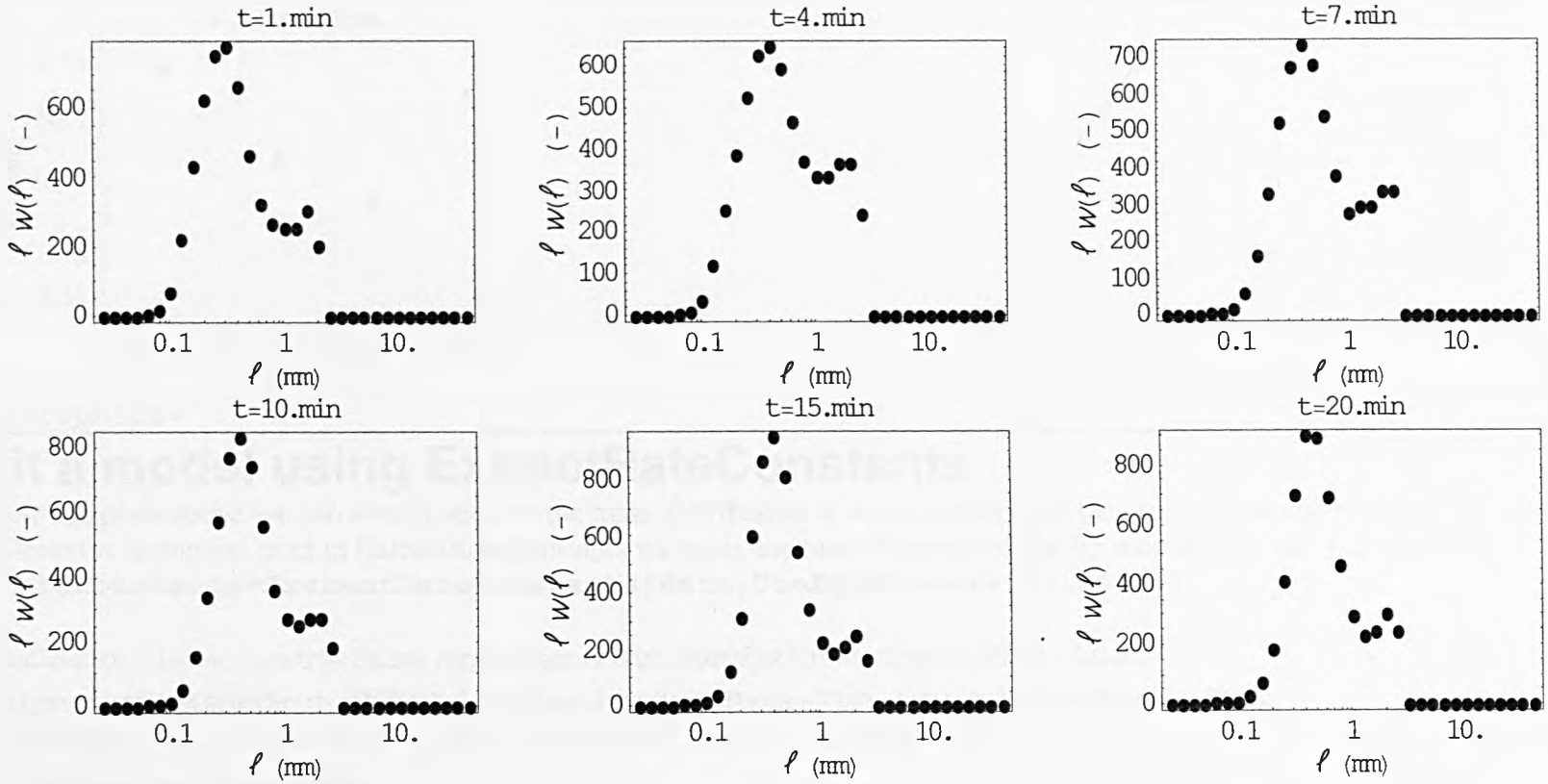


```
{-Graphics-,-Graphics-,-Graphics-,-Graphics-,-Graphics-,-Graphics-}
```

```
MeanSizePlot[data,DefiningMoments→{3,4},momentplotoptions]
```

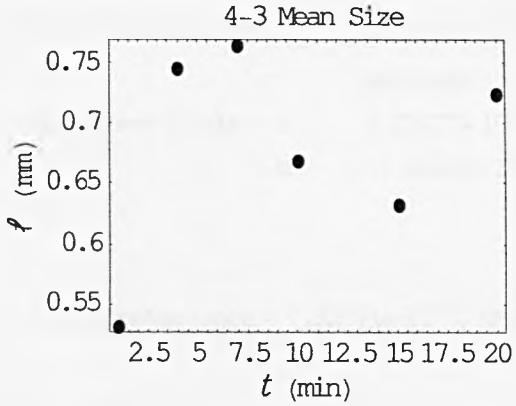

-Graphics-

Fit a model using ExtractRateConstants

From the plots above we can clearly see that the mass distribution is better conditioned than the number distribution. So we will fit to that. For the differential technique used in ExtractRateConstants we study the rate of change of the 4th moment, i.e. the 4-3 mean size.

```
rateconstants=ExtractRateConstants[data,UseEquations→{4},model]
```

{Nucleation→ False, Growth→ False, Aggregation→ True, AggregationRateConstantKnown→ False,
AggregationSizeDependence→ EKEKernel, AggregationDrivingForce→ Time, AggregationInnerKernel→ None,
Beta0Data→ {{60., 4.91177×10^{-12}}, {240., 2.58616×10^{-12}}, {420., -9.79846×10^{-13}}, {600., -1.61752×10^{-12}}, {900., 3.93869×10^{-13}}, {1200., 2.78233×10^{-12}}},
Breakage→ False, Sink→ False}

```
model1=FitRateConstants[rateconstants]
```

Aggregation Fit

$$\{\text{BestFit} \to 2.22007\times10^{-12} - 1.53323\times10^{-15}\,t,\ \text{BestFitParameters} \to \{a \to 2.22007\times10^{-12},\ b \to -1.53323\times10^{-15}\},$$

ParameterCITable →

	Estimate	Asymptotic SE	CI
a	2.22007×10^{-12}	1.96744×10^{-12}	$\{-3.24243\times10^{-12},\ 7.68257\times10^{-12}\}$,
b	-1.53323×10^{-15}	2.85587×10^{-15}	$\{-9.46239\times10^{-15},\ 6.39594\times10^{-15}\}$

EstimatedVariance → 7.32571×10^{-24}, ANOVATable →

	DF	SumOfSq	MeanSq
Model	2	1.29838×10^{-23}	6.49192×10^{-24}
Error	4	2.93029×10^{-23}	7.32571×10^{-24},
Uncorrected Total	6	4.22867×10^{-23}	
Corrected Total	5	3.14143×10^{-23}	

AsymptoticCorrelationMatrix → $\begin{pmatrix} 1. & -0.827391 \\ -0.827391 & 1. \end{pmatrix}$, FitCurvatureTable →

	Curvature
Max Intrinsic	0
Max Parameter-Effects	0
95. % Confidence Region	0.379478

}

{Nucleation → False, Growth → False, Aggregation → True, AggregationRateConstantKnown → True, AggregationSizeDependence → EKEKernel, AggregationDrivingForce → Ti
AggregationInnerKernel → None, AggregationRateConstant → Function[t, $2.22007\times10^{-12} - 1.53323\times10^{-15}$ t], Breakage → False, Sink → False}

```
RateConstantPlot[model1,rateconstants,PlotRange→All]
```

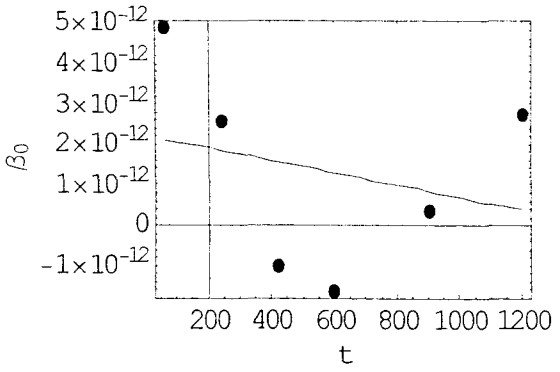


```
{-Graphics-}
```

Since the slope of this plot is not statistically significant, fit a model of zero slope

```
model2=FitRateConstants[rateconstants,AggregationRateConstantModel→a,AggregationRateConstantModelP
arameters→{a}]
 Aggregation Fit
```

{BestFit → 1.34613×10^{-12}, BestFitParameters → {a → 1.34613×10^{-12}}, ParameterCITable →

	Estimate	Asymptotic SE	CI
a	1.34613×10^{-12}	1.0233×10^{-12}	{-1.28435×10^{-12}, 3.97661×10^{-12}

	DF	SumOfSq	MeanSq
Model	1	1.08724×10^{-23}	1.08724×10^{-23}
Error	5	3.14143×10^{-23}	6.28287×10^{-24},
Uncorrected Total	6	4.22867×10^{-23}	
Corrected Total	5	3.14143×10^{-23}	

EstimatedVariance → 6.28287×10^{-24}, ANOVATable →

AsymptoticCorrelationMatrix → {{1.}}, FitCurvatureTable →

	Curvature
Max Intrinsic	0
Max Parameter-Effects	0
95. % Confidence Region	0.389017

{Nucleation → False, Growth → False, Aggregation → True, AggregationRateConstantKnown → True, AggregationSizeDependence → EKEKernel, AggregationDrivingForce → Time, AggregationInnerKernel → None, AggregationRateConstant → Function[t, 1.34613×10^{-12}], Breakage → False, Sink → False}

RateConstantPlot[model2,rateconstants,PlotRange→{Automatic,Automatic}]

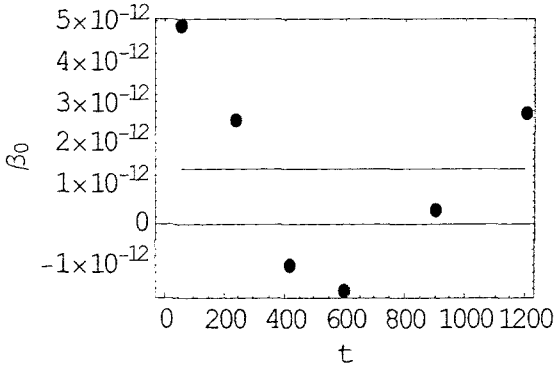

{-Graphics-}

```
RateConstants[model2,rateconstants]
```

RateConstants[{Nucleation→ False, Growth→ False, Aggregation→ True, AggregationRateConstantKnown→ True, AggregationSizeDependence→ EKEKernel, AggregationDrivingForce→ Time, AggregationInnerKernel→ None, AggregationRateConstant→ Function[t, 1.34613×10^{-12}], Breakage→ False, Sink→ False}, {Nucleation→ False, Growth→ False, Aggregation→ True, AggregationRateConstantKnown→ False, AggregationSizeDependence→ EKEKernel, AggregationDrivingForce→ Time, AggregationInnerKernel→ None, Beta0Data→ {{60., 4.91177×10^{-12}}, {240., 2.58616×10^{-12}}, {420., -9.79846×10^{-13}}, {600., -1.61752×10^{-12}}, {900., 3.93869×10^{-13}}, {1200., 2.78233×10^{-12}}}, Breakage→ False, Sink→ False}]

We can use this model to simulate the behaviour of the process

Simulate requires initial conditions

```
ic=Simdata[data,1]
```

{{60., 240., 420., 600., 900., 1200.}, {0.0000253977, 0.0000319992, 0.0000403164, 0.0000507955, 0.0000639983, 0.0000806328, 0.000101591, 0.000127997, 0.000161266, 0.000203182, 0.000255993, 0.000322531, 0.000406364, 0.000511986, 0.000645063, 0.000812728, 0.00102397, 0.00129013, 0.00162546, 0.00204795, 0.00258025, 0.00325091, 0.00409589, 0.0051605, 0.00650182, 0.00819178, 0.010321, 0.0130036, 0.0163836, 0.020642, 0.0260073, 0.0327671}, {1.67307×10^{7}, 9.48801×10^{7}, 2.22742×10^{8}, 9.96139×10^{8}, 2.63384×10^{9}, 6.44338×10^{9}, 1.68479×10^{10}, 2.06074×10^{10}, 1.59345×10^{10}, 1.0284×10^{10}, 5.57665×10^{9}, 2.56467×10^{9}, 9.064×10^{8}, 3.09787×10^{8}, 1.16972×10^{8}, 5.86993×10^{7}, 2.51188×10^{7}, 1.67546×10^{7}, 8.3457×10^{6}, 0, 0, 0, 0, 0, 0, 0, 0, 0, 0, 0, 0, 0}}

Simulate using model 2

```
sim2=Simulate[ic,model2];
```

Plot the results showing the data as points, the second model as a blue line

```
MassPlot[{sim2,data},massplotoptions,DatasetOptions→{{SmoothPlot→True,PlotStyle→RGBColor[0,0,1]},
{SmoothPlot→False}}]
```

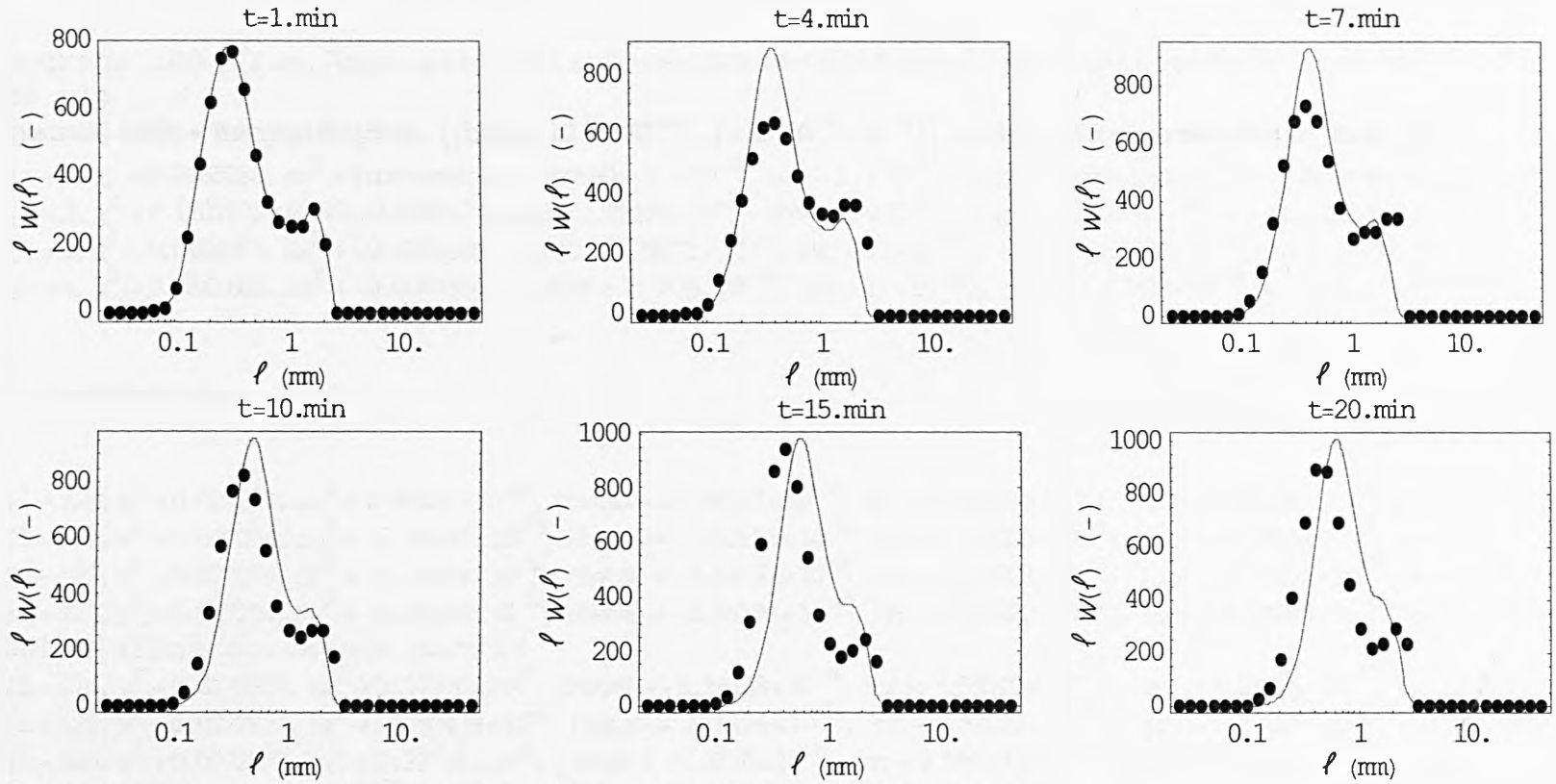


```
{-Graphics-,-Graphics-,-Graphics-,-Graphics-,-Graphics-,-Graphics-}
```

Integral Fit

As an alternative to the above approach, once we have decided that the rate constant does not depend on time, we can fit a value using least-squares minimization

```
model3={Aggregation->True,AggregationSizeDependence→EKEKernel,AggregationRateConstant-
>Function[{t},int +(beta0 t)]}

{Aggregation→True,AggregationSizeDependence→EKEKernel,AggregationRateConstant→Function[{t},int+be
ta0 t]}
{params, sim3} = IntegralFit[data, {{beta0, 10^-15, 10^-14}, {int, 10^-12, 10^-11}}, model3, SSECompareWeights -> {Size, 3}];
{i→ 1, χ^2→ 0.0985188, Δχ^2→ Indeterminate, {beta0→ 1.×10^-15, int→ 1.×10^-12}, |Δp|→ Indeterminate, e→ {Indeterminate, Indeterminate}}
{i→ 2, χ^2→ 0.110727, Δχ^2→ 0.0122085, {beta0→ 1.28125×10^-15, int→ 1.×10^-12}, |Δp|→ 2.8125×10^-16, e→ {1., 0.}}
{i→ 3, χ^2→ 0.0908907, Δχ^2→ -0.0198366, {beta0→ 8.26178×10^-16, int→ 1.×10^-12}, |Δp|→ 4.55072×10^-16, e→ {-1., 0.}}
{i→ 4, χ^2→ 0.0861603, Δχ^2→ -0.00473046, {beta0→ 7.1875×10^-16, int→ 1.×10^-12}, |Δp|→ 1.07428×10^-16, e→ {-1., 0.}}
.
.
...(Iterations, i)...
.
.
{i→ 120, χ^2→ 0.027284, Δχ^2→ 2.98025×10^-15, {beta0→ -5.56197×10^-16, int→ 7.52028×10^-13}, |Δp|→ 2.86626×10^-19, e→ {0.00177682, -0.999998}}
{i→ 121, χ^2→ 0.027284, Δχ^2→ -2.38698×10^-15, {beta0→ -5.56198×10^-16, int→ 7.52029×10^-13}, |Δp|→ 9.2754×10^-19, e→ {-0.00177682, 0.999998}}
{i→ 122, χ^2→ 0.027284, Δχ^2→ -9.15934×10^-16, {beta0→ -5.56197×10^-16, int→ 7.52028×10^-13}, |Δp|→ 5.73251×10^-19, e→ {0.00177682, -0.999998}}
{i→ 123, χ^2→ 0.027284, Δχ^2→ -4.44089×10^-16, {beta0→ -5.56198×10^-16, int→ 7.52029×10^-13}, |Δp|→ 3.54289×10^-19, e→ {-0.00177682, 0.999998}}
Calculating curvature matrix
{i→ 124, χ^2→ 0.0272934, Δχ^2→ 9.37976×10^-6, {beta0→ -5.56198×10^-16, int→ 7.59549×10^-13}, |Δp|→ 7.52015×10^-15, e→ {3.19741×10^-8, 1.}}
{i→ 125, χ^2→ 0.0272854, Δχ^2→ -7.92439×10^-6, {beta0→ -5.6176×10^-16, int→ 7.52029×10^-13}, |Δp|→ 7.52029×10^-15, e→ {-0.000739596, -1.}}
{i→ 126, χ^2→ 0.0272877, Δχ^2→ 2.29734×10^-6, {beta0→ -5.6176×10^-16, int→ 7.59549×10^-13}, |Δp|→ 7.52029×10^-15, e→ {0., 1.}}
CurvatureMatrix→ ( 3.27612×10^32   5.89568×10^29 )
                 ( 5.89568×10^29   1.15496×10^27 )
CovarianceMatrix→ ( 3.75111×10^-32   -1.9148×10^-29 )
                  ( -1.9148×10^-29   1.06402×10^-26 )
Minimum square error  0.027284
```

Parameter	Best Fit	Standard Error
beta0	-5.56198×10^{-16}	1.93678×10^{-16}
int	7.52029×10^{-13}	1.03151×10^{-13}

Simulating best fit results

```
MassPlot[{sim3,data},massplotoptions,DatasetOptions→{{SmoothPlot→True,PlotStyle→RGBColor[0,0,1]},
{SmoothPlot→False}}]
```

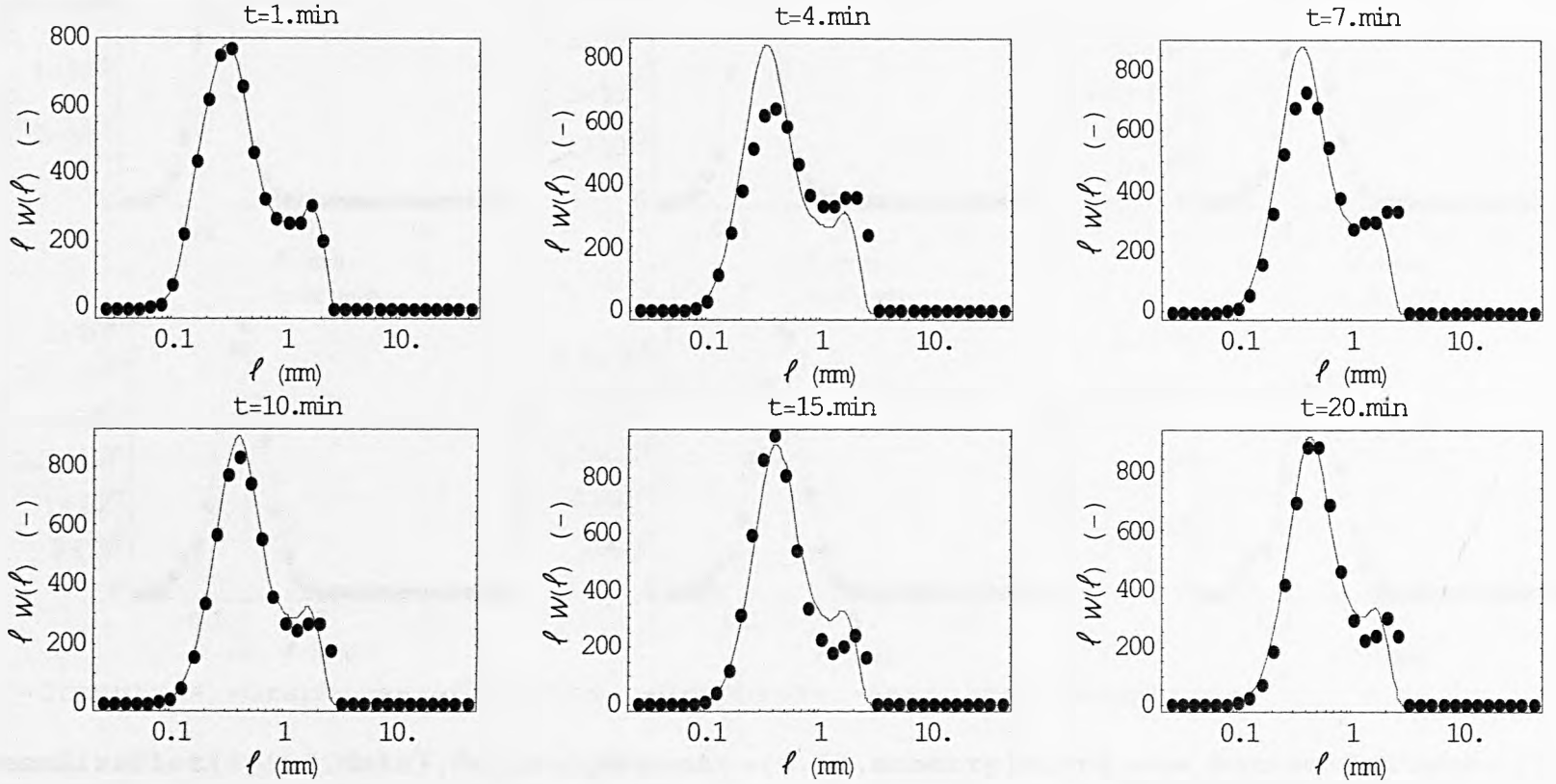

```
{-Graphics-,-Graphics-,-Graphics-,-Graphics-,-Graphics-,-Graphics-}
```

```
NumberPlot[{sim3,data},numberplotoptions,DatasetOptions→{{SmoothPlot→True,PlotStyle→RGBColor[0,0,
1]},{SmoothPlot→False}}]
```

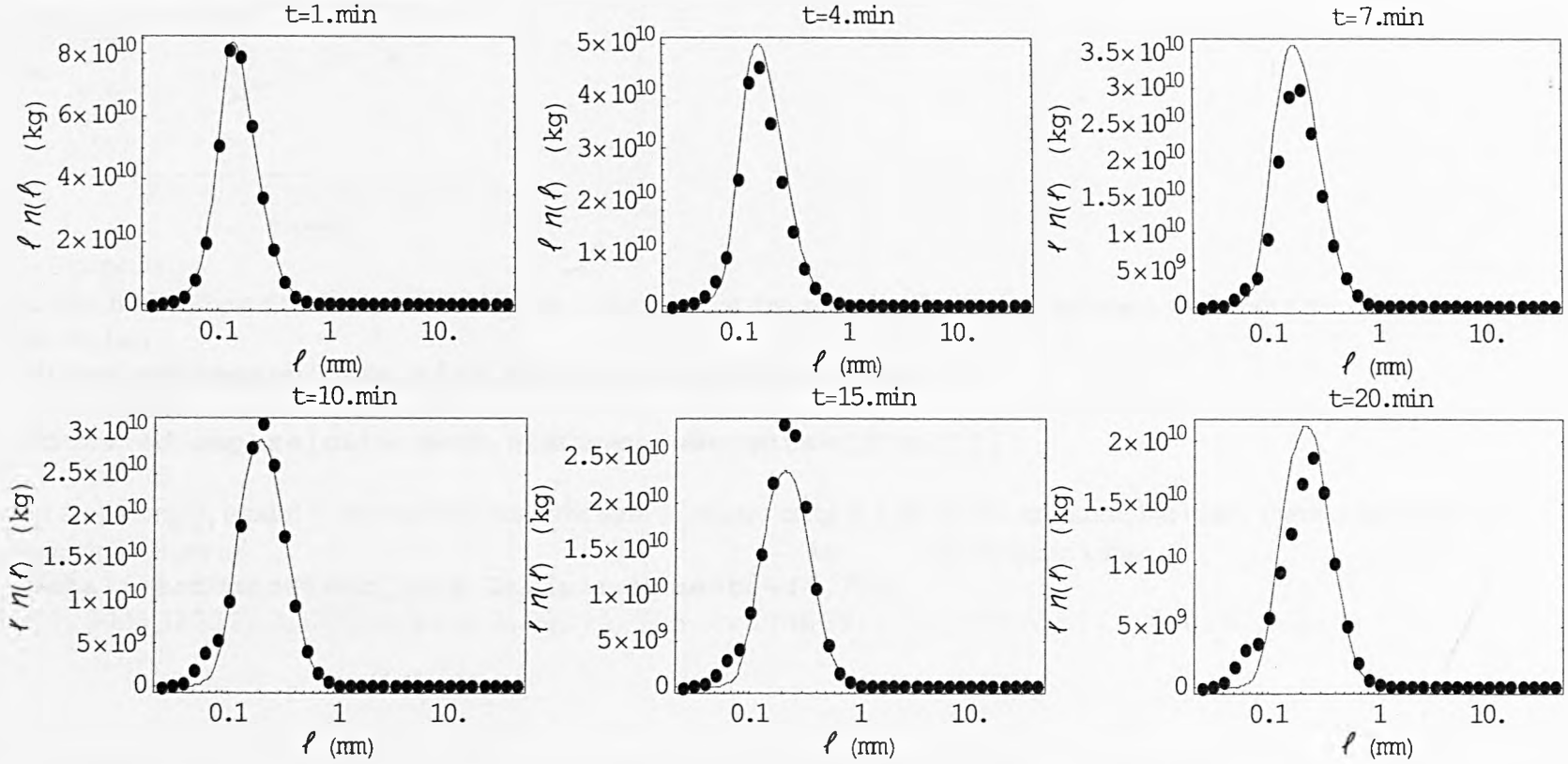


```
{-Graphics-,-Graphics-,-Graphics-,-Graphics-,-Graphics-,-Graphics-}
```

```
MeanSizePlot[{sim3,data},DefiningMoments→{4,3},momentplotoptions,DatasetOptions→{{SmoothPlot→True
,PlotStyle→RGBColor[0,0,1]},{SmoothPlot→False}},PlotRange→{All,Automatic}]
```

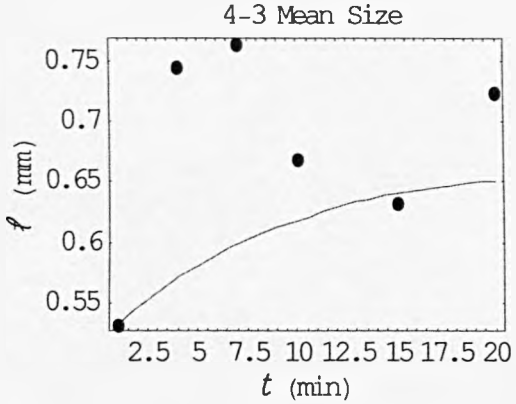

-Graphics-

So which is the best fit? We can calculate an statistic that describes the fraction of variation seen about the initial value that each of the models can explain

```
RSquaredCompare[data,sim2,SSECompareWeights→{Size,3}]
0.110344
RSquaredCompare[data,sim3,SSECompareWeights→{Size,3}]
0.716585
```

Not surprisingly, model 3, which minimises the sum of square error is best by this measure, but really there is no difference. Note also that the estimated values of kg i.e. the same value

```
GetalistofMeanSizes[data,DefiningMoments→{4,3}]
{0.000532322,0.000745412,0.000762706,0.000669177,0.000631544,0.000723285}
```